POLITECNICO
MILANO 1863

School of Industrial and Information Engineering

Master Degree in Engineering Physics

A widefield high-throughput hyperspectral microscope based on an ultrastable common-path interferometer

Supervisor:
Prof. Cristian Manzoni

Co-supervisor:
Prof. Gianluca Valentini

Candidate:
Benedetto Ardini
Matricola **920166**

Academic Year 2020-2021

"in the Primary Miracle (the Resurrection) and the lesser Christian miracles too though less, you have not only that sudden glimpse of the truth behind the apparent Anankê of our world, but a glimpse that is actually a ray of light through the very chinks of the universe about us"

-J.R.R. Tolkien

(letter n°89 to Christopher Tolkien)

Contents

List of Figures

List of Tables

Abstract

Hyperspectral microscopy is a very powerful tool because images with both spatial and spectral information of the samples are retrieved. For this reason it is an important technique for the materials recognition and characterization on the basis of their spectra and with a micrometer spatial resolution. Hyperspectral microscopy can be exploited for different spectral measurement implementations such as reflectivity, transmission, fluorescence and Raman. In general different hyperspectral imaging approaches both in the spectral and in the spatial domain can be adopted. In the spatial domain there's the basic distinction between raster scanning in which the image is acquired one point at a time and widefield in which the image is acquired at once. In the spectral domain there are two main different approaches: the Dispersive Spectroscopy in which the different wavelengths of the detected light are separated and resolved by means of prisms or gratings and the Fourier Transform Spectroscopy which relies on the Fourier transform operation to pass from an acquired interferogram of the detected light to a spectrum.
In 2019 a Fourier Transform Hyperspectral Microscope based a common-path ultrastable interferometer has been developed in Physics Department at Politecnico di Milano [1]. Relying on the advantages of Fourier Transform Spectroscopy, this microscope is used in the widefield approach and therefore all the spectra for the seval image pixels are retrieved at once. The ultrastability of the interferometer allows a simple use of this setup in a routinely laboratory activity.
Starting from the Hyperspectral Microscope introduced in [1], this master thesis deals with the consequent work undertaken on this setup in order to optimize and corroborate the reliability of the system both from an experimental-instrumental implementation and from a datum analysis point of view. In particular the effort has been focused on Raman widefield imaging because that is a very interesting and promising technique as the Raman spectrum peaks are specifically related to the particular chemical species and this allows a very selective characterization of the investigated sample. As Raman phenomenon is characterized by very low cross-section, an optimization of the measurement parameters in order to increase the Raman signal with respect to the background and an accurate choice of

the consequent hyperspectral datum analysis are fundamental in order to accomplish a significative result. In this sense much time has been spent in the laboratory activity to test the setup with different kind of samples and in the improvement of the related analysis software: the scope of this effort has been collecting appreciable results and complying with a proper analytical tool for the information extrapolation.
As it is demonstrated by this thesis work, the setup and its peculiar hyperspectral imaging technique have revealed a very promising system to perform widefield Raman imaging in fast measurements if compared with other works presented in literature and with an high spatial resolution. In addition, the measured Raman spectra are completely fluorescence-free even if the fluorescence intensity from the sample is not negligible: this is a novelty in the spectroscopy community as, in typical Raman setups, the measured Raman spectral peaks are superimposed to the broadband fluorescence background. These characteristics together with the ultrastability and the compactness make this instrument a good candidate for scientific research and industrial applications.

Chapter 1

Theory

1.1 Hyperspectral Imaging

Hyperspectral Imaging is a very powerful technique based on the acquisition of images in which each pixel contains spectral information.

In common imaging each pixel is represented by a single intensity value, in grayscale images, or by a red (R), green (G) and blue (B) value triad, in color images. In greyscale images the single value describes the overall irradiance, instead in color images the combination of the R, G and B values results in the color of the pixel: these representations give only information on the overall incoming light on that part of the electromagnetic spectrum perceived by the human eyes.

An hyperspectral image contains on each pixel an entire vector describing the spectral content as it is acquired: this means that for each pixel such an image contains the intensity associated to each spectral frequency and not only the three intensity values related to the RGB triad or, even worse, the single overall irradiance value as in greyscale images. For this reason an hyperspectral image is called "spectral hypercube" because the intensity values contained on it are organized in a three-dimensional matrix as it is shown in Figure 1.1.

Therefore considering a spectral hypercube means to deal with both spectral and spatial information at the same time: this is very important for applications in which it is requested the investigation of both morphological and chemical composition of the object to study. For these reasons hyperspectral imaging is commonly applied to environmental sensing [2], military target designation [3] and medical imaging [4] but also it has other important applications to several fields such as agriculture [5], astronomy [6], archeology [7] and art conservation [8].

From a spectral hypercube it is possible to obtain a wealth of information including an RGB image: each R, G and B value are calculated integrating the product between the spectrum and functional windows related to R, G

and B over the frequency/wavelength axis as it is shown in Figure 1.2. The real R, G and B windows are defined according to the human perception of colors. As in hyperspectral imaging we have extended spectral information, it is possible to assign the R, G and B windows to different ranges in the spectrum and to generate a false RGB image taking the integral of the product between the spectrum with the redefined RGB windows.

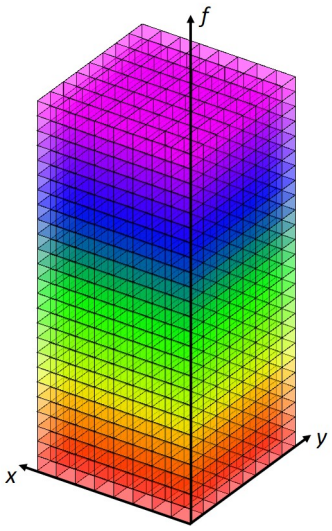

Figure 1.1: Representation of the spectral hypercube space as three-dimensional matrix: the x and y dimensions identify the pixels in the image plane, the f dimension indentifies the spectral frequencies. To enhance the fact that the spectral hypercube can be seen as a collection of images each one related to a particular frequency, each "slice" has been colored with a different hue.

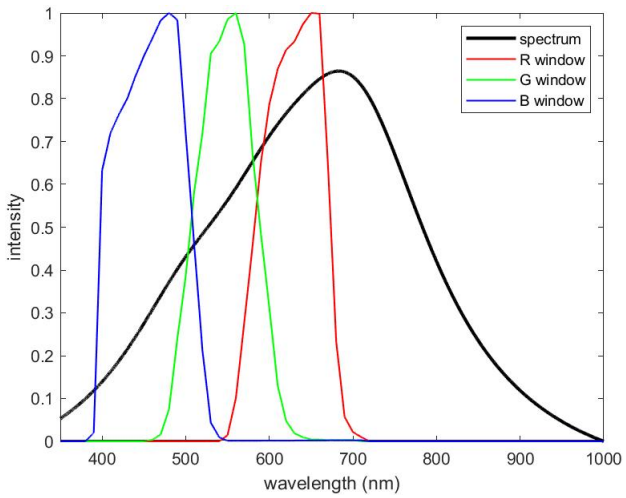

Figure 1.2: Example of a certain spectrum as a function of the wavelength and the three R, G and B windows located in the real wavelength range as perceived by the human eye.

1.2 Fourier Transform Spectroscopy

The Fourier Transform Spectroscopy is a technique based on the Wiener-Kintchine theorem.
This theorem was proved by Norbert Wiener in 1930 for the case of a deterministic function [9]. In the particular case of a continous function $E(t)$ the theorem states that the autocorrelation $\gamma(\tau)$ of $E(t)$ is bound to the power spectral density $S(f)$ of $E(t)$ according to this equality:

$$\gamma(\tau) = \int_{-\infty}^{+\infty} S(f) e^{i2\pi\tau f}\, df \tag{1.1}$$

where the autocorrelation is defined as

$$\gamma(\tau) \doteq \langle E(t)^* E(t-\tau)\rangle = \int_{-\infty}^{+\infty} E(t)^* E(t-\tau)\, dt \tag{1.2}$$

and the symbol * indicates the complex conjugate if E is a complex function. If we consider the complex function $E(t)$ as the functional representation of the dependence of the electric field on time and we make it interfere with a delayed replica $E(t-\tau)$, we can write the interferogram $U(\tau)$ measured on a detector as the intensity I of the overlap of $E(t)$ and $E(t-\tau)$ integrated in the time interval $[t_1, t_2]$ [1]:

$$\begin{aligned}
U(\tau) &= \int_{t_1}^{t_2} I\, dt \propto \int_{t_1}^{t_2} \left[\mid E(t) + E(t-\tau) \mid^2\right]\, dt = \\
&= \int_{t_1}^{t_2} \left[\mid E(t) \mid^2 + \mid E(t-\tau) \mid^2 + E^*(t)E(t-\tau) + E(t)E^*(t-\tau)\right]\, dt = \\
&= \int_{t_1}^{t_2} \left[\mid E(t) \mid^2 + \mid E(t-\tau) \mid^2\right]\, dt + \\
&+ \int_{t_1}^{t_2} \left[E^*(t)E(t-\tau) + E(t)E^*(t-\tau)\right]\, dt = \\
&= C_0 + 2\,\mathrm{Re}\left[\langle E^*(t)E(t-\tau)\rangle\right]
\end{aligned} \tag{1.3}$$

As it can be seen from equation 1.3 taking apart a constant term (called C_0) which do not depend on τ, the integral $U(\tau)$ is equal to $2\,\mathrm{Re}\left[\langle E^*(t)E(t-\tau)\rangle\right]$ which corresponds to the real part of the autocorrelation $\gamma(\tau)$ defined in equation 1.2. This means that, if we consider the real part of the $\gamma(\tau)$, it

[1] In optics the intensity is defined as the amplitude of the Poynting vector $\vec{S} = \frac{c}{4\pi}\left(\vec{E} \wedge \vec{H}\right)$ where c is the speed of light, $\vec{E}$ is the electric field and $\vec{H}$ is the magnetic field. For a plane wave the amplitude of the Poynting vector is $S = \frac{c}{4\pi}\sqrt{\frac{\epsilon}{\mu}} \mid \vec{E} \mid^2$ where ϵ is the dialectric constant and μ is the magnetic permeability: therefore the intensity is proportional to the modulus square of the electric field [10].

corresponds to the interferogram of the two replicas of the electric field $E(t)$ and $E(t-\tau)$ as function of the relative delay τ between the two. Moreover, according to the physical interpretation of the $E(t)$ function as an electric field, we have that the real part of $S(f)$ is the power spectral density of the electric field E and therefore it is the frequency spectrum of the optical radiation. From now on we will consider $\gamma(\tau)$ and $S(f)$ as real functions and by definition the frequency spectrum $S(f)$ and the interferogram $\gamma(\tau)$ are functions belonging to $L^1(\mathbb{R})$ because they are integrable on $\mathbb{R}$. Therefore we can invert equation 1.1:

$$S(f) = \int_{-\infty}^{+\infty} \gamma(\tau) e^{-i2\pi\tau f}\, d\tau \tag{1.4}$$

because $S(f)$ and $\gamma(\tau)$ belong to $L^1(\mathbb{R})$ and for this reason they satisfy the necessary conditions for the inversion. The expressions $\int_{-\infty}^{+\infty} S(f)e^{i2\pi\tau f}\, df$ from 1.1 and $\int_{-\infty}^{+\infty} \gamma(\tau)e^{-i2\pi\tau f}\, df$ from 1.4 corresponds respectively to the Inverse Fourier Transform (IFT) of $S(f)$ and the Fourier Transform (FT) of $\gamma(\tau)$ in $L^1(\mathbb{R})$ [11].

Equation 1.4 states that the FT of the interferogram $\gamma(\tau)$ of the electric field E is equal to the spectrum of E. Therefore if we acquire the interferogram of the incoming electromagnetic radiation and then we take the FT, we obtain the frequency spectrum: this is the basis of FT Spectroscopy.

To acquire the interferogram of the incoming radiation we need an interferometer which has the role to split the incoming electric field into two replicas $E(t)$ and $E(t-\tau)$ and to control the relative temporal delay τ between them.

1.2.1 The Michelson interferometer

The most common configuration for an optical interferometer is the Michelson interferometer invented by Albert Abraham Michelson and used in 1887 in the famous Michelson-Morley experiment for the attempt to detect the existence of the luminiferous ether [12]. Figure 1.3 shows the scheme of the Michelson interferometer: it relies on a 50-50 beam splitter which reflects 50% of the incoming light and transmits the other 50%. The beam splitter is tilted at 45° in order to obtain two replicas of the electric field: one in the upper branch (at 90° with respect to the direction of propagation of the incoming electric field) and the other in the right branch. These two replicas (indicated in red and blue in Figure 1.3) are back reflected by two perpendicular mirrors and then they impinge again on the beam splitter. The light transmitted from the upper branch and the light reflected from the right branch interfere on the detector as shown in Figure 1.3. Mirror M_2 can be translated in order to change the path of the right branch: in this way the two replicas of the electric field which interfere on the detector

have a relative phase difference which depends on the position of the translating mirror. If we consider a plane wave with obscillation frequency f and amplitude A_0, we have that the temporal evolution of the electric field can be written in this way:

$$E(t) = A_0 \cdot e^{-i2\pi ft} \tag{1.5}$$

If the plane wave is delayed because of a different optical path, we have:

$$E(t-\tau) = A_0 \cdot e^{-i2\pi f(t-\tau)} \tag{1.6}$$

where τ is the temporal delay. If we consider an incoming electric field E_{in} as a plane wave oscillating with a frequency f, we have to deal with the interference between two replicas as described by equations 1.5 and 1.6; in this case the intensity I which impinges on the detector is:

$$\begin{aligned} &I(\tau) \propto \mid E(t) + E(t-\tau) \mid^2 = \\ &= \mid E(t) \mid^2 + \mid E(t-\tau) \mid^2 + E^*(t)E(t-\tau) + E(t)E^*(t-\tau) = \\ &= 2\cdot \mid A_0 \mid^2 + \mid A_0 \mid^2 \cdot e^{i2\pi f\tau} + \mid A_0 \mid^2 \cdot e^{-i2\pi f\tau} = 2\cdot \mid A_0 \mid^2 \cdot [1 + \cos(2\pi f\tau)] \end{aligned} \tag{1.7}$$

In reality the detector measures the integral of the intensity I over time, but in this case it would simply result in a multiplication of the equation 1.7 by a constant factor. Thus equation 1.7 gives us the mathematical expression of the interferogram: if the phase $2\pi f\tau = n2\pi$ $(n \in \mathbb{Z})$ we have constructive interference, if the phase $2\pi f\tau = (2n+1)\pi$ $(n \in \mathbb{Z})$ we have destructive interference.

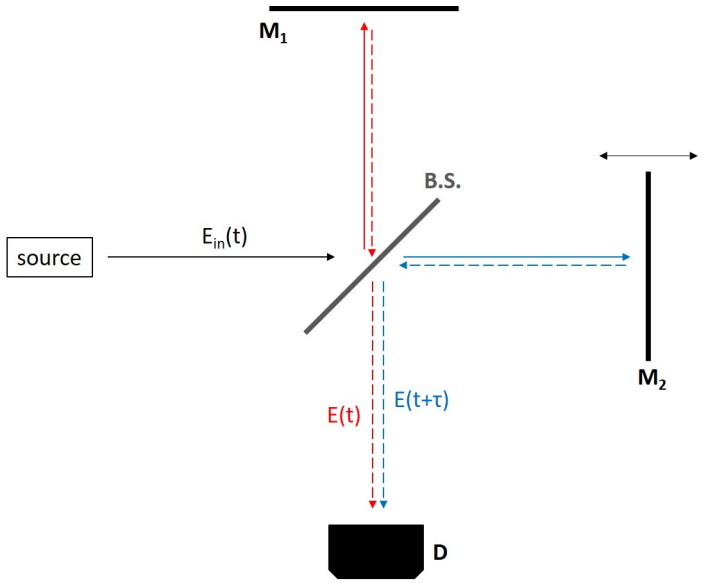

Figure 1.3: Scheme of the Michelson interferometer. Thanks to the beam splitter ($B.S.$) the incoming electric field $E_{in}(t)$ is splitted into two replicas (one reflected on the upper branch, in red, and the other transmitted on the right branch, in blue) which are reflected by two mirrors (M_1 and M_2) and then they interfere on a detector (D). The position of one of the two mirrors (M_2) can be changed to control the optical path difference between the two branches and therefore the temporal delay τ between the two replicas $E(t)$ and $E(t+\tau)$.

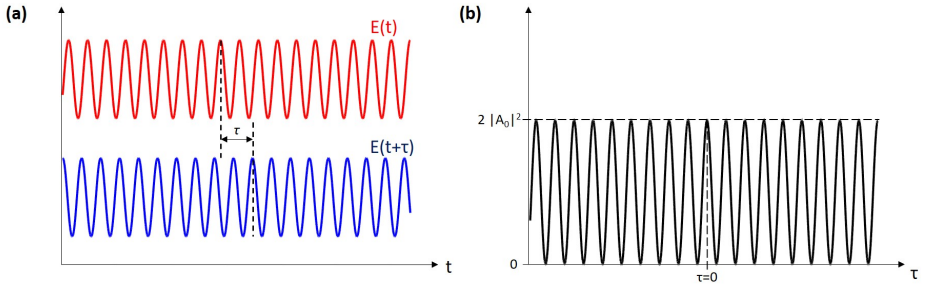

Figure 1.4: (a): example of two replicas of the electric field E (described as a plane wave) with a relative delay τ. The amplitudes of the two replicas are shifted for clarity. (b): intensity of the interference of the two replicas shown in (a) which impinges on the detector as a function of the delay τ.

If we consider the incoming electric field E_{in} as a broadband signal we can write it as:

$$E_{in} = A(t) \cdot e^{-i2\pi f_0 t} \tag{1.8}$$

where $A(t)$ is the envelope and f_0 is the carrier frequency. We can write the energy U measured by the detector integrating the intensity on time t [13]

in an interval $[t_1, t_2]$:

$$\begin{aligned}
U(\tau) &= \int_{t_1}^{t_2} I\, dt \propto \int_{t_1}^{t_2} \mid A(t)\cdot e^{-i2\pi f_0 t} + A(t-\tau)\cdot e^{-i2\pi f_0 (t-\tau)} \mid^2 \, dt = \\
&= \int_{t_1}^{t_2} \left(\mid A(t) \mid^2 + \mid A(t-\tau) \mid^2 \right) dt + \\
&+ \int_{t_1}^{t_2} \left(A(t)\cdot A^*(t-\tau)\cdot e^{-i2\pi f_0 \tau} + A^*(t)\cdot A(t-\tau)\cdot e^{i2\pi f_0 \tau} \right) dt = \\
&= \frac{C_0}{2} + \frac{C_0}{2} + 2\,\mathrm{Re}\left[\int_{t_1}^{t_2} \left(A^*(t)\cdot A(t-\tau)\cdot e^{i2\pi f_0 \tau} \right) dt \right] = \\
&= \frac{C_0}{2} + \frac{C_0}{2} + 2\cdot C(\tau)
\end{aligned} \tag{1.9}$$

where we have put $\int_{t_1}^{t_2} \mid A(t) \mid^2 \, dt = \int_{t_1}^{t_2} \mid A(t-\tau) \mid^2 \, dt = \frac{C_0}{2}$ and we recognize that the third term $2\,\mathrm{Re}\left[\int_{t_1}^{t_2} \left(A^*(t)\cdot A(t-\tau)\cdot e^{i2\pi f_0 \tau} \right) dt \right] = 2\cdot C(\tau)$ is the only τ-dependent term.
If the two replicas are not delayed ($\tau = 0$) $C(\tau) = \frac{C_0}{2}$ and we get:

$$U(\tau) = \frac{C_0}{2} + \frac{C_0}{2} + 2\frac{C_0}{2} = 2\cdot C_0 \tag{1.10}$$

If the two replicas have a relative phase $-\frac{\pi}{2} + 2n\pi \leq 2\pi f_0 \tau \leq +\frac{\pi}{2} + 2n\pi$ we have $0 \leq C(\tau) \leq \frac{C_0}{2}$ and therefore:

$$C_0 \leq U(\tau) \leq 2\cdot C_0 \tag{1.11}$$

If the two replicas have a relative phase $\frac{\pi}{2} + 2n\pi < 2\pi f_0 \tau < \frac{3\pi}{2} + 2n\pi$ we have $-\frac{C_0}{2} < C(\tau) < 0$ and therefore:

$$0 < U(\tau) < C_0 \tag{1.12}$$

If the two envelopes $A(t)$ and $A(t+\tau)$ are well separated in time they do not overlap in the intergral of the third term and we have:

$$U(\tau) = \frac{C_0}{2} + \frac{C_0}{2} + 0 = C_0 \tag{1.13}$$

From the equations 1.10, 1.11, 1.12 and 1.13 we can easily understand the behaviour of U as a function of the delay τ: it has its maximum when $\tau = 0$, then it oscillates around the zero-delay until the absolute value of τ is greater than the temporal coherence of the envelopes $A(t)$ and $A(t+\tau)$ and it stabilizes at half of the oscillation dynamics. The oscillations of the interferogram before the stabilization at half of the dynamics are also refferred to as **fringes**.

Figure 1.5 (b) shows the dependence on the delay τ of the energy U described by equation 1.9.

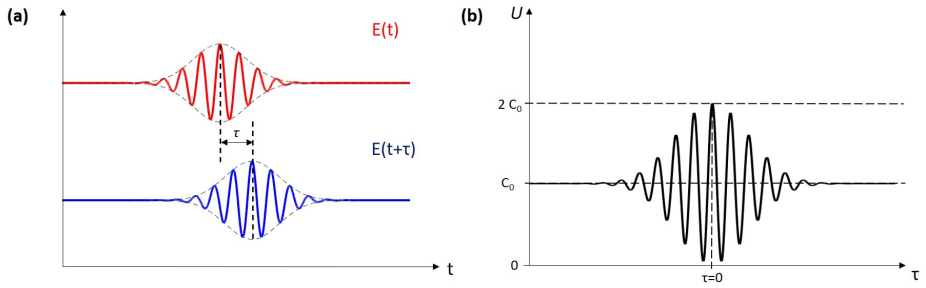

Figure 1.5: (a): example of two replicas of the electric field E in the broadband case. Each one of the two replicas oscillates with the frequency f_0 of the carrier and has an amplitude A which depends on time (in this figure A is considered as a Gaussian envelope). The amplitudes of the two replicas are shifted for clarity. (b): energy U related to the intensity of the interference of the two replicas shown in (a) which is integrated on the detector as a function of the delay τ.

The two examples described by equations 1.7 (see Figure 1.4 (b) as reference) and 1.9 (see Figure 1.5 (b) as reference) are representative of a narrowband-spectrum signal and a broadband-spectrum signal respectively. The plane wave described by equation 1.5 and oscillating with a frequency f has a spectrum which is a line at frequency f, while the broadband signal described by equation 1.8 has a spectrum which is centered around the carrier frequency f_0 and which covers more frequencies. These two examples allow us to understand this important property: the interferogram obtained from the interference of two replicas of a narrowband signal is a periodic function which continues to oscillate even at very large delays (positive or negative) with respect to $\tau = 0$ as it is shown by Figure 1.4 (b), the interferogram obtained from the interference of two replicas of a broadband signal has appreciable oscillations only around $\tau = 0$ and then it settles at half of the maximum as it is shown by Figure 1.5 (b).

To arrive to this conclusion we have considered only examples involving coherent light, infact equations 1.5 and 1.8 are representative of a monochromatic laser and a pulsed laser respectively: anyway the property we have demonstrated with these simple examples is also valid for incoherent light.

1.2.2 The advantages of FT spectroscopy

The very known advantages of FT spectroscopy with respect to the dispersive spectroscopy based on prisms or gratings reside in:

- Jacquinot advantage or throughput advantage
- Fellgett advantage or multiplex advantage

The Jacquinot advantage starts from the fact that in an ideal lossless optical system, the brightness of an object equals the brightness of the image: this is because of the conservation of the "étendue" (or "throughput") [2]. In a real optical system with a limited aperture stop [3] the étendue is limited by the aperture stop itself; therefore grating spectrometers have smaller étendue with respect to FT interferometers because in gratings the light is spatially filtered by linear slits (for the formal demonstration of this statement see the Jacquinot advantage discussion on [15]).

The Fellgett advantage comes from the multiplex principle. This principle asserts that the observation time $T_{\delta\sigma}$ of a small band of width $\delta\sigma$ in a broad spectrum from frequency σ_1 to σ_2 ($\Delta\sigma = \sigma_2 - \sigma_1$) is:

$$T_{\delta\sigma} = \frac{T_{\Delta\sigma}}{\Delta\sigma/\delta\sigma} \tag{1.14}$$

where $T_{\Delta\sigma}$ is the total time required to scan the spectrum from σ_1 to σ_2. This is the principle the grating spectrometers are based on. Therefore the signal-to-noise ratio for a grating is:

$$(S/N)_G \propto \sqrt{T_{\delta\sigma}} \tag{1.15}$$

In an interferometer (FT spectrometer) all the small bands $\delta\sigma$ are observed at the same time; therefore if the total time of the scanning is $T_{\Delta\sigma}$, each small band is observed for a time $T_{\Delta\sigma}$ and the signal-to-noise ratio is:

$$(S/N)_I \propto \sqrt{T_{\Delta\sigma}} \tag{1.16}$$

From equations 1.15 and 1.16 we get the Fellget advantage:

$$\frac{(S/N)_I}{(S/N)_G} = \sqrt{\frac{T_{\Delta\sigma}}{T_{\delta\sigma}}} = \sqrt{\frac{\Delta\sigma}{\delta\sigma}} \tag{1.17}$$

This shows that the signal-to-noise ratio is better in an FT spectrometer than in a grating spectrometer. In reality in equations 1.15 and 1.16 we have assumed that the signal-to-noise ratio depends only on the observation time and not on the noise of the source: this assumption is valid if the noise in the detector is the prevailing one and it is independent on the shot noise of the photons of the source. This situation occurs in the infrared region

[2] The étendue $\mathscr{E}$ of the radiation field emitted by a surface dA and confined in a solid angle $d\Omega$ forming an angle θ with respect to the normal to the surface is defined as

$$\mathscr{E} = dA \cdot \cos(\theta) \cdot d\Omega$$

The étendue is an invariant property of the light beam.

[3] The Aperture Stop of an optical system is the actual physical component that limits the size of the maximum cone of rays (from an axial object point to a conjugate image point) that can be processed by the entire system [14].

in which the noise of the detectors is much higher than the noise of the sources. It can be demonstrated that if the shot noise prevails over the detector noise, as in the visible region, the signal-to-noise ratio is the same for the interferometer and the grating spectrometer and the Fellget advantage is lost (the demonstration of this is in [15]).

Anyway the Jacquinot and Fellgett advantages permit construction of interferometers having much resolving powers than dispersive instruments [16] because, in general, they assure an higher signal-to-noise ratio.

Together with the Jacquinot and Fellgett advantages FT spectroscopy offers the following advantages:

- the flexibility in spectral resolution which depends on the maximum scan delay [1]: the greater the maximum scan delay the better the resolution (see [16] for example)
- the possibility of parallel recording of the spectra of all pixels within a two-dimensional scene of an imaging system [17]

1.3 An ultrastable common-path interferometer: the TWINS

The Michelson interferometer presented in the subsection 1.2.1 is a basic but effective scheme of an interferometer; nevertheless it has problems to fulfill the necessary requirement in FT spectroscopy that the delay of the two replicas of the electric field must be controlled to within a fraction (1/100 or better) of the optical cycle (e.g., $2fs$ at $600nm$) [1]. In practice this means that the beam splitter and the two mirrors must be stabilized with a precision better than tens of nanometers and this ends up in a bulky setup.

In [18] the Translating-Wedge- Based Identical Pulses eNcoding System (TWINS) has been introduced; this system constitutes a common path birefringent interferometer that combines compactness, intrinsic interferometric delay precision, long-term stability and insensitivity to vibrations [1, 18, 17]. Figure 1.6 shows the scheme of the TWINS.

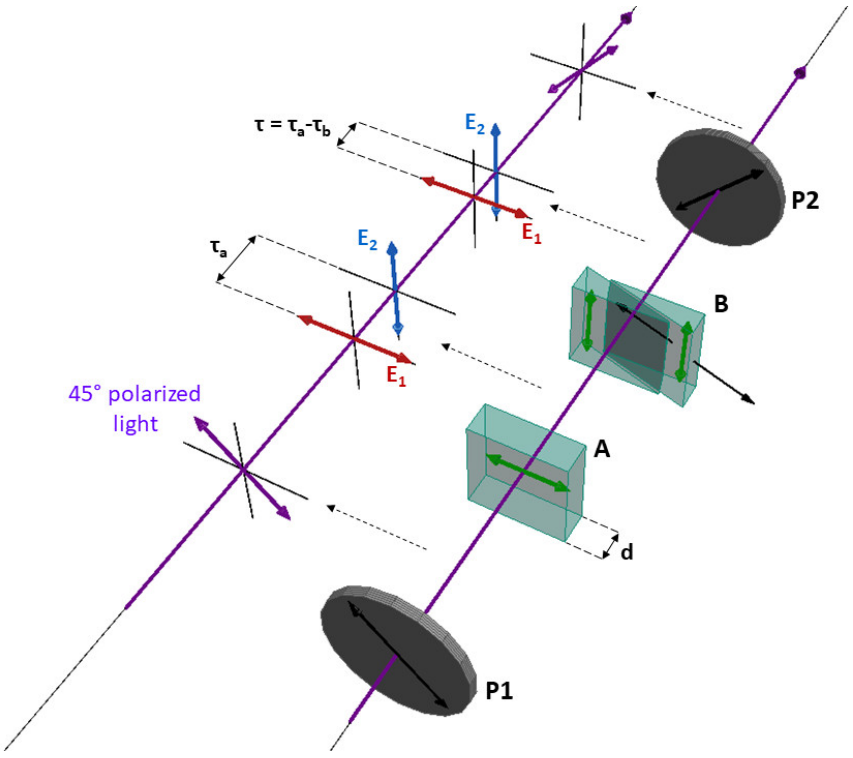

Figure 1.6: Scheme of TWINS. $P1$ and $P2$ are wire-grid polarizers with polarizing axis along the 45° and −45° direction as shown by the black arrows. A and B are two birefringent blocks with optical axis at 0° (horizontal direction) and 90° (vertical direction) as depicted by the green arrows. d is the width of each one of the two birefringent blocks. The width of block B can be changed translating one of the two wedges in the directions indicated by the black arrows. E_1 and E_2 are the two replicas of the electric field generated in the blocks and τ_a and τ_b are the relative delays determined by the birefringence of the crystals. The purple arrow indicates the propagation direction of a paraxial ray.

TWINS is composed by two uniaxial birefringent crystal blocks (A and B in figure) with thickness d and with crossed optic axis (green arrows in Figure 1.6). Block B is divided into two wedges: one of these can be translated by a motorstep in the direction parallel to the cut (as shown by the black arrows in Figure 1.6). In this way the width of block B can be changed with respect to the thickness d. The A and B block are located between two polarizers: one in front ($P1$ in figure) and the other at the end ($P2$ in figure). In Figure 1.6 the two polarizers are crossed ($P1$ with the polarizing axis at 45° and $P2$ with the polarizing axis at $-45°$) but they can be with parallel polarizing axis: if they are parallel the delay $\tau = 0$ in the interference coincides with the maximum of the interferogram (as shown in Figure 1.5 (b) for the Michelson interferometer), if they are crossed the $\tau = 0$ condition coincides with the minimum (the situation is reversed with respect to the one shown in Figure 1.5 (b) because for $\tau = 0$ we have $U = 0$, destructive interference).

Considering as the light propagation direction the one indicated by the purple arrow in Figure 1.6, first of all the incoming light is polarized at 45° by the polarizer $P1$. Then the light enters the block A which has an optic axis along the horizontal direction; due to the birefringence of the material the 45°-polarized electric field is splitted into two replicas (the E_1 and E_2 replicas indicated in the figure).

E_1 has a polarization along the horizontal direction and therefore it oscillates along the optic axis of the crystal experiencing a refractive index $n_\parallel$ (ordinary refractive index), E_2 has a polarization along the perpendicular direction and therefore it oscillates perpendicularly with respect to the optic axis of the crystal experiencing a refractive index $n_\perp$ (extraorinary refractive index), $n_\perp \neq n_\parallel$ [4]. The difference in optical path between the two replicas in the A block is:

$$\Delta_a = \mid n_\perp - n_\parallel \mid \cdot d \qquad (1.18)$$

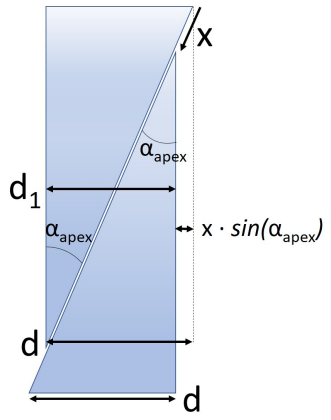

Figure 1.7: Scheme of the block B. x is the translation of the wedge (the positive direction is indicated by the arrow) and α_{apex} is the apex angle.

and therefore after the A block the two replicas have accumulated a relative delay:

$$\tau_a = \frac{\Delta_a}{c} = \frac{\mid n_\perp - n_\parallel \mid}{c} \cdot d \qquad (1.19)$$

[4] For an explanation of the birefringence properties see, for example, [14]

where c is the speed of light in vacuum.

The difference in optical path between the two replicas in the B block is:

$$\Delta_b = \mid n_\perp - n_\parallel \mid \cdot d_1 \tag{1.20}$$

where $d_1 = d - x \cdot \sin(\alpha_{apex})$ is the width shown in the scheme of Figure 1.7 for a positive translation x of the wedge and considering an apex angle α_{apex}. Therefore the relative delay accumulated by the two replicas due to the block B is:

$$\tau_b = \frac{\Delta_b}{c} = \frac{\mid n_\perp - n_\parallel \mid}{c} \cdot d_1 \tag{1.21}$$

As the block B has the optic axis in the vertical direction, the E_1 replica now experiences the extraordinary refractive index $n_\perp$ and the E_2 replica now experiences the ordinary refractive index $n_\parallel$: the situation is reversed with respect to the propagation in block A.
Therefore the total relative delay between the two replicas before the second polarizer ($P2$) is:

$$\tau = \tau_a - \tau_b = \frac{\mid n_\perp - n_\parallel \mid}{c} \cdot (d - d_1) = \frac{\mid n_\perp - n_\parallel \mid}{c} \cdot x \cdot \sin(\alpha_{apex}) \tag{1.22}$$

Then, after the polarizer $P2$, the two replicas of the electric field are projected on the same polarization direction and they can interfere on a detector according their phase displacement $2\pi f_0 \tau$ as described by equation 1.9.

Equation 1.22 clearly shows the linear dependence of the interference delay τ from the translation x of the wedge: the translation x can be positive (direction indicated in Figure 1.7 with respect to the 0 when $d_1 = d$) or negative and therefore the wedges structure allows us to scan the varius delays of interference.

As can be seen from equations 1.18 and 1.20 the difference in optical path between the two replicas depends on the difference between the two refractive indices in the crystals and on the widths d and d_1 the two replicas pass through: therefore the interference is determined only by the birefringence properties of the blocks A and B but anyway the pathlenghts of the two replicas in the TWINS interferometer are exactly the same. This means that all the movements and mechanical instabilities of the physical component of the TWINS are experienced by both of the two replicas: this solves the stability problems necessary to perform FT spectroscopy.

1.4 Widefield imaging

Widefield is an imaging technique in which an image the sample is acquired at once. For this reason the entire Field of View (FOV) on the sample has to be uniformly illuminated and the imaging system has to be designed in order to produce an image on a position-sensitive detector [5]. There are two possible configurations in widefield imaging: reflection configuration and transmission configuration. In the reflection configuration the sample is illuminated from above as depicted in Figure 1.8 (*a*), instead in the transmission configuration the sample is illuminated from the bottom as depicted in Figure 1.8 (*b*).

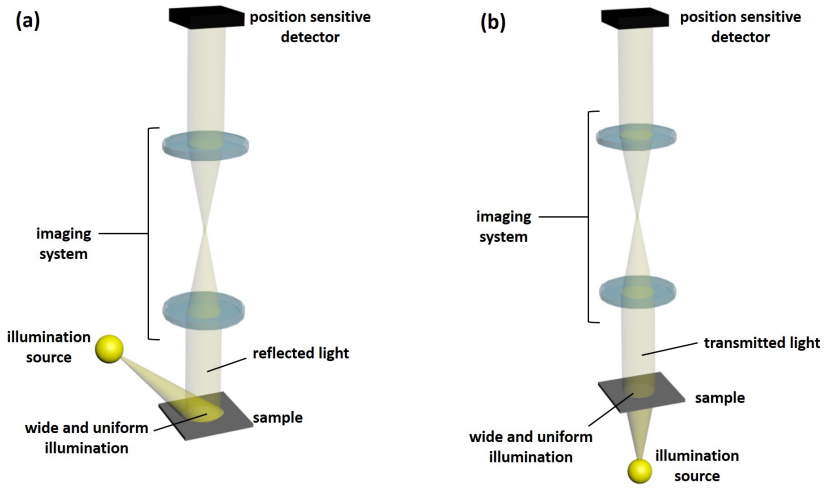

Figure 1.8: (*a*): widefield reflection scheme. (*b*): widefield transmission scheme.

Another image acquisition technique is the raster scanning (which is also called "whiskbroom") in which the sample is illuminated with a tightly focused light beam that is scanned in two dimensions to obtain the entire image [6] (see [4] and [20] as reference). Raster scanning is a point-scanning technique because one point at time is illuminated and integrated on the detector: scanning all the points on the FOV, the system is able to build the entire image. Figure 1.9 depicts the conceptual scheme behind the raster scanning imaging technique. The scanning of the tightly foucused light beam over the stationary sample is determined by a moving mirror (called scanning mirror in Figure 1.9) which can rotate in the two dimensions; alternatively a point-scanning technique can be realized without scanning mirror and

[5] A position-sensitive detector is a two-dimensional matrix of small elements (pixels) each one sensitive to the amount of incoming light. Therefore such a device is able to detect the spatial intensity distribution of light on the pixels plane.

[6] In optical systems which allow optical sectioning (such as confocal microscopes) a 3D-scanning can be performed to obtain 3D images of the sample.

simply moving the sample. Then the setup relies on a de-scanning mirror which rotates in such a way that the light coming from the sample is always directed towards a single element detector [7]: in this way no position sensitive camera is needed because the scanned point coordinates information can be deduced from the rotation control of the scanning mirror and de-scanning mirror.

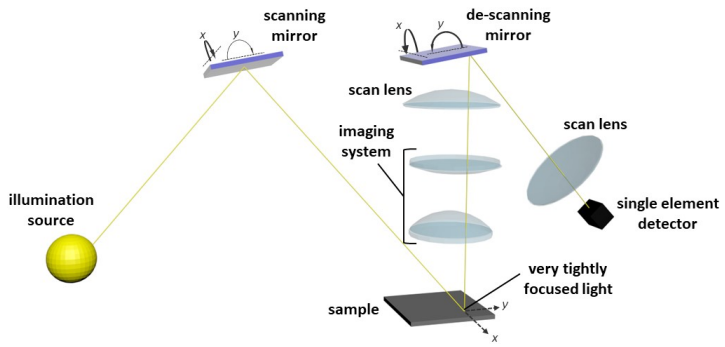

Figure 1.9: Raster scanning scheme.

Figure 1.9 illustrates the raster scanning scheme in reflection configuration: the transmission geometry can be used in a scanning system but it is rarely found in practice [20].

There is another technique similar to whiskbroom but which relies on the scanning of an entire line on the sample (line-scanning) instead of a single point: this is called "pushbroom" (see [4] as reference).

[7] In practice, in most of the microscopes which work in the reflection geometry, the scanning and de-scanning is performed by a single moving mirror (see [20])

1.5 FT hyperspectral widefield imaging with TWINS

In sections 1.2, 1.3 and 1.4, the FT spectroscopy principles, the TWINS ultrastable interferometer and the widefield imaging conception has been presented: now in this section the applications of these concepts in hyperspectral imaging are discussed.

FT hyperspectral imaging relies on the acquisition of an image for each delay of interference: the collection of all these frames is called **temporal hypercube** and it can also be seen as a single image on which each pixel contains an entire interferogram. The principle behind FT hyperspectral imaging is that, taking the FT of each interferogram contained in the temporal hypercube, the final spectral hypercube is obtained: all these concepts will be studied in chapter 2.

In an acquisition system thought to perform FT hyperspectral imaging based on TWINS interferometer, each one of the frames is acquired for a particular translation of the wedge (for a particular delay of the replicas of the electric field determined by birefringence properties). Figure 1.10 represents the conceptual scheme of an imaging system which includes the TWINS interferometer.

In section 1.4 we have seen that in a widefield imaging system a large area of the sample is illuminated and also the optical detection system of an ordinary imaging device is designed in order to collect the light within a certain numerical aperture. This means that the light going through the TWINS interferometer in an imaging system is not only composed by paraxial rays as the one considered in section 1.3 and shown in Figure 1.6: the rays can impinge on the birefringent plates A and B with a certain angle α and this determines a correction to the relative phase $2\pi f\tau$ between two replicas of the electric field.

In a 2-dimensional representation the light coming from a point in the FOV, which forms an angle α_0 with respect to the optical axis (see Figure 1.10 for the definition of α_0), is a bundle of rays which propagates at various angles around α_0 with a range $\Delta\alpha$ [17]: for this reason we can uniquely identify a particular ray bundle by its own pair $\{\alpha_0, \Delta\alpha\}$ with α_0 *central ray angle* and $\Delta\alpha$ *angle range* (the range between the angles of the marginal rays of the bundle with respect to the central ray). We have to consider an entire pencil of rays (and not a single ray) because an imaging system is characterized by a certain numerical aperture determined by a finite aperture stop therefore it is able to collect an entire bundle of light coming from a single point.

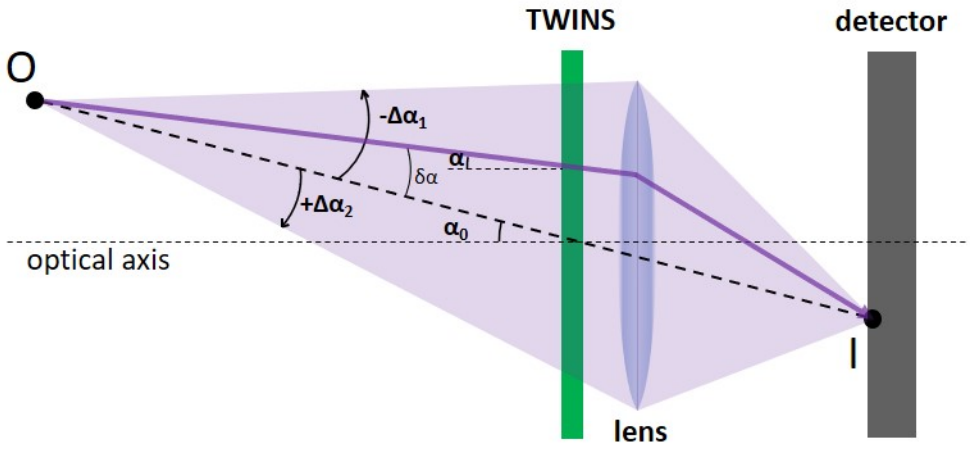

Figure 1.10: 2-dimensional schematic representation of an FT hyperspectral imaging system based on TWINS interferometer. O: point in the FOV on the object plane. I: point on the detector in the image plane. α_0: angle the line from O to I forms with respect to the optical axis. The purple shaded area represents the ray bundle defined by the angle range $\Delta\alpha = [-\Delta\alpha_1; \Delta\alpha_2]$ and collected by the imaging system. The purple line indicates a generic ray inside the bundle which forms an angle $\alpha = \alpha_0 + \delta\alpha$ with respect to the optical axis. The lens represents the finite aperture stop of the imaging system. The green rectangle is a schematic 2-D depiction of the TWINS interferometer illustrated in Figure 1.6.

Therefore we can write the angle α formed by the single ray (belonging to a certain light bundle) with respect to the paraxial axis in this way:

$$\alpha = \alpha_0 + \delta\alpha \qquad (\text{with } -\Delta\alpha_1 \leq \delta\alpha \leq \Delta\alpha_2) \tag{1.23}$$

where we have considered $\delta\alpha$ as the angle variation with respect to α_0 inside the range $\Delta\alpha = [-\Delta\alpha_1; \Delta\alpha_2]$ of the bundle. Therefore we can uniquely identify a particular ray inside the bundle $\{\alpha_0, \Delta\alpha\}$ with the pair $\{\alpha_0, \delta\alpha\}$. In the TWINS interferometer, each one of these rays determines an electric field replicas pair with a relative phase:

$$\phi = 2\pi f\tau + \phi_0 + \delta\phi \qquad (\text{with } -\Delta\phi_1 \leq \delta\phi \leq \Delta\phi_2) \tag{1.24}$$

where $2\pi f\tau$ is the relative phase determined by the delay τ controlled with the translation of the wedge (as described by equation 1.22) and $\phi_0 + \delta\phi$ is the correction to the relative phase determined by the fact that the ray impinges on the birefringent plates at an angle $\alpha_0 + \delta\alpha$. We call ϕ_0 the phase correction due to angle α_0 and $\delta\phi$ the phase correction due to the angle variation $\delta\alpha$: in this way, as $\delta\alpha$ is limited in a range $\Delta\alpha$, we have that $\delta\phi$ is limited inside a range $\Delta\phi = [-\Delta\phi_1; \Delta\phi_2]$. From this statement we can understand that a ray bundle $\{\alpha_0, \Delta\alpha\}$ can be uniquely identified by the pair $\{\phi_0, \Delta\phi\}$ and a single ray $\{\alpha_0, \delta\alpha\}$ of that bundle by $\{\phi_0, \delta\phi\}$. With equation 1.24 we don't want to draw the matemathical dependence of ϕ on the angle α of incidence of the single ray (for this discussion see [17]) but

we want only to point out the fact that the relative phase between the two replicas depends not only on the wedge translation but also on the position of the object point at an angle α_0 with respect to the optical axis and on the angle variation $\delta\alpha$ within the bundle range $\Delta\alpha$. We have to mark the fact that, if we fix the angle α of incidence, the phase correction $\phi_0 + \delta\phi$ is linear with respect to the wedge translation x.

The phase correction $\phi_0 + \delta\phi$ is responsible of a delay shift of the two replicas interferogram because the overall delay τ_ϕ can be written as:

$$\tau_\phi = \frac{\phi}{2\pi f} = \tau + \frac{\phi_0 + \delta\phi}{2\pi f} = \tau + \tau_{shift} \tag{1.25}$$

τ is a function of the wedge translation x (equation 1.22) but also τ_{shift} depends on x as well as α:

$$\tau_\phi(x, \alpha) = \tau(x) + \tau_{shift}(x, \alpha) \tag{1.26}$$

where:

$$\begin{cases} \tau_{shift}(x, \alpha = 0) = 0 \\ \tau_{shift}(x, \alpha \neq 0) \neq 0 \end{cases} \tag{1.27}$$

Equation 1.26 tells us that, if the ray impinges on the TWINS at an angle $\alpha \neq 0$, the delay τ_ϕ is not anymore only the nominal delay τ associated to the wedge translation x (as we have seen in section 1.3) because there's a correction term τ_{shift}. This means that the association of the wedge scanning to a delay scanning is not unique for all the rays collected by the imaging system but it depends contemporarly on the wedge position x and on the angle α of ray incidence. As shown in Figure 1.10, the light coming from a point O in the FOV is sent to a point I on the detector; therefore all the rays within the bundle are all integrated on the conjugated point on the detector. In a FT hyperspectral imaging acquisition this means that on that point we have the sum of the electric fields which, as it can be seen from equation 1.26, are related to a different delay axis although they are built on a single set of translations $\{x\}_{set}$ of the wedge. Moreover in a widefield geometry the optical system collects light from all the points in the FOV and creates the correspondent image on the camera: therefore on the image plane each point derives from the integration of its associated light bundle characterized by its own *central ray angle* α_0. These facts determines two fundamental problems as discussed in [1] and [17]:

- hyperbolic phase pattern across the FOV
- reduction of interferogram fringes visibility ν on each point of the detector

The phase pattern is due to the fact that the ray bundles coming from different points in the FOV are characterized by different central ray angles

α_0 and this determines a dependence of the phase correction ϕ_0 (see equation 1.24) on the particular position of the FOV. As it is shown in [1], the 2D spatial map of the phase ϕ_0 determined by the uniaxial birefringent crystal of the TWINS is characterized by an hyperbolic pattern.

As it is stated in [17] the fringes visibility reduction is determined by the phase span $\Delta\phi$. This is a direct cause from the fact that on a single point of the detector we have the sum of the electric field replicas related to all the rays within the particular bundle $\{\phi_0, \Delta\phi\}$. In order to study the dependence of the fringes visibility on $\Delta\phi$ we can consider each one of the rays within the bundle as a monochromatic plane wave with frequency f. We can make the assumpion that the polarization is the same for all the electric fields related to these rays when they impinge on the detector point and we can consider the ray phase correction $\delta\phi$ as uniformly distributed in the interval $\Delta\phi = [-\Delta\phi_1; \Delta\phi_2]$. Starting from these hypothesis, we call $E_{\{\phi_0,\delta\phi\}}(2\pi ft + \phi_r)$ and $E_{\{\phi_0,\delta\phi\}}(2\pi ft + \phi + \phi_r)$ the two replicas of the electric field associated to a particular ray $\{\phi_0, \delta\phi\}$ expressed as functions of the phase $2\pi ft + \phi_r$: ϕ_r is the phase difference of $E_{\{\phi_0,\delta\phi\}}(2\pi ft + \phi_r)$ with respect to the first replica $E_{\{\phi_0,\delta\phi=0\}}(2\pi ft)$ of the central ray. In this simple model the interferogram measured on the detector point in the time interval $[t_1, t_2]$ is:

$$U(\tau_\phi) = \\ = \int_{t_1}^{t_2} \left| \int_{-\Delta\phi_1}^{+\Delta\phi_2} \left[E_{\{\phi_0,\delta\phi\}}(2\pi ft + \phi_r) + E_{\{\phi_0,\delta\phi\}}(2\pi ft - \phi + \phi_r) \right] d(\delta\phi) \right|^2 dt \tag{1.28}$$

where we have written the integral from $-\Delta\phi_1$ to $+\Delta\phi_2$ in order to sum all the replicas belonging to the different rays inside the bundle $\{\phi_0, \Delta\phi\}$. ϕ_r depends on $\delta\alpha$ and therefore in the integral in equation 1.28 it depends on $\delta\phi$. To simplify the calculation we can neglect ϕ_r: this coincides with the assumption that the first replicas of the rays within the bundle see the same optical path independently on the incidence angle on the TWINS. This is reasonable as in a two-dimensional representation of the TWINS one of the two replicas pass through the birefringent blocks A and B without any dependence of the crystal refractive indices on the angle of incidence (see [1] for the details on this). As all the rays within the bundle are focused on the same detector point, we can reasonably consider all the first replicas reciprocally in phase.

The electric field associated to a plane wave can be written as:

$$E(\varphi) = A_0 e^{-i\varphi} \tag{1.29}$$

where φ is its overall phase and A_0 is its amplitude. Substituting equation

1.29 in equation 1.28, ϕ with the expression 1.24, and neglecting ϕ_r, we get:

$$U(\tau_\phi) = \\ = \int_{t_1}^{t_2} \left| \int_{-\Delta\phi_1}^{+\Delta\phi_2} \left[A_0 \cdot e^{-i(2\pi f t)} + A_0 \cdot e^{-i(2\pi f t - \phi_0 - \delta\phi - 2\pi f \tau)} \right] d(\delta\phi) \right|^2 dt \tag{1.30}$$

In this equation we have considered all the replicas of all the rays within the bundle with the same amplitude A_0. As the factors A_0 and $e^{-i(2\pi f t)}$ don't depend on $\delta\phi$, we can rewrite equation 1.30 in this way:

$$U(\tau_\phi) = \int_{t_1}^{t_2} \left| A_0^2 \right| \cdot \left| \int_{-\Delta\phi_1}^{+\Delta\phi_2} \left[1 + e^{i(\phi_0 + \delta\phi + 2\pi f \tau)} \right] d(\delta\phi) \right|^2 dt \tag{1.31}$$

From equation 1.31 we can calculate the expression of U as a function of τ and the phase span $\Delta\phi = [-\Delta\phi_1; \Delta\phi_2]$ [8]:

$$U(\tau) = |A_0|^2 \cdot \left| \Delta\phi_2 + \Delta\phi_1 - i e^{i(\phi_0 + 2\pi f \tau)} \cdot \left[e^{i\Delta\phi_2} - e^{-i\Delta\phi_1} \right] \right|^2 \cdot (t_2 - t_1) \tag{1.32}$$

We define the fringes visibility ν in agreement with the definition in [17]:

$$\nu(\Delta\phi_1, \Delta\phi_2) \doteq \frac{max\left\{U(\tau)\right\}_\tau - \langle U(\tau) \rangle_\tau}{\langle U(\tau) \rangle_\tau} \tag{1.33}$$

where the notations $max\left\{U(\tau)\right\}_\tau$ and $\langle U(\tau) \rangle_\tau$ indicate respectively the maximum and the mean of $U(\tau)$ calculated on the τ variable: for this reason ν is calculated as a function of the phase span $\Delta\phi = [-\Delta\phi_1; \Delta\phi_2]$.

Figure 1.11 shows the dependence of ν on $\Delta\phi_2$ (considering $\Delta\phi_1 = 0$) calculated substituting equation 1.32 in equation 1.33: this is the same result shown in [17]. As it can be seen the fringes visibility ν is almost 100% for small phase span ($|\Delta\phi_2 - \Delta\phi_1| < \pi$), then it decreases until it reaches 0% (at $|\Delta\phi_2 - \Delta\phi_1| = 2\pi$).

[8] We make the approximation that the phase correction $\phi_0 + \delta\phi$ is not dependent on the wedge translation x and therefore there is not a mathematical relation between τ and $\phi_0 + \delta\phi$. For this reason we can calculate U as a function of τ as τ_ϕ is simply obtained by the addition of a term τ_{shift} which does not depend on x in this approximation.

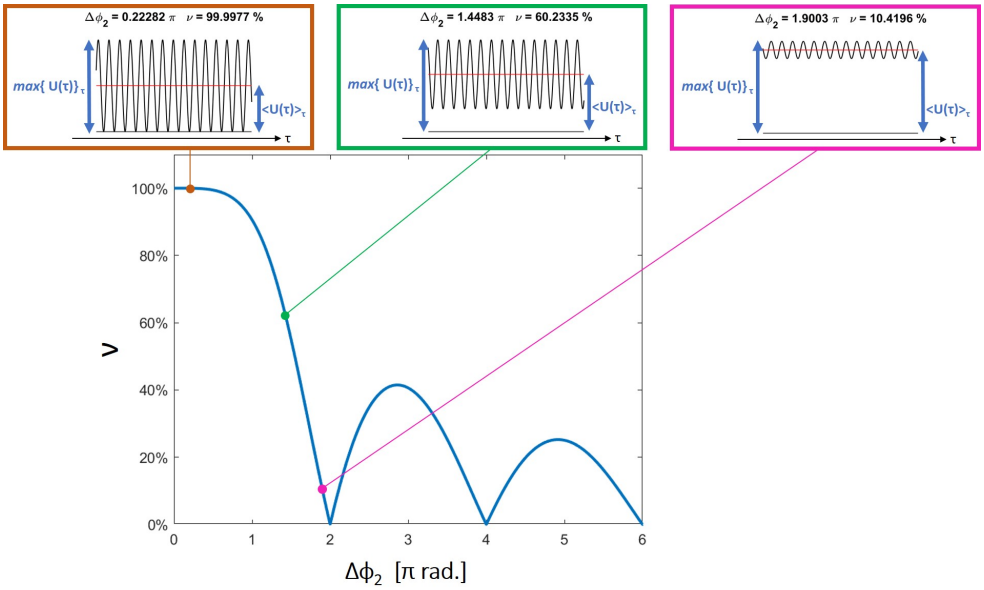

Figure 1.11: Fringes visibility ν as a function of $\Delta\phi_2$ (in multiple of π) considering $\Delta\phi_1 = 0$, $\phi_0 = 0$, $f = 500THz$ ($\lambda = 600nm$) and $\tau \in \left[-100 \times 5\mu m \times 0.29\frac{fs}{\mu m}; +100 \times 5\mu m \times 0.29\frac{fs}{\mu m}\right]$. In the panels at the top three interferogram for different values of $\Delta\phi_2$ are shown.

1.5.1 High-fringes visibility and Uniform Zero-path Delay configurations

The imaging system scheme shown in Figure 1.10 relies on a single lens. The imaging scheme used in microscopy is the 4f configuration depicted in Figure 1.12. As it can be seen this scheme relies on two elements: the objective and the tube lens. The objective (depicted in Figure 1.12 as a single lens) has the role to collect the cone of light (defined by its numerical aperture NA) from each point of the sample and it has to be located at a distance from the sample equal to f_1 which is the objective focal length. In this way the rays coming from a point of the sample are parallel after the objective: they are infinity conjugated. Then the tube lens has the role to focus the rays in a point at a distance equal to f_2 which is the tube lens focal length: therefore the tube forms an image of each point of the sample on the detector plane if it is located at a distance f_2.

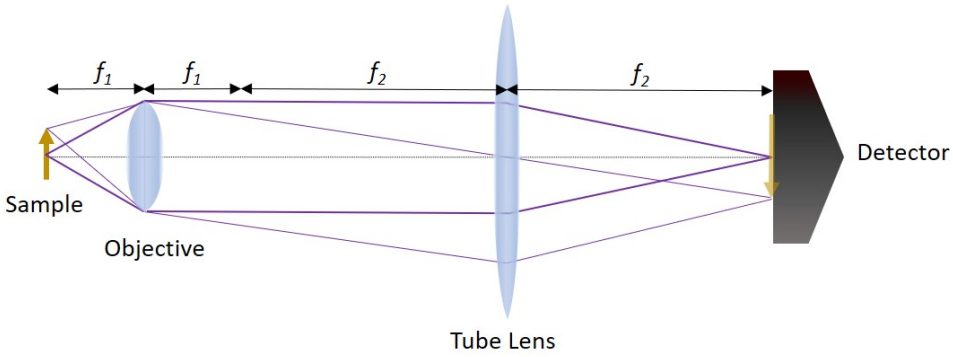

Figure 1.12: Scheme of the 4f configuration. f_1: focal length of the objective. f_2: focal length of the tube lens

The magnification M of the image of the sample on the detector plane in the 4f configuration is:

$$M = \frac{f_2}{f_1} \tag{1.34}$$

and the resolution $\delta\rho$ of such an optical system is given by the Abbe diffraction limit:

$$\delta\rho = \frac{\lambda}{2 \cdot NA} \tag{1.35}$$

where $NA = n \cdot \sin(\alpha_{max})$ is the objective numerical aperture (n is the refractive index of the objective surrounding medium and α_{max} is the maximum angle of the cone of light accepted by the objective) [20].

In a FT hyperspectral imaging system based on TWINS which relies on the 4f scheme there is the possibility to choose between the two different locations of the interferometer depicted in Figure 1.13 (a) and in Figure 1.13 (b). This choice ends up with two different configurations of the imaging system called high-visibility configuration and uniform zero-path delay (ZPD) configuration [1]. The high-visibility configuration is the one in which the TWINS interferometer is located between the objective and the tube lens. In this scheme all the rays belonging to a bundle that comes from a single point in the sample pass through the TWINS with the same angle because they are all parallel as shown in Figure 1.13 (a). In this way all the electric field replicas of these rays integrated as in equation 1.28 have a maximum phase shift $\Delta\phi = [-\Delta\phi_1, \Delta\phi_2]$ which is almost zero and this ends up in a high fringes visibility ν as defined in equation 1.33. We have to note that the different bundles coming from different points in the sample pass through the TWINS with different α_0 angles and therefore in this configuration the problem of the hyperbolic phase pattern across the FOV is not solved.

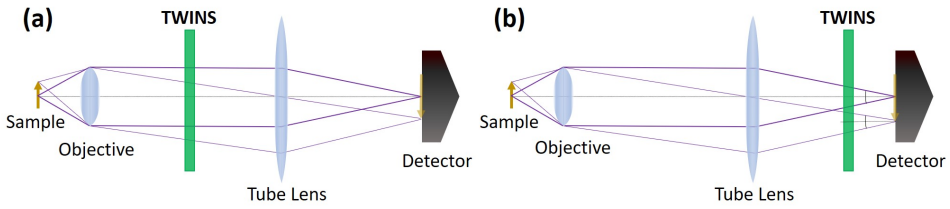

Figure 1.13: (a): high-visibility scheme in the FT hyperspectral imaging system based on TWINS in the case of a 4f configuration. (b): uniform ZPD scheme in the FT hyperspectral imaging system based on TWINS in the case of a 4f configuration.

The uniform ZPD configuration is obtained when the TWINS is located after the tube lens. In this scheme (see Figure 1.13 (b)) all the rays of a bundle pass through the interferometer with different angles α (as defined by equation 1.23) but with $\alpha_0 = 0$: therefore the rays integrated in a single point of the detector have on average an angle $\alpha = 0$ with respect the TWINS and this means that the integral on that detector point (see equation 1.32 for reference) is not dependent on ϕ_0 and therefore it is completely controlled by the delay τ imposed by the wedge translation x. As this situation is the same for all the bundles (and therefore for all the points on the detector), we have that all the pixels' interferograms acquired in the temporal hypercube are referred to the same axis of delays $\tau(x)$: the zero delay is not shifted but it is uniform on all the image pixels. This solves the problem of the hyperbolic phase pattern across the FOV but it reduces the fringes visibility as the integral of interferograms on each point of the detector contains interferograms of rays with different angles α with respect to the TWINS.

Chapter 2

Management and development of data

2.1 Analysis and treatment of the temporal hypercube

In section 1.5 we have seen the concept of **temporal hypercube** which is the datum collected by an FT hyperspectral imaging system. This datum is the collection of varius images at different delays determined by the translation of the wedge of the TWINS interferometer. For this reason we can see the temporal hypercube as an image whose pixels contain each one a interferogram as it is presented in Figure 2.1.

As in a measurement acquisition the wedge translator covers the overall excursion through discreet steps (set of translations $\{x\}_{set}$), the collected frames are referred to a discreet set of delay values. For this reason the interferogram in the single pixel of the temporal hypercube is an array of values as a function of τ. As we have seen in section 1.2, the interferogram is the starting datum in FT spectroscopy: by taking the Fourier transform of the interferogram $U(\tau)$ according to equation 1.4 we obtain the frequency spectrum $S(f)$:

$$S(f) = \int_{-\infty}^{+\infty} U(\tau) e^{-i2\pi\tau f}\, d\tau = \mathcal{FT}\left[U(\tau)\right] \tag{2.1}$$

where $\mathcal{FT}$ denotes the Fourier transform operation. As the delay τ depends on the discrete set of wedge translation $\{x\}_{set}$, the FT we have to consider is discrete:

$$S(f) = \sum_{\tau \in \{\tau\}_{set}} U(\tau) \cdot e^{-i2\pi\tau f} \cdot \Delta\tau = \mathcal{DFT}\left[U(\tau)\right] \tag{2.2}$$

where $\Delta\tau$ denotes the difference between τ and its following in the array $\{\tau\}_{set}$ and $\mathcal{DFT}$ denotes the discrete Fourier transform operation.

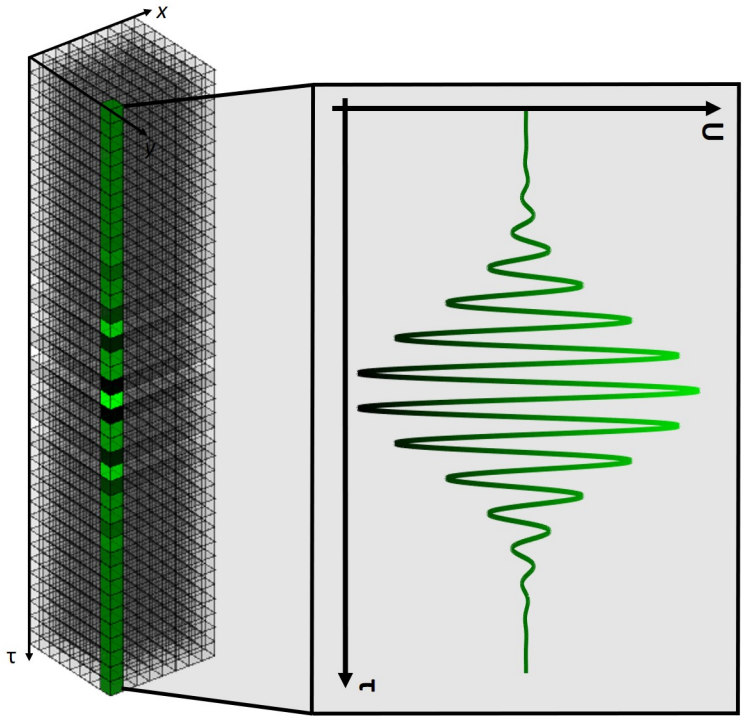

Figure 2.1: Depiction of the temporal hypercube space as three-dimensional matrix: the x and y dimensions identify the pixels in the image plane, the τ dimensions identifies the delays. The window on the right shows the interferogram contained in the pixel in green as energy U vs. delay τ. The color saturation represents the interferogram value.

Therefore, as it is stated by equation 2.2, it is necessary to take the $\mathcal{DFT}$ of each pixel in the image in order to obtain the final spectral hypercube which is the datum of interest in hyperspectral imaging. This is not a straightforward operation because a real measurement acquires a non-ideal interferogram and therefore some treatments are necessary before taking the $\mathcal{DFT}$: the subtraction of the mean (and of a polynomial fit of the slowly varying signal) and the apodization. Moreover we have to point out that in an experimental setup the control is on the wedge translation therefore the retrieved temporal hypercube is referred to the wedge position. This means that the spectra obtain from the FT operation are expressed in terms of pseudo-frequency: the way to pass from the pseudofrequency domain to the frequency domain will be discussed in chapter 3.

2.1.1 Subtraction of the mean and polynomial fit

As we have seen in section 1.2, the physical quantity measured by a detector is the energy; therefore the acquired interferogram is in the form:

$$U(\tau) = C_0 + 2 \cdot C(\tau) \tag{2.3}$$

as it is stated by equation 1.9. In this equation we can see that the acquired interferogram is constituted by a τ-dependent part $2 \cdot C(\tau)$ (which is the term that oscillates) and a constant term C_0 (which simply adds a background to the oscillating part). As $2 \cdot C(\tau)$ oscillates around 0 and it has null mean, the term C_0 represents the mean of the function $U(\tau)$. Therefore, before applying equation 2.2, it is necessary to subtract its mean in order to avoid a peak at frequency $f = 0$ in the spectrum. In experimentally measured interferograms C_0 is not always constant: therefore we have not only the problem to subtract a mean but also to subtract a polynomial function from the interferogram that, after the $\mathcal{DFT}$ operation, would produce artifacts in the spectrum at low frequencies.

2.1.2 Finite acquisition record: convolution with a boxcar

The set $\{\tau\}_{set}$ determined by the wedge excursion during the measurement acquisition is a finite interval. This means that the interferograms contained in the temporal hypercube are not extended from $-\infty$ to $+\infty$ as the theory of equation 2.1 requires. Therefore a real aquired interferogram can be seen as an infinite extended interferogram $U(\tau)$ multiplied by a 'boxcar' function $BX(\tau)$ [19]; applying equation 2.1 we have:

$$\int_{-\infty}^{+\infty} U(\tau) \cdot BX(\tau) \cdot e^{-i2\pi\tau f}\, d\tau = \mathcal{FT}\left[U(\tau) \cdot BX(\tau)\right] \tag{2.4}$$

whith the boxcar function defined as:

$$BX(\tau) = \begin{cases} 1 & \text{if } \; T_1 \leq \tau \leq T_2 \\ 0 & \text{if } \; \tau < T_1 \;\; \text{or} \;\; \tau > T_2 \end{cases} \tag{2.5}$$

where T_1 and T_2 indicate respectively the first and the last delay in the excursion set $\{\tau\}_{set}$. From the FT theory [11] the operation 2.4 can be rewritten as:

$$\mathcal{FT}\left[U(\tau) \cdot BX(\tau)\right] = \mathcal{FT}\left[U(\tau)\right] * \mathcal{FT}\left[BX(\tau)\right] = S(f) * \mathcal{FT}\left[BX(\tau)\right] \tag{2.6}$$

where we use $*$ to denote the convolution operation. As we have that:

$$\mathcal{FT}\left[BX(\tau)\right] = \int_{T_1}^{T_2} e^{-i2\pi\tau f}\, d\tau = \frac{i}{2\pi f}\left[e^{-i2\pi T_2 f} - e^{-i2\pi T_1 f}\right] \tag{2.7}$$

equation 2.6 tells that, the FT of an interferogram acquired from delay T_1 to delay T_2, provides $S(f)$ convoluted with a function $\mathcal{FT}\left[BX(\tau)\right]$ which introduces some sidebands artifacts in the spectrum. If we consider a symmetric acquisition of the interferogram ($T_1 = -T$ and $T_2 = T$) we get from equation 2.7:

$$\mathcal{FT}\left[BX(\tau)\right] = \frac{2T \sin\left(2\pi T f\right)}{2\pi T f} = 2 \cdot T \cdot \operatorname{sinc}\left(2Tf\right) \tag{2.8}$$

Figure 2.2 shows the effect of the multiplication of the interferogram by BX which introduces undesired sidebands in the spectrum near the narrow peak.

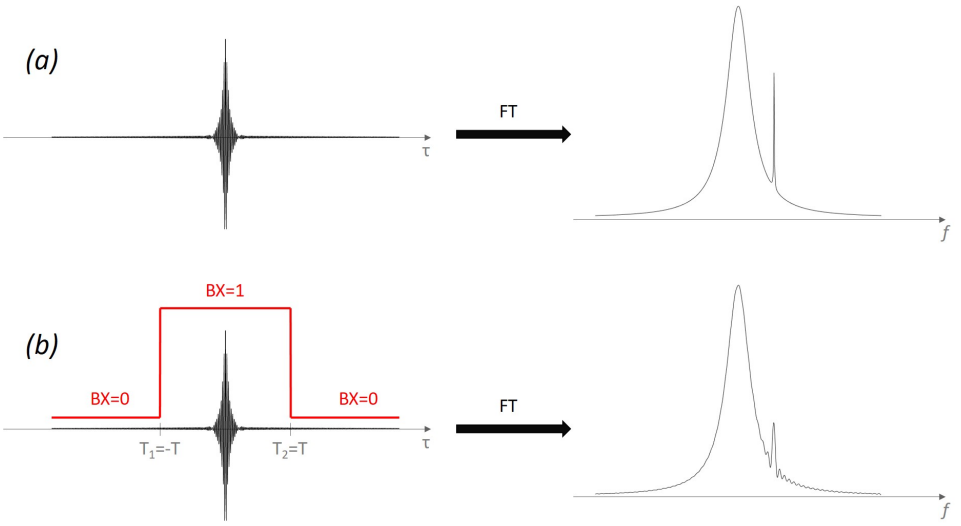

Figure 2.2: Effect of the multiplication of the interferogram by a boxcar function. (a) shows the FT of the infinite extended interferogram which is the real spectrum on the right. (b) shows the FT of the same interferogram multiplied by a boxcar BX with extension from $T_1 = -T$ to $T_2 = T$.

Figure 2.2 (b) presents the case in which the boxcar is symmetric with respect to the delay $\tau = 0$ and the FT ends up with a spectrum which is a real function. If we consider an asymmetric boxcar (with T_1 and T_2 which are not necessarily $T_1 = -T$ to $T_2 = T$) we have the convolution of the spectrum $S(f)$ with the complex function described by equation 2.7: in this case the resulting spectrum is not a real function but it is complex. The problem of treating complex spectra will be discussed in section 2.3.

In Figure 2.2 it is evident that the convolution with $\mathcal{FT}\left[BX(\tau)\right]$ produces a broadening of the spectrum peaks: this broadening inversely depends on the width of the boxcar window. This is a fundamental property of the FT spectroscopy: the spectral resolution depends on the delay interval scanned during the acquisition.

2.1.3 Apodization

As in real measurements we acquire a finite record of the interferogram, we can't avoid the sidebands effect on the spectrum; however we can reduce it using the so called **apodization**.

The concept behind apodization is to truncate the interferogram less abruptly than with 'boxcar' cutoff: therefore we multiply the interferogram by a proper apodization function. There are several apodization functions

described in literature (see for example [19], [21] and [22]): Figure 2.3 shows some of the most used apodization windows and shows their effect on a single-line spectrum.

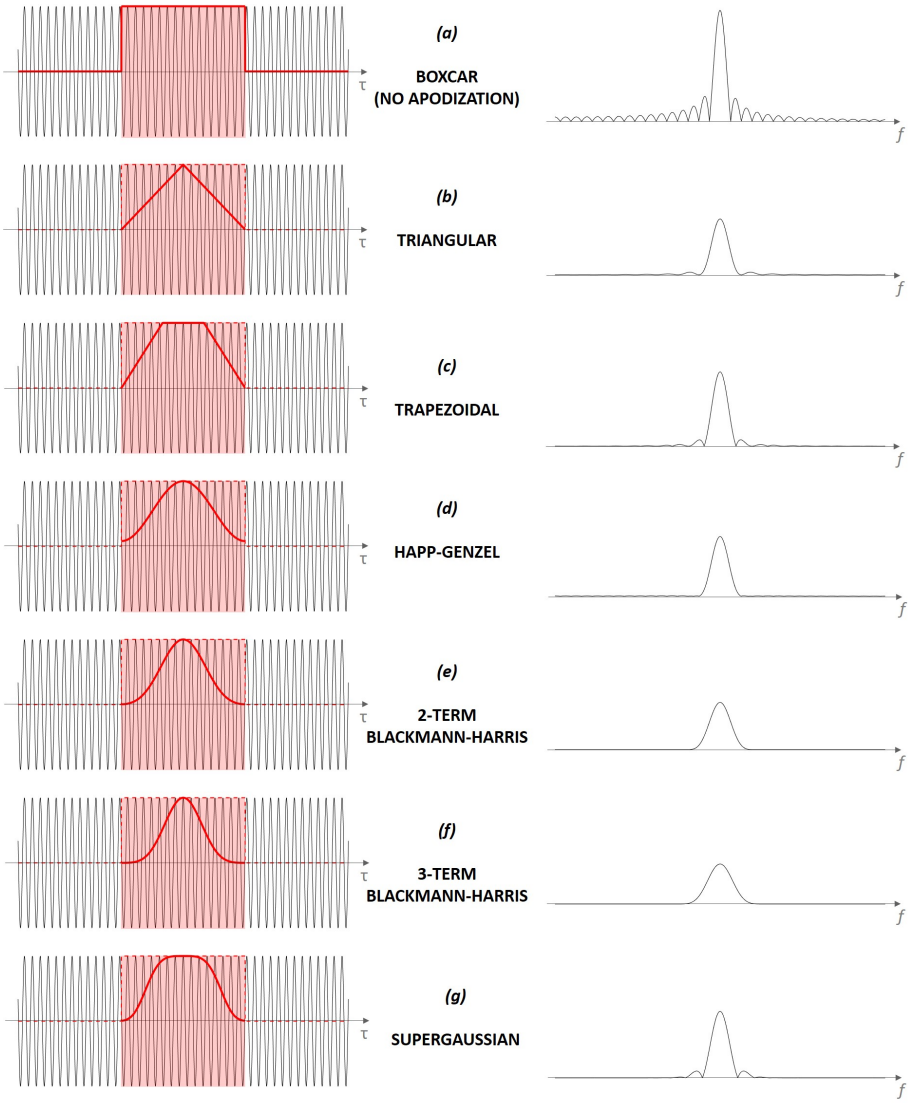

Figure 2.3: Effect of different apodizations on a cosinusoidal interferogram function (simulated in MATLAB). Left: the sinusoidal interferogram (black line) and the apodization function (red line). The apodizations have been built considering the delay window defined by the boxcar (dashed red line): this simulates the finite record of the interferogram in a real measurement (red shaded area). The Supergaussian has been considered in the form $e^{-\tau^{2\cdot \mathrm{index}}}$ with index = 2. Right: the resulting spectrum after the FT operation.

The different apodizations have their pros and cons and the best one depends on the particular measurement and the particular spectrum we are acquiring. The two most important characteristics to consider for the

choice of the apodization are the sidebands added to the spectrum lines and the broadening of the lines. Figure 2.4 shows the cases (d), (f) and (g) (presented in Figure 2.3) in a semi-logarithmic plot. As it can be clearly seen the Supergaussian apodization determines the smallest broadening of the spectrum line but it presents evident sidelobes next to the peak. 3-term Blackmann-Harris apodization function has negligible sidelobes but it determines a considerable broadening of the peak. Happ-Genzel apodization is a good compromise between the sidebands (10^{-2} smaller than the main peak) and the broadening. As it can be seen Supergaussian and Happ-Genzel present an higher peak in the spectrum with respect to the 3-term Blackmann-Harris.

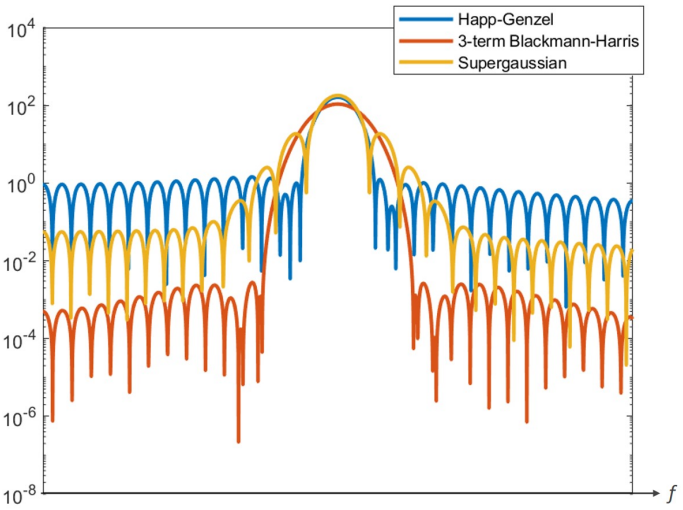

Figure 2.4: Comparison between Happ-Genzel, 3-term Blackmann-Harris and Supergaussian apodization functions effects ((d), (f) and (g) cases in Figure 2.3). The y-axis is in logarithmic scale in order to enhance the level of the ripples. The Supergaussian has been considered in the form $e^{-\tau^{2\cdot \mathrm{index}}}$ with index $= 2$.

From this analysis it is clear that the best apodization depends on which kind of property we need for our specific case. For example in a measurement in which the level of noise is very high the best apodization is the Happ-Genzel because it does not lower and broaden conspicously the spectrum peaks and the high-level ripples are anyway covered by the noise. Instead in a measurement with low noise and broadband-features spectum the best apodization between (d), (f) and (g) cases will be the 3-term Blackmann-Harris.

2.2 Implementation of the Fourier Transform

As it has been already anticipated in section 2.1, in FT hyperspectral imaging we obtain the spectral hypercube taking the Descreete Fourier Transform, $\mathcal{DFT}$, of each interferogram contained in the temporal hypercube. Therefore, if we consider the interferogram $U_p(\tau)$ (already adjusted with the subtraction of the mean and the polynomial fit and already apodized) of the pixel p, we calculate the spectrum $S_p(f)$ on that pixel through the operation:

$$S_p(f) = \mathcal{DFT}\left[U_p(\tau)\right] \tag{2.9}$$

The operation stated in 2.9 has to be performed for each pixel p of the image and this can results in a very time-demanding process for images larger than 1 Mpixel. For this reason the implementation choice for the operation $\mathcal{DFT}$ is very important from a computational point of view.

One of the most efficient algorithms for the implementation of the $\mathcal{DFT}$ is the Fast Fourier Transform (FFT). In [23] it has been shown that the $\mathcal{DFT}$, which was thought to require N^2 arithmetic operations, could have a computational cost of $N\log(N)$ operations if it is implemented in the FFT algorithm.

In experimental interferograms the set of wedge translations $\{x\}_{set}$ is not uniform because the positions assumed by the wedge are not perfectly equispaced: therefore in reality what we have to perform is the Non-uniform Discrete Fourier Transform, $\mathcal{NDFT}$, and for each pixel p we have to calculate:

$$S_p(f) = \mathcal{NDFT}\left[U_p(\tau)\right] \tag{2.10}$$

As the FFT algorithm works only for equispaced data we can't use it to implement the $\mathcal{NDFT}$.
If we consider equation 2.2 for a non-uniform delays set $\{\tau\}_{set}$ we can write:

$$\mathcal{NDFT}\left[U_p(\tau)\right] = \sum_{\tau\in\{\tau\}_{set}} U(\tau)\cdot e^{-i2\pi\tau f}\cdot\Delta\tau \tag{2.11}$$

We can write the delays set as:

$$\{\tau\}_{set} \doteq \begin{pmatrix}\tau_1\\ \tau_2\\ \vdots\\ \tau_n\end{pmatrix} \tag{2.12}$$

and its differential as:

$$\{\Delta\tau\}_{set} \doteq \begin{pmatrix}\Delta\tau_1 = \tau_2 - \tau_1\\ \Delta\tau_2 = \tau_3 - \tau_2\\ \vdots\\ \Delta\tau_{n-1} = \tau_n - \tau_{n-1}\\ \Delta\tau_n = \tau_n - \tau_{n-1}\end{pmatrix} \tag{2.13}$$

If we consider these definitions[1] and the frequency set $\{f\}_{set}$, we want to take the points of the spectrum S_p in, defined as:

$$\{f\}_{set} \doteq \begin{pmatrix} f_1 \\ f_2 \\ \vdots \\ f_m \end{pmatrix} \tag{2.14}$$

we can rewrite equation 2.11 exploiting the matrix product:

$$\begin{aligned} &\begin{pmatrix} S_p(f_1) \\ S_p(f_2) \\ \vdots \\ S_p(f_m) \end{pmatrix}^T = \mathcal{NDFT}\left[U_p(\tau)\right] = \\ &= \begin{pmatrix} U_p(\tau_1)\cdot\Delta\tau_1 \\ U_p(\tau_2)\cdot\Delta\tau_2 \\ \vdots \\ U_p(\tau_n)\cdot\Delta\tau_n \end{pmatrix}^T \cdot \begin{pmatrix} e^{-i2\pi\tau_1 f_1} & e^{-i2\pi\tau_1 f_2} & \dots & e^{-i2\pi\tau_1 f_m} \\ e^{-i2\pi\tau_2 f_1} & e^{-i2\pi\tau_2 f_2} & \dots & e^{-i2\pi\tau_2 f_m} \\ \vdots & \vdots & \ddots & \vdots \\ e^{-i2\pi\tau_n f_1} & e^{-i2\pi\tau_n f_2} & \dots & e^{-i2\pi\tau_n f_m} \end{pmatrix} \end{aligned} \tag{2.15}$$

where ^{T} is the symbol for transposed and $\cdot$ between the vector and the matrix denotes the matrix product. As it can be seen in equation 2.15 the only elements which depend on the particular pixel p are $U_p(\tau_1)$, $U_p(\tau_1)$, ... , $U_p(\tau_n)$ that are the interferogram vector elements for the pixel p. If we assume a unique delays set $\{\tau\}_{set}$ for an acquisition of the temporal hypercube, we can calculate $\{\Delta\tau\}_{set}$ (as defined by equation 2.13) and the matrix of exponentials (in 2.15) only one time: it is not necessary to calculate them for each pixel p of the image.

The matrix implementation of the $\mathcal{NDFT}$ described by equation 2.15 with the precalculation of the differentials $\{\Delta\tau\}_{set}$ and the exponentials matrix is an operation that can be easily setted up and performed in a MATLAB software in a reasonable amount of time even for a very large number of pixels.

There is another possibility to implement an efficient algorithm for $\mathcal{NDFT}$ which is the Non-uniform Fast Fourier Transform (NUFFT) algorithm: the mathematical discussion of this algorithm can be found in [24].

Figure 2.5 shows the results of a simulation in which the performances of the matrix implementation of $\mathcal{NDFT}$ as described by 2.15 has been compared to the performances of the NUFFT algorithm. The calculations have been performed on a simulated interferogram with a certain number of samples (number n of delays in the vector $\{\tau\}_{set}$) and repeated for 10^5 iterations

[1]Note that the last two elements of vector $\{\Delta\tau\}_{set}$ are equal ($\Delta\tau_n = \Delta\tau_{n-1}$): this is an approximation in order to have $\{\tau\}_{set}$ and $\{\Delta\tau\}_{set}$ of the same dimension.

(the iterations simulate the large amount of pixels of an image). The number of samples for the simulated interferogram has been: 256, 512 and 1024. The number of elements for the calculated spectrum (number m of frequencies in the vector $\{f\}_{set}$) was fixed to 500. For the matrix implementation of $\mathcal{NDFT}$ have been taken into considerations both the case in which the differetial delay set $\{\Delta\tau\}_{set}$ and the exponentials matrix are calculated each time for each iteration and the case in which they are precalculated only one time before starting the iterations.

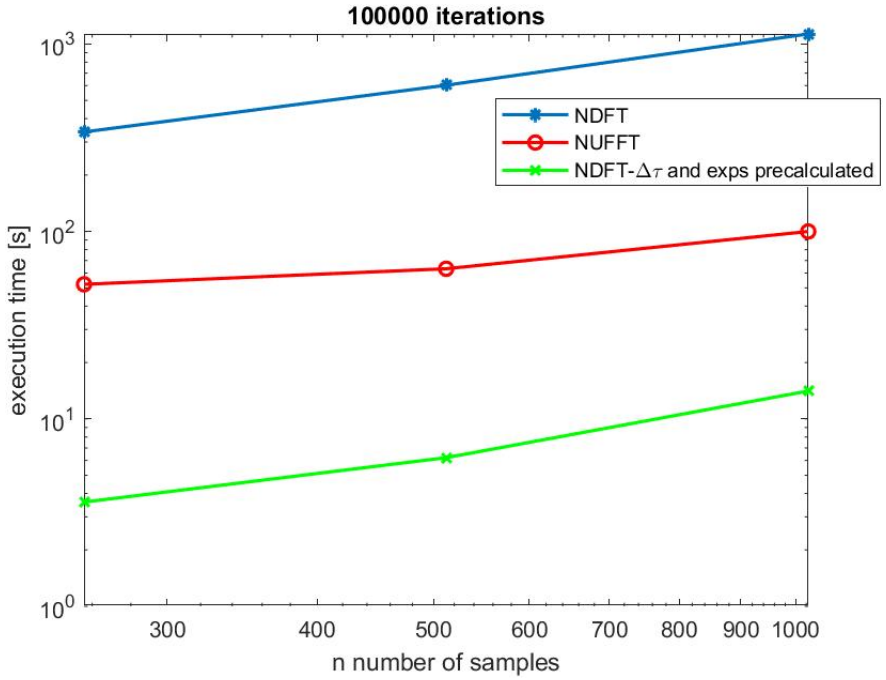

Figure 2.5: Results of a MATLAB simulation of three different implementations of the Non-uniform Discrete Fourier Transform (NDFT). This graph in logarithmic scale shows the total execution time as a function of the number of samples (number n of elements in the delay set $\{\tau\}_{set}$: $n = 256$, $n = 512$ and $n = 1024$) for a fixed number of iterations (10^5 iterations). The number of elements for the calculated spectrum (number m of frequencies in the vector $\{f\}_{set}$) was fixed to $m = 500$. **NDFT**: Non-uniform Discrete Fourier Transform as described by equation 2.15 with the calculation of $\{\Delta\tau\}_{set}$ and the matrix of exponentials for each iteration. **NUFFT**: Non-uniform Fast Fourier Transform algorithm implemented by the MATLAB function $nufft$. **NDFT-$\Delta\tau$ and exps precalculated**: Non-uniform Discrete Fourier Transform as described by equation 2.15 with the calculation of $\{\Delta\tau\}_{set}$ only one time before the iterations.

As it can be seen from this figure, the best implementation in terms of execution time is the one in equation 2.15 with the precalculation of $\{\Delta\tau\}_{set}$ and the exponentials matrix. Therefore from now on when referring to the FT of a real acquired temporal hypercube we will mean the operation stated in 2.15 with the precalculated elements repeated for each pixel in the image (for each interferogram U_p of each pixel p).

2.3 Analysis and treatment of the spectral hypercube

As we have seen in section 2.2 we obtain the spectral hypercube taking the FT of the temporal hypercube which means applying equation 2.15 to all the interferograms U_p of the various pixels in the image in order to obtain the corresponding spectra S_p. In this section we will concern the problems related to the treatment of a spectral hypercube that derived from a measured temporal hypercube and we will presents and discuss the possible methods to extract a physical and significant information from it.

In the ideal case the temporal hypercube contains interferograms which are symmetric with respect to the zero delay and, taking the FT of this, we would obtain a spectral hypercube constituted by real numbers. As we have seen in section 1.5 the various interfrograms collected across the FOV in an hyperspectral FT imaging system based on TWINS are intrinsically referred to slightly different delay axis because there's a certain shift τ_{shift} in the delay (see equation 1.26) due to the angle α the incoming rays forms with the optical axis of the TWINS interfometer. In addition, there may be a certain imprecision in the real evaluation of the wedge positions $\{x\}_{set}$ during the measurement (due to both the motor positioning errors and the control software which have an intrinsic uncertainty, $\sim 0.1\mu m$) and therefore the delay axis $\{\tau\}_{set}$ is not exactly the expected one from the sampled points of the interferogram vector. As discussed in [19], the FT of an asymmetric interferogram determines a complex spectrum: this means that an experimental temporal hypercube ends up in a complex spectral hypercube in which both real and imaginary parts are present. Together with the intrinsic delay shift there is the measurement noise which perturbes the measurement of the temporal hypercube: this determines an intrinsic asymmetry even in the functional form of the interferograms which would be supposed to be exactly symmetric with respect to their own baricenters.

In order to better visualize this problem we give now a general mathematical description of an interferogram and the phenomena which determines its asymmetry with respect to the zero-path delay (ZPD), $\tau = 0$. We start considering an ideal interferogram U_{ideal} which is perfectly symmetric with respect to the ZPD. If we take its FT we obtain the ideal spectrum S_{ideal} which is a purely real function:

$$\mathcal{FT}\left[U_{ideal}(\tau)\right] = S_{ideal}(f) \tag{2.16}$$

If now we introduce a delay shift τ_{shift} (which is defined according to equation 1.25) in the points of the delay axis $\{\tau\}_{set}$ the ideal interferogram is reffered to, we have to consider an interferogram $U_{ideal}(\tau + \tau_{shift})$. According to equation 1.26 we would have that the delay shift τ_{shift} depends on the nominal position x of the wedge and therefore it would be different for

different delays τ: in this discussion we consider this shift as independent on the delay τ and therefore we consider it as a constant. In this approximation we have that all the points of the function U_{ideal} are shifted by a constant quantity τ_{shift}. If we take the FT we obtain:

$$\mathcal{FT}\left[U_{ideal}(\tau + \tau_{shift})\right] = e^{i2\pi\tau_{shift}f} \cdot S_{ideal}(f) \tag{2.17}$$

therefore from FT properties we obtain a complex spectum with modulus equal to S_{ideal} and phase equal to $2\pi\tau_{shift}f$. Equation 2.17 tells us that, if the problem on the interferogram were simply a delay shift, we would just need to correct the phase by multiplying the result of the FT by $e^{-i2\pi\tau_{shift}f}$ (or by taking its absolute value). But, as we have already marked, an experimentally acquired interferogram is disturbed by noise. Therefore a complete description of the interferogram is:

$$U(\tau) = U_{ideal}(\tau + \tau_{shift}) + n(\tau) \tag{2.18}$$

where the function n is the uncorrelated noise and, in principle, it can include also the correction to τ_{shift} which depends on τ. If we take the FT of U we obtain:

$$\begin{aligned} &\mathcal{FT}\left[U(\tau)\right] = \mathcal{FT}\left[U_{ideal}(\tau + \tau_{shift}) + n(\tau)\right] = \\ &= e^{i2\pi\tau_{shift}f} \cdot S_{ideal}(f) + \mathcal{FT}\left[n(\tau)\right] \end{aligned} \tag{2.19}$$

The FT of the noise is a complex function with a phase $\phi_n(f)$ which randomly depends on f therefore we can write:

$$\mathcal{FT}\left[U(\tau)\right] = e^{i2\pi\tau_{shift}f} \cdot S_{ideal}(f) + e^{i\phi_n(f)} \cdot N(f) \tag{2.20}$$

where $N(f)$ is the modulus of the FT of the noise. Equation 2.20 clearly shows that we can't retrieve a real function spectrum with a simple phase correction multiplying by $e^{-i2\pi\tau_{shift}f}$. If we fix to a particular frequency $\bar{f}$, from this equation we can understand that:

$$\mathcal{FT}\left[U(\tau)\right](\bar{f}) \sim \begin{cases} e^{i2\pi\tau_{shift}\bar{f}} \cdot S_{ideal}(\bar{f}) & \text{if } S_{ideal}(\bar{f}) \gg N(\bar{f}) \\ e^{i\phi_n(\bar{f})} \cdot N(\bar{f}) & \text{if } S_{ideal}(\bar{f}) \ll N(\bar{f}) \end{cases} \tag{2.21}$$

Therefore, if we consider a frequency $\bar{f}$ which corresponds to a peak of the physical spectrum S_{ideal} that is above the modulus of the FT of the noise ($S_{ideal}(\bar{f}) \gg N(\bar{f})$), the phase of the complex spectrum $\mathcal{FT}\left[U(\tau)\right]$ is $\sim 2\pi\tau_{shift}\bar{f}$, if we consider a frequency $\bar{f}$ which corresponds to a frequency region in which there's no signal ($S_{ideal}(\bar{f}) \ll N(\bar{f})$), the phase is $\phi_n(\bar{f})$. If we take into consideration a population of pixels of an hyperspectral image all referred to a spatial region in which it is supposed to have a single type of spectrum S_{ideal}: in the first case ($S_{ideal}(\bar{f}) \gg N(\bar{f})$) we have that all the pixels contain a complex value with an almost constant phase $\sim 2\pi\tau_{shift}\bar{f}$

(spatially correlated phase), in the second case ($S_{ideal}(\bar{f}) \ll N(\bar{f})$) all the pixels have random different phases $\phi_n(\bar{f})$ which depend on the particular pixel (spatially uncorrelated phase). Figure 2.6 (c) shows the plot in the Gauss plane (real part and imaginary part) of a population of 64×64 pixels in a simulated hyperspectral image: all these pixels contain different complex spectra due to added noise but, in principle, all derive from the same physical spectrum (Figure 2.6 (a)). As it can be seen, the pixels population at a frequency coincident with a peak of the physical spectrum are distributed in a region of the plane such that their complex phase is limited around a certain value which coincides with $2\pi\tau_{shift}\bar{f}$ (correlated phase). The pixels population belonging to a frequency where there's no signal are distributed around the origin of the Gauss plane and therefore their phases span all the round corner.

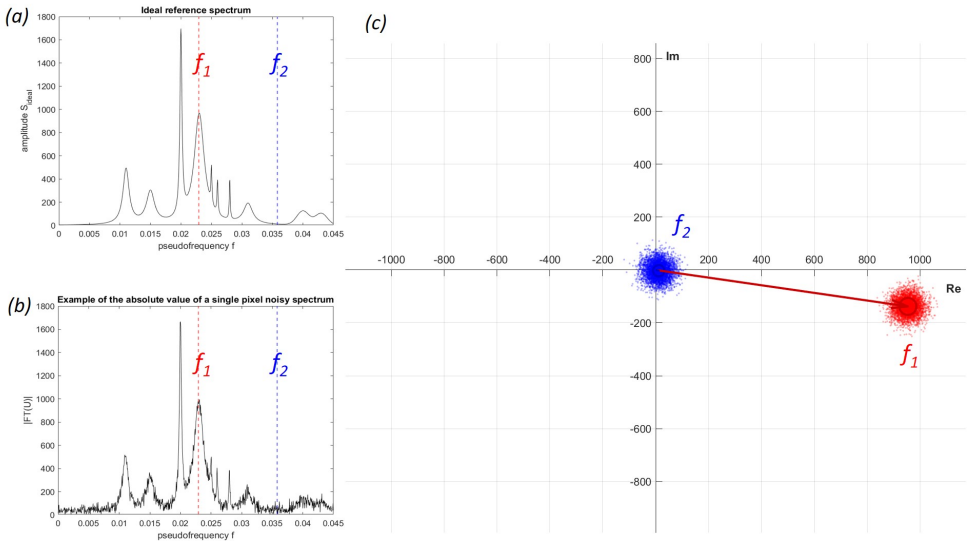

Figure 2.6: Results obtained from a MATLAB simulation considering a noisy complex spectral hypercube with 64×64 pixels, each of them containing a noisy complex spectrum generated from the reference noiseless real spectrum depicted in (a). Starting from the ideal spectrum (a), we generated the corresponding interferogram for each pixel. Then all the 4096 independent interferograms have been temporally shifted and Gaussian noise with standard deviation equal to 1/100 of the maximum of the interferogram has been added independently to each one of the interferograms. The noisy interferograms has been apodized with Happ-Genzel window and then Fourier transformed to obtain the final noisy complex spectral hypercube. (b): an example of the absolute value plot of a single spectrum in the noisy complex hypercube. (c): plot in the Gauss plane of the 64×64 pixels of the image at the frequencies indicated by the vertical dashed lines in (a) and (b). The arrows indicate the mean value of the complex numbers at a fixed frequency, the circle indicates the standard deviation calculated as the square root of the variance of the absolutes values.

This different behaviour of the complex phase of the spectra in the case of signal peak frequencies and in the case of completely noisy frequencies is a useful information that, even if it is not directly a physical observable, can be exploited for the spectral hypercube analysis together with the absolute

value of the spectra.

As for hyperspectral imaging analysis the final datum we want to study is a spectrum (or a set of spectra) constituted by real numbers and therefore an actual physical observable, finally we need to extract a real quantity from the complex FT we obtain. There are two ways to extract this physical information which are:

1. taking the real part of FT
2. taking the absolute value of FT

The first case needs some care because the real part of complex numbers can be negative if the complex phase is contained in the interval $\left[\frac{\pi}{2} + 2k\pi, \frac{3\pi}{2} + 2k\pi\right]$, with $k \in \mathbb{Z}$, and negative values are not physical in an observed spectrum. To face this problem what it has to be done is to correct the complex spectrum by a linear phase which is calculated as linear fit of the phases evaluated at the different frequencies. Starting from equation 2.20 we can write the complex spectrum S_{compl} as:

$$S_{compl}(f) = e^{i2\pi\tau_{shift}f} \cdot S_{ideal}(f) + e^{i\phi_n(f)} \cdot N(f) = |S_{compl}(f)| \cdot e^{i\hat{\phi}(f)} \quad (2.22)$$

where $\hat{\phi}$ is the complex phase of S_{compl}. The linear phase correction has to be calculated as linear fit $\hat{\phi}_{fit}(f)$ on the base of the values of $\hat{\phi}$ at the different frequencies f in order to retrieve a good approximation of the linear phase $2\pi\tau_{shift}f$. Considering the different behaviour of the phase for peak frequencies (correlated) and for noisy frequencies (uncorrelated) we have previously discussed, a reasonable method to calculate the linear fit $\hat{\phi}_{fit}(f)$ is to assign a considerable weight to those phase values related to peak frequencies and small weight to those phase values related to noisy frequencies: therefore a good weight-definition for the linear fit implementation can be based on $|S_{compl}(f)|$ itself. Then the phase correction of the spectrum S_{compl} is simply performed multiplying it by the term $e^{-i\hat{\phi}_{fit}(f)}$. This approach of multiplying by a phase, based on the Mertz-method [2], is supposed to produce a final spectrum which has negligible complex phase for those values in correspondence of peak frequencies and considerable complex phase for those values related to noisy frequencies: in this way the real part of such a spectrum determines only positive peaks and positive and negative noise spikes. This method of analysis is useful when a mean spectrum is calculated from a certain omogeneous region of interest (ROI) in the hyperspectral image because the spectrum peaks sum up and the noise on average simplifies.

The second possibility is to take the absolute value of $S_{compl}(f)$ and

[2]In the Mertz-method the phase is extracted deducing the temporal shift τ_{shift} of the interferogram taking the central lobe as reference [25]. This operation would in principle be equal to taking the absolute value of the spectrum but this is not the case in noisy experimental interferograms

therefore directly consider $|S_{compl}(f)|$ as the measured spectrum. In this case of spectrum evaluation, two possibilities arises when we consider a population of pixels in an hyperspectral image which are all supposed to contain the same physical spectrum and we want to consider the mean spectrum of such a ROI. These two different possibilities are:

- mean of the absolute values of the spectra
- absolute value of the mean of the spectra

These two approaches are not equivalent because in general the absolute value of the sum of complex numbers is not equal to the sum of the absolute values. The difference between the two is straightforward from Figure 2.6 (c). We can understand that taking the mean of the absolute values of a population of complex numbers means to take the mean geometrical distance from the origin of the related points in the Gauss plane; instead taking the absolute value of the mean means to take the modulus of the mean point in the Gauss plane. Between these two approaches the best one is the absolute value of the mean because if we consider Figure 2.6 (c) taking the absolute value of the mean for the population of points related to the peak frequency means to take the length of the red arrow and taking the absolute value of the mean for the population of points related to the noisy frequency means to take the length of the blue arrow which is almost imperceptible because its mudulus is almost zero. In this way, taking the absolute value of the mean, we end up with a mean spectrum in which we have that noise cancel out because its uncorrelated nature ends up in a mean which is almost zero in the Gauss plane and in which the peaks (correlated nature of the signal) are preserved. Figure 2.7 shows the comparison of the two approaches. If the mean spectrum S_{mean} is calculated as the mean of the absolute values of the selected complex spectra S_{compl}, even if we average over a large number of pixels we have that the signal is "overwhelmed" by the noise. Instead if the mean spectrum S_{mean} is calculated as the absolute value of the mean of the selected complex spectra S_{compl}, as the number of selected pixels increases, the noise cancels out and S_{mean} tends to the noiseless ideal spectrum S_{ideal}. This is a very important result because it makes clear that in FT imaging dealing with a complex hypercube means that the information is contained both in the amplitude and in the phase of the spectra even if this second one is not directly a physical observable. This property allows us to understand the best method to apply when we want to extract a physical spectrum from a generated spectral hypercube datum applying the absolute value operation: **during the analysis we have to preserve as much as possible the complex nature of the datum and only at the end of our calculations, when we need to deal with a real spectrum, we take the modulus**. This approach is even better than the Mertz-method previously discussed because, when the

signal-to-noise ratio is very low (in equation 2.22 S_{ideal} and N are of the same order of magnitude), the calculation of the correction term $e^{-i\phi_{fit}(f)}$ can be mislead by the noise itself (the contribution of the uncorrelated phase ϕ_n to the overall phase $\hat{\phi}$ is not negligible even for peak frequencies) and this can determine consistent negative overshoots in the spectrum where we expect signal peaks.

The analytical method of dealing with a complex datum and extracting the absolute value only at the end works only if all the pixels in the hyperspectral image are characterized by the same delay shift τ_{shift} of the related interferograms: if this is not, it is not anymore true that the pixel population at a peak frequency $\bar{f}$ plotted in the Gauss plane has small phase variations around a fixed value $2\pi\tau_{shift}\bar{f}$. In an hyperspectral FT imaging system based on TWINS the condition of constant τ_{shift} is only guaranteed in the uniform ZPD configuration where all the interferograms in the acquired temporal hypercube are referred to the same delay axis (see section 1.5). In all the other configurations where this property is not guaranteed we have to use the Mertz-method or to directly consider the absolute value of the spectral hypercube.

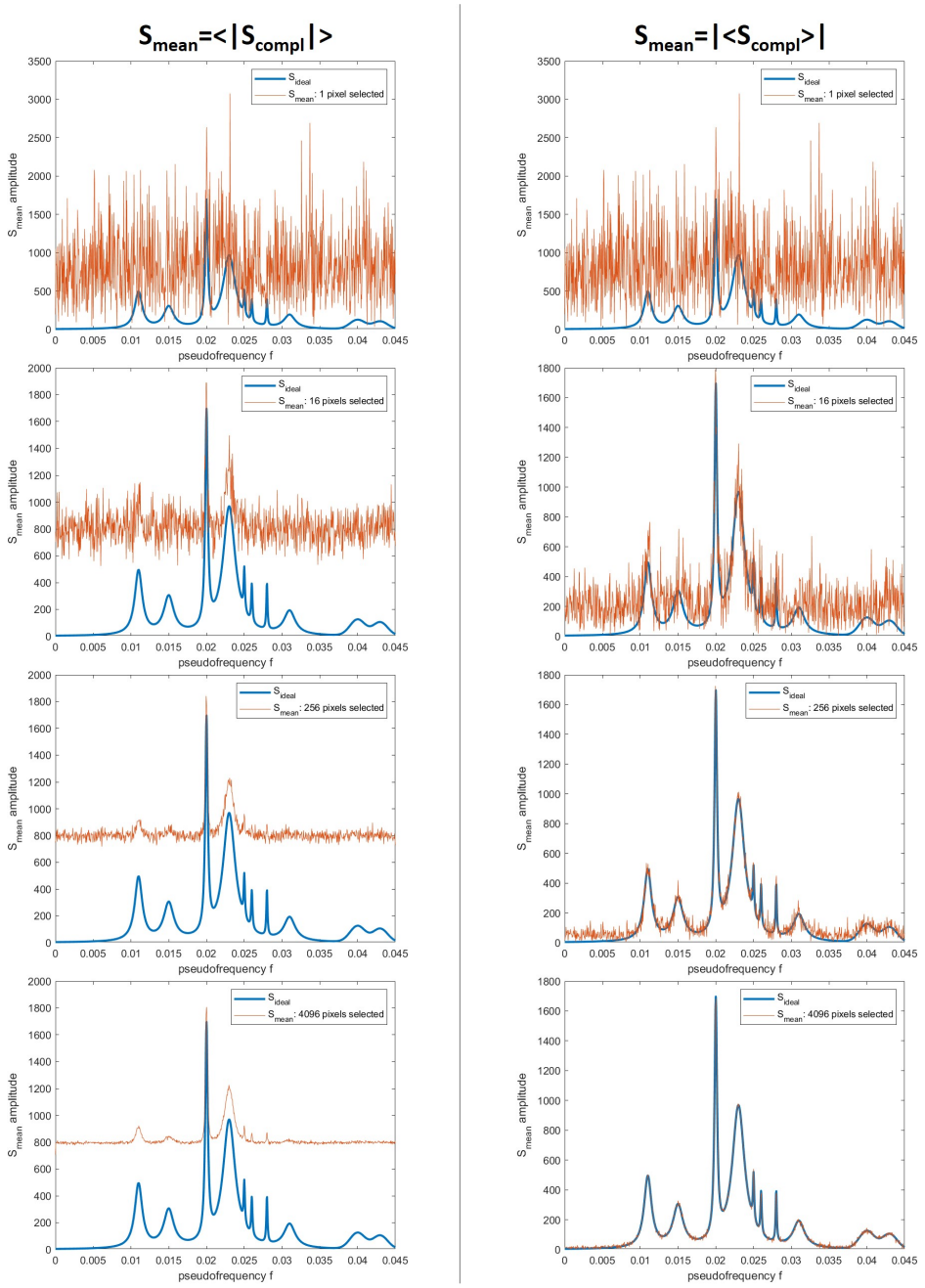

Figure 2.7: Results obtained from the same simulation described in Figure 2.6 but considering a noise standard deviation equal to 1/5 of the maximum of the ideal interferogram. The left column (title $S_{mean} = \langle |S_{compl}| \rangle$) shows the mean spectrum $S_{mean} = \langle |S_{compl}| \rangle$ in the noisy complex spectral hypercube. The right column (title $S_{mean} = |\langle S_{compl} \rangle|$) shows the mean spectrum $S_{mean} = |\langle S_{compl} \rangle|$. On each column there are four rows each one containing the comparison of S_{mean} (red line) with the starting ideal spectrum S_{ideal} (bold blue line) for different numbers of selected pixels: 1, 16, 256 and 4096.

Chapter 3

FT Hyperspectral Microscope based on TWINS

In section 1.5 we have seen the general scheme of an imaging system which implements hyperspectral widefield imaging based on FT with TWINS interferometer and the possible configurations for a 4f system in microscopy (high-fringes visibility and uniform ZPD). Now we give the description of the scheme and the functionality of the Hyperspectral Microscope (HSM) used for the acquisition of the measurements presented in this thesis work.

3.1 Scheme: hardware and software components and illumination and detection geometry

As presented in [1] a Leica DMRBE optical microscope has been upgraded to HSM placing the TWINS interferometer described in section 1.3 between the tube lens and the 2-dimensional position sensitive detector (Luca R, Andor, Belfast, Northern Ireland) with size $8 \times 8mm^2$, 1002×1004 pixels, 14-bit depth, and spectral sensitivity from 400 nm to 1100 nm. In this way the HSM has been realized in the uniform ZPD configuration (see subsection 1.5.1 for the description of this configuration) that guarantees a uniform delay on the FOV. The TWINS interferometer described in section 1.3 has been realized with crossed polarizers' axes (as shown in Figure 1.6): this means that at the delay $\tau = 0$ we have destructive interference of the light after the TWINS and no light comes to the detector. The birefringent blocks A and B are in α-barium borate (α-BBO) [1] and the B block is cut into two wedges with apex angle $\alpha_{apex} = 7°$. The wedge translation is performed through a motorized step system (translator $PI^{®}$ L-402 Miniature Linear Stage) which is driven by a motor controller ($PI^{®}$ C-663.12 Mercury Step

[1] The α-BBO is a negative uniaxial crystal with ordinary refractive index $n_{\|} = 1.6725$ and extraordinary refractive index $n_{\perp} = 1.5322$ considering $600nm$ wavelength.

Stepper Motor Controller). The motor controller is connected to a PC in order to receive instructions for the translations of the step system. By means of a LabVIEW software, the PC transmits to the motor controller the target translator position, as decided by the user. To check if the step system has been correctly translated, the PC receives from the motor controller the value of the effective position the translator is in. The check on the position value is done in the LabVIEW software with a tolerance of $0.1\mu m$ [2]. The same LabVIEW software is used to control the detector parameters that will be presented in section 3.2. Figure 3.1 shows a schematic representation of the HSM. The commercial microscope has been modified with the addition of a fiber coupling to allow the illumination with a laser from the top of the sample. Figure 3.2 illustrates the scheme of laser illumination from the top; a dedicated optical system has been designed in order to have on the sample plane the image of the exit of the fiber: in this way the sample is illuminated by a spatially uniform laser spot if a multimode fiber is used. In reality to obtain a uniform spot the fiber is bent in order to mix of the multiple modes. In addition, to average out the speckle effect on the sample plane, in our measurements the fiber is shaken by a loudspeaker oscillating at a $45Hz$ frequency modulation.

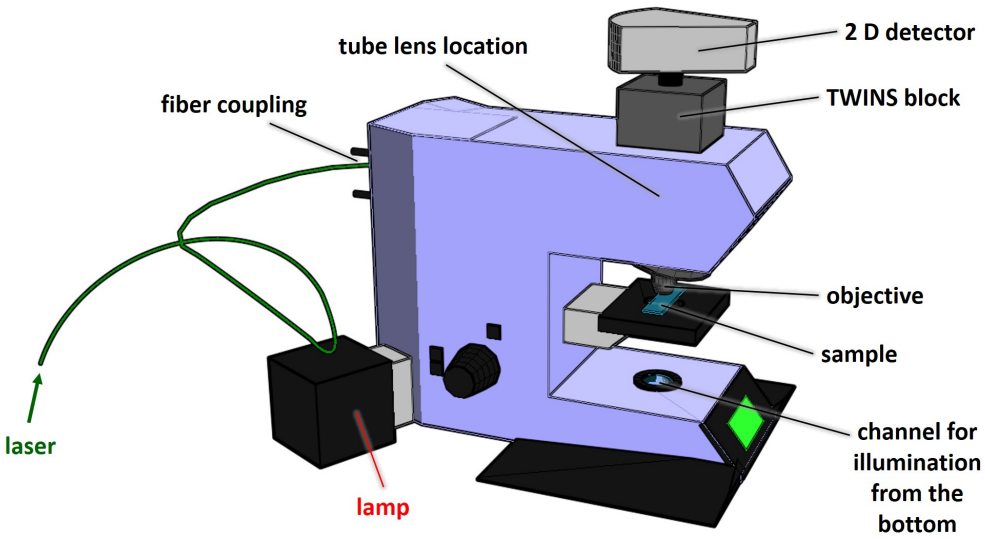

Figure 3.1: Scheme of the Hyperspectral Microscope with TWINS interfrometer located between the tube lens and a 2 dimensional detector. In this scheme there are also two illumination sources: an integrated lamp for the illumination from the bottom (widefield transmission geometry) and laser source through a fiber coupling that allows illumination from the top (widefield reflection geometry, see Figure 3.2 for the details).

[2]This means that the step system translation and the motor controller-PC communications are repeated until the difference of the effective translator position (value received by the PC from the motor controller) with respect to the target is smaller than $0.1\mu m$.

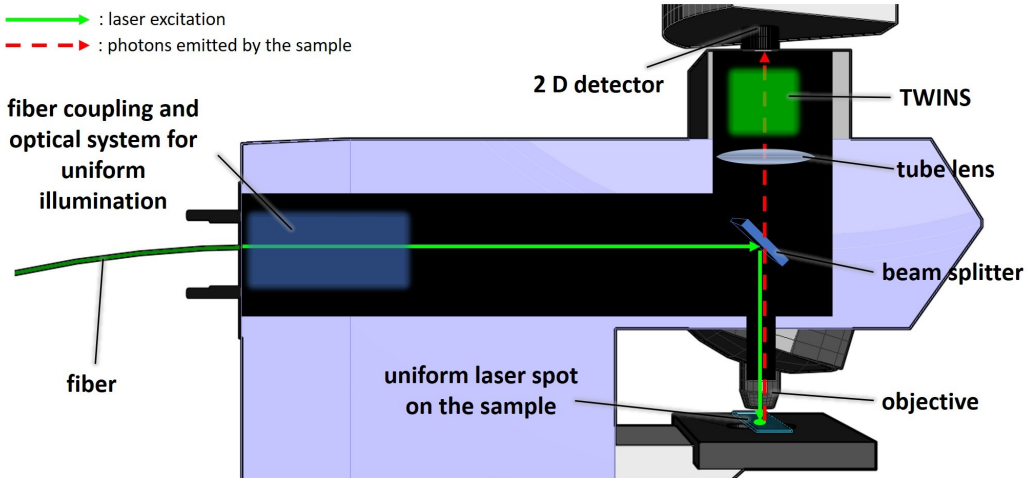

Figure 3.2: Schematic representation of the illumination from the top (widefield reflection geometry) with a laser through a coupled fiber. An optical system (*fiber coupling and optical system for uniform illumination*) has been designed in order to allow a *uniform laser spot on the sample* when the excitation light is focused by the *objective*. A *beam splitter* reflects the laser on the sample and lets the red-shifted photons emitted by the sample pass through the detection uniform ZPD module (*objective*, *tube lens*, *TWINS* and *2 D detector*).

As it can be seen the laser light propagates in the horizontal direction inside the microscope after the fiber coupling and then it is reflected by a beam splitter. The objective focuses the laser in the uniform illumination spot to excite the sample. The photons emitted by the sample can pass through the beam splitter (if they are red-shifted with respect to the laser wavelength) therefore they are collected by the uniform ZPD imaging system which creates on the 2 dimensional detector an image for each delay τ controlled by the wedge translation x in the TWINS. As the illumination light comes from the top, the emitted light from the sample is also collected on the top of it and the illumination area on the sample is large (the image of the fiber section), **this scheme realizes the epi-illumination geometry in widefield imaging** discussed in section 1.4 (see Figure 1.8 (a) as reference). As it is shown in Figure 3.1, there is also the possibility to illuminate the sample from the bottom in **widefield transmission geometry**.

3.2 Measurement acquisition parameters

As we have seen in section 2.1, a measurement with an FT hyperspectral imaging system, such as the HSM, consists in the acquisition of images of the sample at different delays τ scanned by the wedge translation in a discrete set of steps $\{\tau\}_{set}$: this ordered set of frames consititutes the temporal hypercube of the measurement. In this section we discuss all the parameters related to the acquisition of the temporal hypercube.

3.2.1 Detector parameters

With equation 1.3 we have understood that the detector measures an energy and therefore it integrates the incoming light intensity I in an interval $[t_1, t_2]$. In the case of the HSM the 2-dimensional detector is based on the charge-coupled device (CCD) technology and therefore the integrated energy on each detector element is stored as electronic charge accumulated in a potential well [26]. This camera has 14-bit depth: this means $2^{14} = 16884$ discretization levels of the detector dynamics. Therefore the energy values are expressed in counts of the detector that belong to the interval from 0 to 16883. For each acquisition frame we can choose the **integration time** which is the time interval the CCD camera collects the incoming light and consequently promotes electronic charge inside the potential well. Provided that the camera dynamics is not saturated, an high integration time allows to improve the signal-to-noise ratio but it lengthens the measurement time. Another way to improve the S/N ratio is by **binning**: this technique consists on summing up the electrons contained in a certain number of pixels and therefore the resulting frame has lower resolution. If the noise is dominated by the shot noise, the S/N ratio is increased by the square root of the number of binned pixels; if the noise is dominated by the read noise of the CCD, the S/N ratio linearly increases with the number of binned pixels [27]. If, for instance, we set binning equal to 2, this means that we take the average over 2×2 pixels: this reduces the resolution of the image as the number of final separeted pixels is 4 times lower but it increases the signal-to-noise ratio by a factor between 2 and 4. The CCD camera offers also the possibility to increase the electron multiplication inside the potential wells of the pixels through a **gain**: we have seen that this parameter does not appreciably increase the S/N ratio.

3.2.2 Objective

In section 1.5 we have seen the role of the objective in a 4f configuration and the concepts of magnification and resolution of such an optical system. If we have a fixed tube lens as in the case of the HSM depicted in Figure 3.1, the **magnification** of the sample imaged on the detector plane is determined by the objective. As the sample must be located at a distance from the objective equal to its focal length f_1 (see Figure 1.12), also the FOV is uniquely determined by the choice of the objective if the field stop defined by the tube lens is fixed. The resolution of the optical system depends on the objective **numerical aperture** NA as drawn by equation 1.35. Table 3.2 lists the objectives used in HSM measurements presented in chapter 4 and their specifications.

objective	FOV diameter	NA
$Leica^{®}\ PL\ FLUOTAR\ 50\times$	$160\mu m$	0.55
$Leica^{®}\ PL\ FLUOTAR\ 20\times$	$400\mu m$	0.40
$Leica^{®}\ N\ PLAN\ 5\times$	$1600\mu m$	0.12

Table 3.1: Objectives characteristics

3.2.3 Wedge scan

The temporal hypercube acquired in the measurement is defined in the delay τ dimension (see the three-dimensional matrix representation of the temporal hypercube in Figure 2.1) by the position of the wedge translator during the acquisition: for each position a frame is acquired. We call **wedge scan** the set of the translator positions $\{x\}_{set}$ for the particular acquisition. For the HSM measurements the acquisitions are set in uniform wedge scan uniquely defined by the **step width**. As the translation control has a nominal precision of $0.1\mu m$ [3], the wedge scan is not exactly uniform because the steps are not exactly equispaced. The total excursion determines the spectral resolution of the measurement (see subsection 2.1.2): the proper choice of it depends on the spectrum to be measured and on the spectral detail. The wedges used in the HSM has an excursion limited in the interval $[-2810\mu m; +10138\mu m]$ with respect to the ZPD position. The step width is the sampling step Δx of the interferograms therefore from the Nyquist theorem:

$$\Delta x \leq \frac{1}{2 \cdot \nu_{max}} \tag{3.1}$$

where ν_{max} is the maximum frequency of the spectrum [19]. In order to avoid spectrum aliasing, the sampling step has to comply with the theorem 3.1: as there are not lower limits, in principle it can be chosen arbitrarily small. As we have that the lower the sampling step the higher the number of samples for a fixed wedge excursion (that complies with the desired spectral resolution), the best choice would be to take the smallest sampling step as possible because the higher the number of samples the better the S/N ratio. On the other hand, an higher number of samples would lengthen the total measurement time: for this reason in a real measurement the step is chosen compromising between the improvement of the S/N ratio and the total acquisition time duration.

In chapter 4 the measurement wedge scan is indicated using this notation:

$$N_{start} \rightarrow N_{end}(\times \Delta x) \tag{3.2}$$

[3] This is the tolerance on the position value controlled in the LabVIEW software in the PC.

where N_{start} and N_{end} are the integer number of steps with respect to the ZPD position of the wedge translator starting position and ending position respectively [4] and Δx is the step width.

The measured temporal hypercubes are referred with respect to the wedge translations $\{x\}_{set}$ (unit of measurement μm): this results in spectral hypercubes in psuedo-frequency units (unit of measurement μm^{-1}). For this reason a frequency calibration of the HSM is necessary in order to convert the pseudo-frequency axis to real-frequency units. Such a calibration is retrieved measuring light with precisely known spectral lines [5]. In this way particular real frequencies are associated to related pseudo-frequencies values: then the calibration is calculated from the fitting of these points.

3.3 Calibration of the wedge translator

In section 3.1 we have given a description of the wedge translator control process and we have pointed out that the nominal precision imposed by the LabVIEW software is $0.1\mu m$.

In that description we have seen that, to check the position of the wedge translator, the software receives an input from the motor controller with the position value; this value is in turn affected by an error because of the translator encoder imprecision.

The errors made by the translator in the wedge excursion steps result in an uncorrect delay axis $\{\tau\}_{set}$ [6] the interferograms in the temporal hypercube are referred to: this is the cause of some artifacts in the spectrum that can be misleading for the analysis. To correct these errors a calibration of the system is necessary. This is obtained by measuring signal with narrowband frequency spectrum that will act as a physical reference in the retrieved spectra: for this reason we have chosen as reference the He:Ne laser (wavelength $633nm$). In the specific we have illuminated a spectralon [7] with the He:Ne laser beam and we have measured it in the reflection geometry. We have performed various scans in order to study the behaviour of the translator errors and to have a good statistics for the calibration. For the analysis of each measurement these steps have been followed:

1. A certain number of regions of interest (ROIs) in the hyperspectral

[4] Note that N_{start} and N_{end} can be negative since they are referred to the ZPD position

[5] Spectral peaks whose real frequency have been recorded with several instruments and tabulated in several literature works.

[6] As the delay axis $\{\tau\}_{set}$ is linear with respect to the wedge translations $\{x\}_{set}$ (as it is pointed out in section 1.5) and the frequency calibration, once it has been retrieved, is straightforward used for the spectra conversion, we refer to $\{x\}_{set}$ directly as the delay axis $\{\tau\}_{set}$ as we have previously done and we interchange this two notations.

[7] The spectralon is a fluoropolymer that has an high reflectrance over a wide region of the electromagnetic spectrum from ultraviolet to near-infrared.

image and their related mean spectra have been considered.

2. For each ROI mean spectrum the He:Ne peak (and its related pseudofrequency f) has been identified (because it is higher than the artifact peaks).

3. The spectra has been back transformed with the IFT operation considering a pseudofrequency range that included both the laser peak and the artifacts, obtaining the related interferogram y_τ.

4. The IFT of the spectra results in complex interfrograms in the form $y_\tau = |y_\tau| \cdot e^{i\phi(\tau)}$ with a phase ϕ. If the spectra have only the single laser peak, their complex interferograms are expected to have a phase $\phi(\tau) = 2\pi f\tau$. As we know that the He:Ne laser measurements has only one peak, we can theoretically impose a delays axis $\{\tau_c\}_{set}^{corrected}$ such that the oscillation phase is exactly in the form $\phi(\tau) = 2\pi f\tau_c$ (with the laser frequency f). Therefore, starting from the phase ϕ extrapolated from the interferograms y_τ of the error-affected measurement, the calculation
$$\tau_c = \frac{\phi}{2\pi f} \tag{3.3}$$
allows us to retrieve the correct positions $\{\tau_c\}_{set}^{corrected}$ of the translator.

5. Once we have retrieved the correct delay axis $\{\tau_c\}_{set}^{corrected}$, we can calculate the delays correction as:
$$\{\Delta\tau_c\}_{set}^{correction} = \{\tau_c\}_{set}^{corrected} - \{\tau\}_{set} \tag{3.4}$$
This is the calibration associated to a particular ROI.

6. The overall single measurement calibration is calculated as the mean of the calibrations $\{\Delta\tau_c\}_{set}^{correction}$ of the considered ROIs.

Figure 3.3 shows the delay corrections that have been calculated for some measurements on the He:Ne laser.

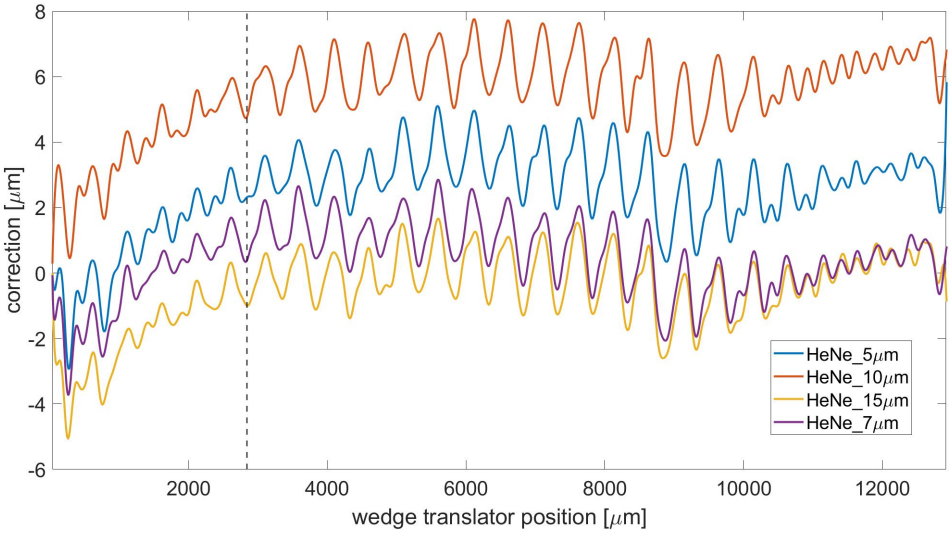

Figure 3.3: Delay corrections for each wedge translator position obtained from the measurements $HeNe\_5\mu m$, $HeNe\_10\mu m$, $HeNe\_15\mu m$, $HeNe\_7\mu m$ indicated in table 3.2. The vertical black dashed line indicates the zero path delay position which is $2846.3\mu m$. The x-axis has been considered in the excursion common to all the measurements (from position $41.3\mu m$ to position $12926.3\mu m$).

meas. name	step	initial pos.	final pos.	n° steps
$HeNe\_5\mu m$	$5\mu m$	$41.3\mu m$	$12926.3\mu m$	2577
$HeNe\_10\mu m$	$10\mu m$	$36.3\mu m$	$12926.3\mu m$	1289
$HeNe\_15\mu m$	$15\mu m$	$41.3\mu m$	$12926.3\mu m$	859
$HeNe\_7\mu m$	$7\mu m$	$39.2\mu m$	$12983.8\mu m$	1841

Table 3.2: Parameters of the measurements for the wedge translator position correction. All the other parameters that are not listed in this table have been kept constant for all the measurements (objective: $Leica^{®}$ 20×, integration time: $30ms$, gain:0, binning:3).

As it can be seen from Figure 3.3, except for a shift in the y-axis, the delays corrections of the different measurements (whose parameters are indicated in table 3.2) are almost equal for each translator position. This means that the error made by the translator is actually a systematic error and it can be properly corrected with a calibration. The vertical shift in the y-axis of the corrections retrieved in the different measurements is not a problem because a constant shift in the delay axis of the interferograms in a temporal hypercube determines a constant complex phase in the complex spectra (as stated in equation 2.17) that can be easily removed.

The final wedge translator calibration $\{\Delta\tau_{cal}\}_{set}^{calibration}$ has been obtained as the mean of the curves in Figure 3.3. This calibration is simply added to the measurement delay axis $\{\tau\}_{set}$ to retrieve the corrected

measurement delay axis $\{\tau_c\}_{set}^{corrected}$:

$$\{\tau_c\}_{set}^{corrected} = \{\tau\}_{set} + \{\Delta\tau_{cal}\}_{set}^{calibration} \tag{3.5}$$

Figure 3.4 shows the effect of the translator calibration (which has been retrieved on the basis of He:Ne laser) on a measurement of the Ti:sapphire laser (wavelength $785nm$). As it can clearly seen, if no calibration is applied the spectrum presents some artifacts that disturbs the proper visualization and physical analysis. If the calibration $\{\Delta\tau_{cal}\}_{set}^{calibration}$ is applied to the delay axis $\{\tau\}_{set}$ of the temporal hypercube according to equation 3.5, the FT provides a spectrum that does not present anymore the artifacts.

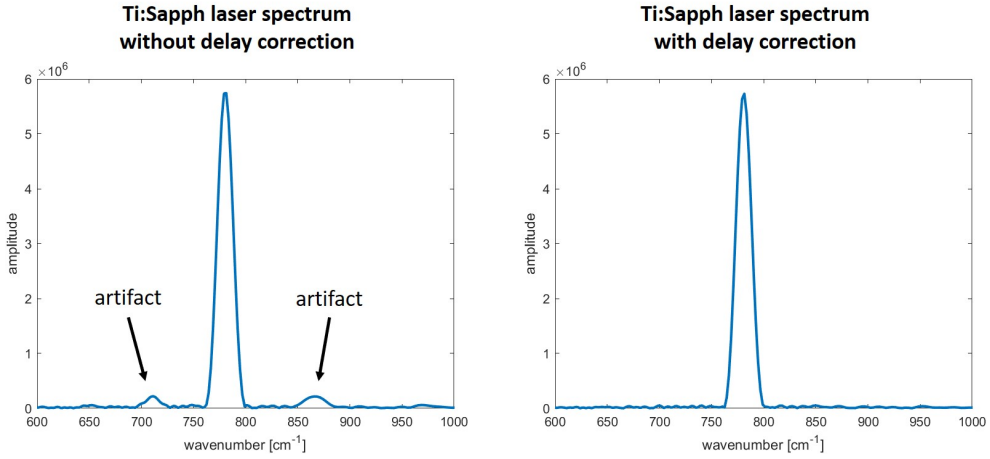

Figure 3.4: Effect of the application of the translator calibration on the spectrum of the Ti:sapphire laser measured by the HSM. The wedge excursion for this measurement has been $-200 \rightarrow +200(\times 10\mu m)$: this explain the very low spectral resolution.

This is an important result because it shows that the translator calibration works properly and it is able to clean up the spectra of the measurements from undesired false peaks.

Chapter 4

Application of the FT Hyperspectral Microscope

In chapter 3 the FT Hyperspectral Microscope based on TWINS has been presented and the measurement acquisition parameters has been discussed. In the present chapter some of the measurements obtained with the HSM and their related results are shown and analyzed in order to corroborate the reliability and the enormous potentials and applications of this system. Section 4.1 will show an electroluminescence measurement that clearly makes evident the fine sensibility of the HSM to small spectrum peak variations inside the FOV and then Section 4.2 will deeply focus on the very interesting and promising results of the HSM in the spontaneous Raman hyperspectral widefield imaging.

4.1 Commercial LEDs measurement

In this section we present some measurements on commercial Light Emitting Diodes (LEDs) acquired by the HSM system. These LEDs ($CreeXlamp^{®}$ XM-L and XP-E) have $1mm \times 1mm$ dimensions and are based on InGaN Multiple Quantum Wells (MQWs) technology. GaN is the most popular material in the semiconductor industry after silicon and it has a wide direct bandgap energy of $3.4eV$ at room temperature [28]; InN is a semiconductor with a direct bandgap energy of $0.7eV$ [29]. For this reason the emission wavelength of InGaN can be tuned over a wide range from visible red ($\sim 610nm$) to ultraviolet ($\sim 365nm$) by changing the alloy composition and and forming heterostructures such as quantum wells [30].

In these measurements the LEDs have been biased with different current values and their photoluminescence have been detected with the HSM. The measurements presented in this section and their related paramenters are lised in Table 4.1: the first three entries regard the XM-L green LED and the last two entries regard the XP-E amber LED. The the LED electrolu-

minescence has relatively broadband spectral features and therefore, as we have seen in section 1.2, the related interferogram oscillates only at short delays around the delay $\tau = 0$: for this reason we have acquired these measurements with small excursions (with respect to the maximum excursion allowed by the wedge translator) around the ZPD [1]. The excursion required by the XP-E amber is larger with respect to the XM-L green because it presents a typical spectrum with a tighter peak. Figure 4.1 (a) and Figure 4.1 (b) show the spectra of XM-L green and XP-E amber LEDs respectively: as it is indicated by the arrows, the peaks values can change. The nominal emission wavelength of the XM-L green LED is identified by Cree LED manufacturing company in the range $520 - 535nm$ and the nominal emission wavelength of the XP-E amber LED is identified around $585 - 590nm$: the results we have obtained with our measurements are an agreement with these values. As we have previously outlined, the emission peak shifts are determined by variation of alloy composition (concentration of GaN and InN) but there are other physical mechanisms that can determine them such as temperature increase or Quantum-Confined Stark Effect (QCSE)[2]. A red-shift of the emission spectrum peak can be determined by the temperature increase in InGaN (as it is shown in [33]) and a blue-shift, as the bias current increases, can be determined by the reduction of the Stark shift of QCSE because, upon the application of large forward bias, excess carriers are injected into the QW which screens part of the polarization field (as it is

[1] The LED electroluminescence is the result of injection of carriers in the semiconductor device and the following electrons-holes recombinations with spontaneous emissions of photons. In a semiclassical approach starting from the spontaneous emission rate $r_{sp} = A_{cv} \cdot f_c(\mathcal{E}_2) \cdot [1 - f_v(\mathcal{E}_1)]$ (considering the Einstein's coefficient A_{cv} and the Fermi-Dirac distribution of the valence band f_v and the conduction band f_c) for a given transition from a level $\mathcal{E}_2$ in the conduction band to a level $\mathcal{E}_1$ in the valence band, we can calculate the total spontaneous emission rate R_{sp} as a function of the photon frequency. Considering a joint density of states ρ_j, the total spontaneous emission rate can be written as $R_{sp} = r_{sp} \cdot \rho_j$. Starting from the expression of R_{sp}, the Full-Width-At-Half-Maximum (FWHM) $\Delta\lambda$ of the emission spectrum in terms of photon wavelength can be calculated as (see [31] for the demonstration):

$$\Delta\lambda \approx \frac{1.8\lambda^2 k_B T}{hc}$$

where λ is the emission spectrum peak, k_B is the Boltzmann constant, T is the temperature, h is the Planck constant and c is the speed of light in vacuum. Considering $\lambda \sim 500nm$ and $T \sim 300K$, we have $\Delta\lambda \sim 10nm$: this means that the electroluminescence signal has a typical bandwidth of $\Delta f \sim 10THz$ and therefore an interferogram oscillations extension of $\frac{1}{\Delta f} \sim 100fs$. As the delay variation introduced between two replicas of electric field at $600nm$ by a translation $\Delta x = 5\mu m$ of the $\alpha - BBO$ wedges (with apex angle $\alpha_{apex} = 7°$) is $0.29fs$, the electroluminescence interferogram extension is $\sim 350 \times \Delta x$: therefore a symmetric acquisition around the ZPD with ~ 350 steps determines a spectral resolution which is enougth to characterize a semiconductor electroluminescence spectrum.

[2] The QCSE is the decrease of the optical transition energy as a result of the band structure tilt. In QWs this determines a red-shift (referred to as Stark shift) with increase in the bias field [32].

shown in [34] for InGaN QWs) . For these reasons these commercial LEDs are very interesting sample to be investigated with hyperspectral imaging because both spatial and spectral information are important.

LED	**bias**	**int.time**
$XMLg$	$1\mu A$	$1000ms$
$XMLg$	$100\mu A$	$40ms$
$XMLg$	$40mA$	$3ms$
$XPEa$	$100\mu A$	$200ms$
$XPEa$	$40mA$	$15ms$

Table 4.1: Parameters used in the measurements of the commercial LEDs described in this section. $XMLg$ indicates the XM-L green LED and $XPEa$ indicates the XP-E amber green LED. **bias**: LED applied bias current. **int.time**: CCD integration time. For all these measurements we have used the $5\times$ objective, $-200 \rightarrow +200(\times 5\mu m)$ wedge scan for the XMLg LED and $-400 \rightarrow +400(\times 5\mu m)$ wedge scan for the XPEa LED, CCD gain equal to 1 and CCD binning equal to 1.

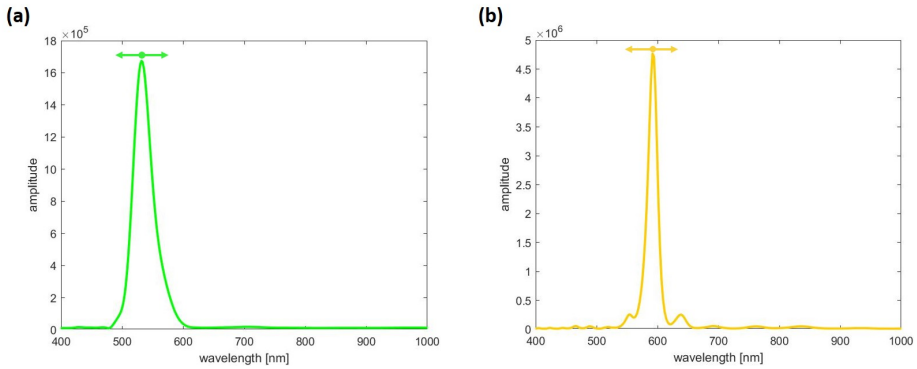

Figure 4.1: (a): typical luminescence spectrum of $CreeXlamp$® XM-L green LED measured with HSM. The arrows indicate that the position of the peak can change according to the bias current. (b): typical luminescence spectrum of $CreeXlamp$® XP-E amber LED measured with HSM. The arrows indicate that the position of the peak can change according to the bias current.

Figure 4.2 $(a) - (c)$ shows the map of the emission spectrum peak of the XM-L green LED for different values of bias current. In this figure the colorbar ranges have been chosen in order to enhance the small variation of the peak emission that the LED presents on its surface: these spatial changes of the spectrum peak are probably due to small variations of the InGaN alloy. For the three different values of current we can recognize some regions on the surface which present blue or red shift of the emission peak in few nanometers of wavelength range. Figure 4.2 $(d) - (f)$ shows the same maps for equal colorbar ranges (from $525nm$ to $540nm$): from these a general blue-shift of the peak is evident as the current increases. This

blue-shift of the emission wavelength can be attributed to the reduction of the Stark shift as the current increases.

The inhomogeneities of the emission peak can be seen also on the surface of the XP-E amber (Figure 4.3): even in this case the wavelength shift is in few nanometers range. In this case we have a general red-shift of the peak as the current increases: this can be physically explained as an effect of thermal heating due to the increase of injected electrons.

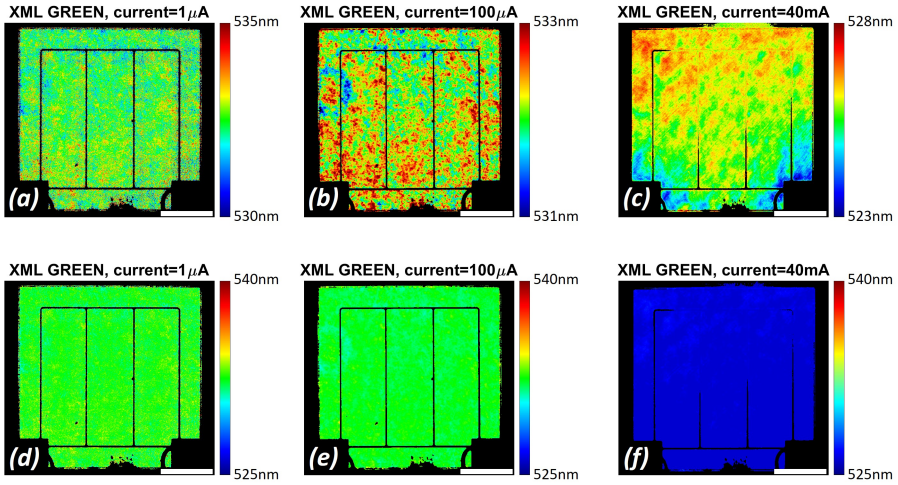

Figure 4.2: From (a) to (c): spectral peak maps of the XM-L green LED for different values of current ($1\mu A$, $100\mu A$ and $40mA$).
From (d) to (f): spectral peak maps of the XM-L green LED for different values of current ($1\mu A$, $100\mu A$ and $40mA$).
The colorbars indicate the peak wavelength value (in nm). The scale bar is $250\mu m$.

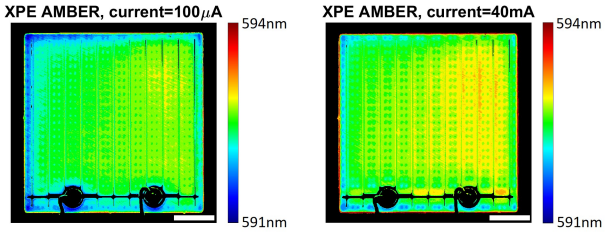

Figure 4.3: Spectral peak maps of the XP-E amber LED for different values of current ($100\mu A$ and $40mA$). The colorbars indicate the peak wavelength value (in nm). The scale bar is $250\mu m$.

These results are very important because they clearly show a fine sensitivity of the HSM to the peak shift over the measurement hyperspectral image: from the maps shown in Figures 4.2 and 4.3 we can appreciate spectrum peak variation even of $\sim 0.5nm$. Moreover these measurements clearly show that the spatial resolution is very high (spectral variation can be appreciated in $\sim 1\mu m$) infact it is the one of the 4-f system as we have seen in theory in section 1.5: the resolution is limited only by the objective nu-

merical aperture and there are not other worsening factors related to the acquisition system (the TWINS does not affect the spatial resolution). This is an optimum and very promising starting point for the FT widefield hyperspectral imaging for which the HSM has been designed for.

4.2 Widefield hyperspectral Raman measurements

Raman imaging is a very powerful technique to recognize the different species captured in the FOV because the Raman spectrum is like a "fingerprint" of the materials. Despite its huge potential for several application fields, Raman has some issues that make it a challenging technique and require many cares in the setup.

In this section a general introduction to Raman spectroscopy and its related issues are presented with a focus on Raman imaging. Then the application of the HSM on this field is presented and its related advantages with respect to other approaches is discussed. Finally some Raman measurements with HSM are illustrated highlighting the enormous potential of this setup for micro-sized samples recognition and characterization.

4.2.1 General introduction to Raman Imaging Spectroscopy and its related issues

In 1928 C.V. Raman and K.S. Krishnan reported the discovery of "a change of wave-length in light scattering" [35] that the scientific community would be referred to as Raman scattering. In 1930 C.V. Raman was awarded the Nobel prize for this fundamental discovery.

Spontaneous Raman scattering is an effect that can be detected if a medium is excited by light: the incoming photons with frequency ω_i can be elestically scattered (Rayleigh scattering) or inelastically scattered with a frequency that is lower (Raman Stokes scattering) or higher (Raman anti-Stokes scattering) with respect to the initial frequency [36]. In a macroscopic theory of inelastic light scattering we have that the Stokes photons have a frequency $\omega_S = \omega_i - \omega_0$ and the anti-Stokes photons have a frequency $\omega_{AS} = \omega_i + \omega_0$ where ω_0 is the frequency of atomic displacement associated with a phonon [3] of the material [38]. Figure 4.4 schematically illustrates the effect of light scattering on the photon frequency.

[3]The vibrations in a molecule can be described in terms of normal modes. A normal mode is a periodic collective motion where all particles involved move at the same frequency. A normal mode with oscillation frequency ω_0 in a quantum mechanics description (quantum harminic oscillator formalism) can be seen as a quantum state characterized by a certain number of quanta of vibration [37], phonons, each one with an energy $\hbar\omega_0$.

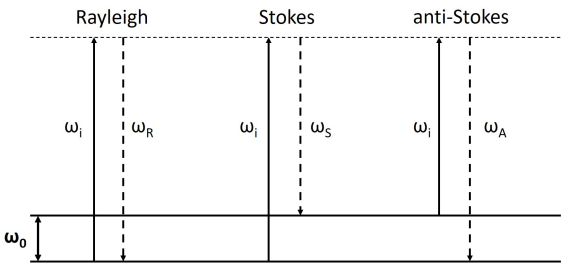

Figure 4.4: Schematic depiction of the elastic scattering (Rayleigh), Raman inelastic Stokes scattering (Stokes) and Raman inelastic anti-Stokes scattering (anti-Stokes). ω_0: phonon frequency. ω_i: incoming photon frequency. ω_R: Rayleigh scattered photon frequency which is equal to the incoming photon frequency. ω_S: Stokes scattered photon frequency. ω_{AS}: anti-Stokes scattered photon frequency.

Such a simple description of the Raman effect allows us to understand the selectivity of this phenomenon which is characterized by a frequency shift ω_0 which depends on the particular atomic positions, electron distribution and intermolecular forces of the material [39]. For this reason Raman spectroscopy has a lot of applications in different fields of scientific research such as biology [39, 40, 41], material science [42], pharmaceutical industry [43], medicine [44] and tumors diagnosis [45, 46, 47, 48]. Unfortunately Raman scattering is characterized by a very low cross section [4] which is typically 10^{-7} for Stokes signal and even weaker for the anti-Stokes signal [20, 49, 50]: this means that the excitation light fluence on the sample has to be very high (order of $10^{-2} - 10\frac{mJ}{\mu m^2}$) in order to have a significative Raman signal. To reach such fluences and to have a fixed and precisely known incoming photon frequency, the excitation source used to perform spontaneous Raman measurements is the laser light (pump source). The signal of interest in spontaneous Raman spectroscopy is the Stokes one (because the anti-Stokes has a lower cross-section) and for this reason the spontaneous Raman spectra are typically plotted as function of the wavenumber defined as the Stokes shift (with respect to the pump source) normalized on the speed of light quantity.

In 1975 Delhaye and Dhamelincourt introduced the first Raman microscope [51]. From that point several spontaneous Raman imaging techniques have been introduced but even nowadays this is a very challenging field in science because the high fluences required to reach an acceptable S/N result in **very long acquisition times** or **high laser power** focused on the sample paying attention not to overcome the damage threshold limit [5].

[4] The scattering cross section σ is defined by

$$N_s = N_i \cdot \sigma$$

which is the relation that links the number N_i of incoming photons to the number N_s of scattered photons [38].

[5] A typical sample damage threshold in terms of irradiance is $\sim 2 - 10\frac{mW}{\mu m^2}$ [52]

In section 1.4 we have pointed out the various imaging methodologies that have been developed and we have seen that they can be grouped in global (widefield) or raster (whiskbroom and pushbroom) acquisition techniques. As marked in [52], point-scan Raman mapping speed is about one to few spots per second (see for example [50] and [53]) and this results in very long image aquisition (hours) if this dwell time is multiplied by thousands of pixels. In [52] an high-speed hyperspectral spontaneous Raman imaging which relies on Spatial Light Modulation (SLM) is presented and the integration time per pixel results in $\sim 10ms$. Others have performed Raman widefield but the integration time per single pixel of the image is comparable to the Raman raster techniques [54, 55]. In all these works on spontaneous Raman imaging in general the acquisition of the Raman spectra is performed by means of grating dispersive spectrometers or bandpass filters at specific Raman peaks [6]. Fourier Transform spectroscopy has been applied to Raman since 1980s [56, 57] because of the higher throughput with respect to the grating spectrometers. There are some recent works which presented FT spontaneous Raman imaging [58, 59] but all of them rely on very cumbersome and complex setups.

In Raman spectroscopy there's the **problem of removal of the fluorescence background** [7]. In general the fluorescence phenomenon has an higher efficiency with respect to the Raman one. For this reason, in most of the cases, the excitation wavelength is chosen in the near-infrared region ($785nm$, $830nm$ and $1064nm$ are typical excitation wavelength chosen for Raman measurements) where most of the materials have no appreciable absorption [60, 61, 53]: this has the cost of reducing the Raman signal as its

[6] This is reasonable in the spectroscopic applications where it is sufficient to record only a minimal number of Raman images at specific wavenumber positions in order to reveal the spatial chemical heterogeneity of the sample [55].

[7] The **fluorescence** is the emission of light from the sample as a result of the de-excitation of the sample after illumination light absorption: therefore fluorescence is not a scattering phenomenon as Raman but it is the consequence of the re-emission of the energy previously deposited on the sample [20]. In a simple two-levels model the absorption phenomenon can be described in this way: an incoming illumination photon with energy $\Delta\mathcal{E}_a = \hbar\omega_a$ ($\hbar = \frac{h}{2\pi}$ where h is Plank constant and $\omega_a = 2\pi f_a$ where f_a is the frequency of the photon) disappears and the energy is transferred to an electron which is promoted from its starting electronic level (initial state, energy $\mathcal{E}_1$) to a final electronic level with higher energy (final state, energy $\mathcal{E}_2 = \mathcal{E}_1 + \Delta\mathcal{E}$). As a consequence of the energy conservation, the difference $\mathcal{E}_2 - \mathcal{E}_1$ must be equal to the energy $\Delta\mathcal{E}_a$ of the incoming photon ($\Delta\mathcal{E} = \Delta\mathcal{E}_a$). Then the electron can come back to the initial state and a photon $\Delta\mathcal{E}_\phi = \Delta\mathcal{E}$ is emitted. As real molecule possesses many vibrational and rotational levels (that, in effect, spread the electronic levels into multilevel bands), a part of the $\mathcal{E}_2$ energy is converted into phonon vibrations and the emitted photon has an energy lower with respect to the absorbed one ($\Delta\mathcal{E}_\phi < \Delta\mathcal{E}_a$): this explains the typical red-shift (Stokes shift) of the fluorescence with respect to the excitation light ($f_\phi < f_a$). The widening of the electronic levels to bands explains the broadband nature of fluorescence spectra. From this simple model we can understand that the fluorescence intensity dependence on the excitation frequency f_a is determined by the electronic levels structure of the material.

intensity scales with the fouth power of the excitation frequency [8].

As the Raman signals are very narrow peaks in comparison to the fluorescence bands, there are some analytical techniques that relies on this property to discriminate between the two. The demonstration of these techniques (e.g. shifted-spectra, first-derivative spectroscopy and fast Fourier transform filtering techniques) is beyond the scope of this section but it can be easily found in literature (e.g., [62, 63]). In Time-Resolved Spectroscopy there is the possibility of fluorescence removal through time-gating as the Raman interaction is practically instantaneous ($\ll 1ps$) and the fluorescence photons emission is, statistically, relatively slow ($\sim 100ps$) [64]. The methodology we have used with HSM to remove the fluorescence signal in our Raman spectra is discussed in subsection 4.2.2.

4.2.2 Raman FT acquisition with Hyperspectral Miscroscope: unilateral sampling of the interferogram

Together with the advantages described in section 1.2, another very important benefit of FT spectroscopy with respect to the dispersive spectroscopy based on prisms and gratings is the measurement of the interferogram itself instead of collecting directly a spectrum. As we have seen in the subsection 1.2.1, the interferogram of a broadband signal presents oscillations only in proximity of the delay $\tau = 0$ and then it settles to a constant value, instead the interferogram associated to a tightband signal oscillates even at very large delays (endlessly if it is spectrum is a monochromatic signal). Therefore, signals with a spectrum characterized by both broadband features and narrow features (see the example in Figure 4.5), the central part of the interferogram (around $\tau = 0$) gives information on the broadband characteristics of the spectrum (Figure 4.7), while the tails of the interferogram (at very large delays, $\mid \tau \mid \gg 0$) carries information only on the tightband features (Figure 4.6). In this way FT spectroscopy enables the uncoupling of the broadband part of the spectrum from the narrowband part by choosing the proper acquisition sampling of the interferogram in the proper delay interval. In Figures 4.5 and 4.7 only a small window in the delay axis has been shown in order to better visualize the interferograms: the oscillations extends much longher than the limits imposed by these plots because they are related to very thin lines in spectrum. The interferogram oscillations associated to

[8] The dependence on the fourth power of the frequency is a general and important property of light scattering (both Rayleigh and Raman) and it can be deduced from the Rayleigh scattering law:

$$P = \frac{e^2 \omega^4 r^2}{12\pi\epsilon_0 c^3}$$

where P is the power irradiated by an induced dipole, e is the electron charge, $\omega = 2\pi f$ is the pulsation (f is the oscillation frequency), r is the charges distance in the dipole, ϵ_0 is the dielectric constant and c is the speed of light in vacuum [14]. The demonstration applied to the Raman scattering can be found in [38].

the thin spactral lines are very small with respect to the central part of the interferogram because the total energy of the narrowband part, the integral of the thin lines in spectrum, is much smaller (four orders of magnitude in the example of Figures 4.5, 4.6 and 4.7) with respect to the energy of the broadband part, the integral of the broad shape of the spectrum.

As the Raman spectra are characterized by very narrow peaks, the concept depicted in Figures 4.5, 4.6 and 4.7 is the reason why **we have used for the Raman measurements acquisition an unilateral delay scan** with the wedge translator in order to **directly obtain fluorescence-free Raman spectra**. This unilateral acquisition is a key point of our Raman measurements approach that has not been used in previous FT Raman spectroscopy works [56, 57, 58, 59]. As it can be seen from the simulation of Figure 4.5, if we have a broadband part of the spectrum characterized by a consistent amplitude, the small tighband signal stays on top of the half-dynamics of the interferogram: applied to the Raman case this means that, if the fluorescence is a strong signal, it greatly raises up the half-dynamics and this sets a limit in the integration time and binning in order not to saturate the CCD.

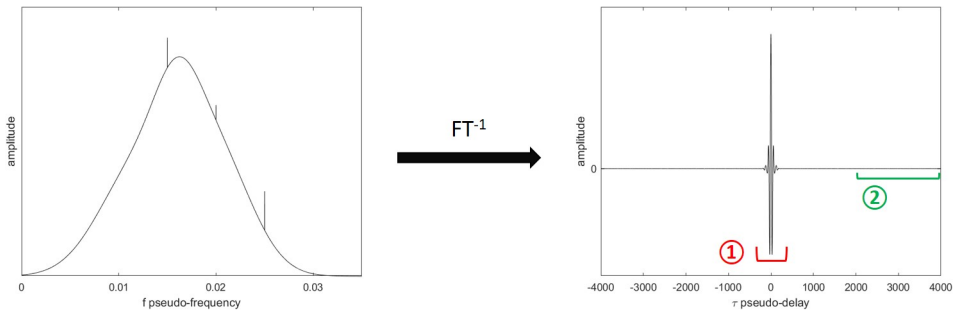

Figure 4.5: Left: an example of spectrum with a broadband component (the wide shape) and a tightband component (the thin lines). Right: the associated interferogram calculated as the IFT (FT^{-1}) of the spectrum on the left.

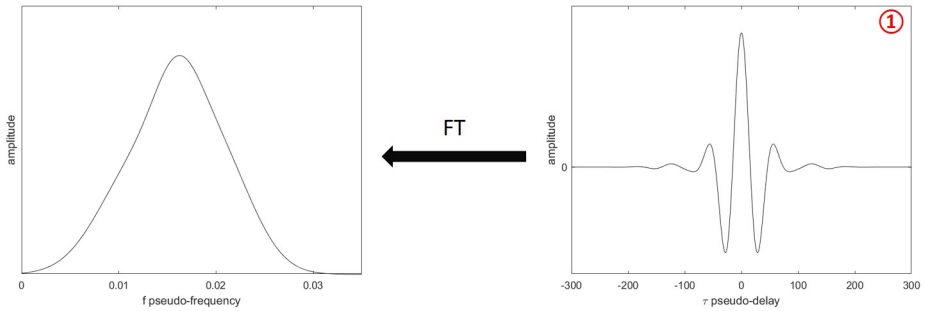

Figure 4.6: Right: the central part of the interferogram shown in Figure 4.5. Left: the associated spectrum.

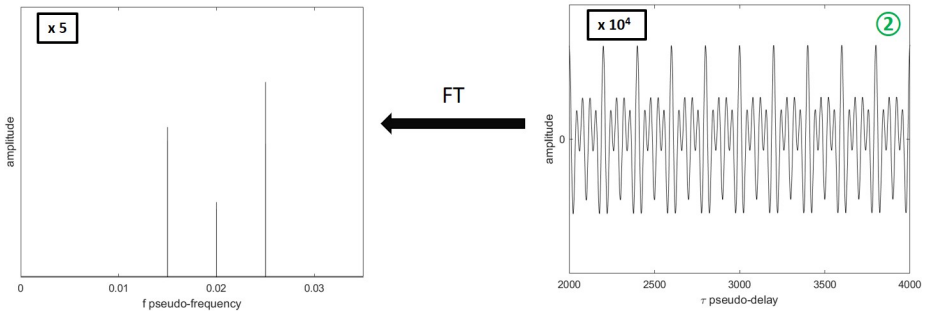

Figure 4.7: Right: the tail of the interferogram shown in Figure 4.5; the y-axis has been zoomed (zoom factor: 10^4) around the 0 amplitude in order to better visualize the oscillations; in the x-axis only a small part of the delays are shown as the interferogram is very long. Left: the associated spectrum (zoom factor: 5).

4.2.3 PMMA and PS beads Raman measurement

In this subsection we present and discuss the Raman measurement on Polymethyl methacrylate (PMMA) and Polystyrene (PS) beads with the HSM. The PMMA and PS are thermoplastics that constitute a standard sample for Raman spectroscopy as their Raman spectra have been broadly measured and they are well known in literature [65, 66, 67, 68, 69].

For Raman measurements with the HSM, the geometry of the top laser

illumination (described in section 3.1 and depicted in Figure 3.2) is used. The PMMA and PS beads sample has been prepared on an aluminum substrate [9]. We have performed two different measurements with two different pump sources: Ti:Sapphire laser (continous wave, wavelength $785nm$, power $155mW$) and frequency doubled Nd:YAG laser ($Spectra-Physics^{®}Millennia$, continous wave, wavelength $532nm$, power $2W$). In Table 4.2 all the measurements parameters are indicated. The wedge excursion have been $9.6mm$ that is almost the maximum allowed by the wedge translator for a unilateral acquisition (see chapter 3) and, after Happ-Genzel apodization, this results in a spectral resolution of $\sim 110cm^{-1}$ of the spectral hypercube. The spectral resolution can be improved by increasing the maximum delay scan: this can be reached by choosing longer wedges and a crystal with stronger birefringence than the α-BBO [10]. For both measurements we have used dichroic beam splitter (as it is shown in Figure 3.2): $Semrock^{®}$ LPD02-785RU for $785nm$ laser and $Semrock^{®}$ LPD02-532RU-25 for $532nm$ laser. In the detection branch we have located two filters in order to remove the laser signal: $Semrock^{®}$ RazorEdge Long Pass E-Grade 785 and $Thorlabs^{®}$ FELH0800 for $785nm$ laser; $Semrock^{®}$ RazorEdge LP03-532RU-25 and $Thorlabs^{®}$ FELH0550 for $532nm$ laser.

laser	**power**	**obj.**	**fiber**	**scan**	**time**	**g.**	**bin.**
$785nm$	$50mW$	$50\times$	$200\mu m$	$+30 \rightarrow +670(\times 15\mu m)$	$40s$	1	2
$532nm$	$450mW$	$20\times$	$400\mu m$	$+45 \rightarrow +1005(\times 10\mu m)$	$2s$	1	2

Table 4.2: PMMA and PS beads measurements paremeters with the two different pump sources. **laser**: laser pump wavelength. **power**: laser power on the sample. **obj.**: objective. **fiber**: fiber diameter. **scan**: wedge translator scan. **time**: CCD integration time. **g.**: CCD gain. **bin.**: CCD binning.

In the measurement with the $785nm$ excitation source the power on the sample was $50mW$ on a uniform circular spot of $\sim 200\mu m$ which was the image of the exit of the $200\mu m$ fiber (see section 3.1) [11]. The integration time per frame was set to $40s$ in order to reach a fluence per frame of $\sim 5{\cdot}10^{-2}\,\frac{mJ}{\mu m^2}$ that is small (about two orders of magnitude lower) in comparison to the

[9] Aluminum is typically used as sample substrate in Raman measurement because it has not Raman or fluorescence signal

[10] Using equation 1.22 considering $\alpha_{apex} = 7°$, YVO_4 crystal ($n_{\parallel} = 1.9987$ and $n_{\perp} = 2.2240$ at $600nm$ wavelength) and a wedge excursion $x = 30mm$, we can obtain a delay scan $\Delta\tau = 2745.7fs$ that corresponds to a spectral resolution of $12.140cm^{-1}$ that is acceptable if compared with other Raman imaging systems (for comparison see for example [50, 70, 71]).

[11] The magnification of the image of the fiber exit on the sample plane is not exactly 1 and infact the laser spot in the FOV is a bit smaller with respect to the diameter of the fiber.

ones typically used in Raman widefield [54, 55, 58, 59]. In the measurement with the $532nm$ laser the power on the sample was $450mW$ on a uniform circular spot of $\sim 400\mu m$ [12] and the integration time per frame was set to $2s$: this means a fluence of $\sim 6 \cdot 10^{-3} \frac{mJ}{\mu m^2}$. Figure 4.8 shows the False RGB map retrieved from the spectral hypercube of the $532nm$ exitation laser measurement in the spectral range from $2668cm^{-1}$ to $3172cm^{-1}$ and Figure 4.9 (a) and Figure 4.9 (b) show the related spectra of PS and PMMA. As it can be seen, the spectra are completely fluorescence-free because of the unilateral temporal hypercube acquisition described in subsection 4.2.2: this is the reason why we can rely on a $532nm$ excitation source that normally is avoided in FT Raman systems in order to have negligible fluorescence signal [60]. As the Raman signal intensity scales with the fourth power of the excitation frequency, switching from the $785nm$ to the $532nm$ extitation enhances the Raman emission by a factor ~ 4.7: this explains why with the $532nm$ pump we can rely on a smaller fluence on the sample for the single acquired frame and therefore on a much smaller integration time.

[12] See the previous note about the image of the fiber exit on the sample plane.

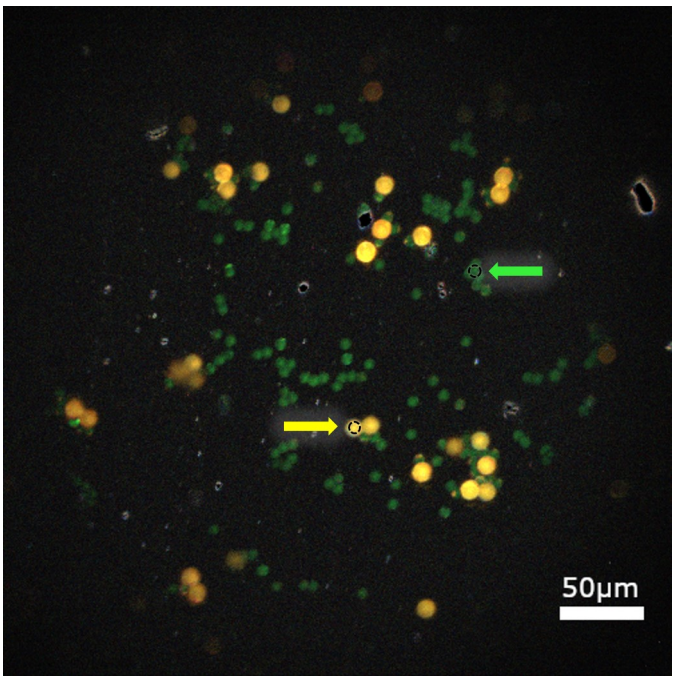

Figure 4.8: False RGB generated from the spectral hypercube considering the wavenumber interval $2668cm^{-1} - 3172cm^{-1}$. In this spectral interval the beads that results in green are the PMMA and the beads that results in yellow-orange are the PS. The yellow arrow indicates a ROI in a PS bead and the green arrow indicates a ROI in a PMMA bead. Laser pump wavelength: $532nm$. Power on the sample: $450mW$. Image dimensions: 502×501 pixels. Total temporal hypercube acquisition time: 36 minutes.

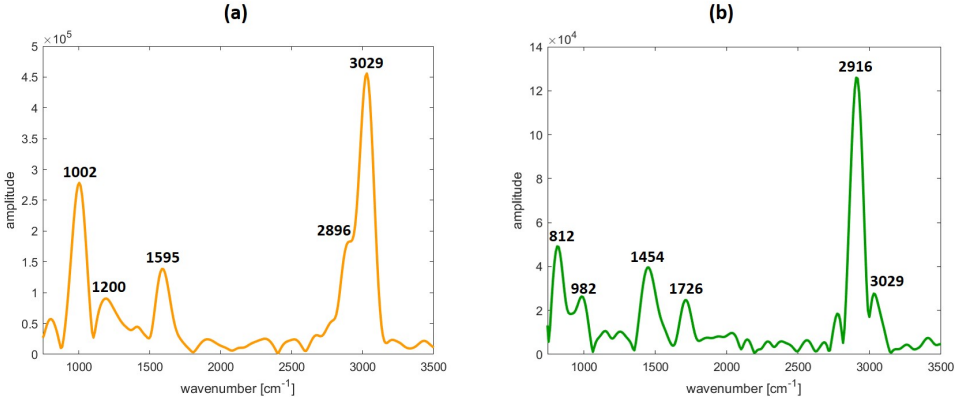

Figure 4.9: (a): Raman spectrum obtained as the mean of pixels in a ROI on a PS bead indicated by the yellow arrow in Figure 4.8. The spectral resolution is $\sim 110cm^{-1}$. (b): Raman spectrum obtained as the mean of pixels in a ROI on a PMMA bead indicated by the green arrow in Figure 4.8. The spectral resolution is $\sim 110cm^{-1}$.

The spectra obtained are in agreement with the ones reported in literature (see for example [65, 68]) and in the measurement with $532nm$ laser the strong peaks in the $3000cm^{-1}$ region related to the C-H bond stretching

vibration [72] are clearly present.

Figure 4.10 shows the comparison between the spectra of PS obtained with the $532nm$ excitation laser and the $785nm$ excitation laser: as it can be seen the S/N ratio is much better in the $532nm$ case and in the $785nm$ case the high wavenumber peaks are not present as they fall in a wavelength region near the $1100nm$ limit of the CCD sensitivity. Furthermore we have to point out the fact that the measurement with $532nm$ has required a total acquisition time of 36 minutes instead the measurement with $785nm$ has required a total acquisition time of 7 hours and 7 minutes! A total measurement time of 36 minutes for a 502×501 pixels image means a time per pixel of $\sim 9ms$ that is a competitive value with respect to the raster-scanning approaches that can be found in literature.

As the spectra resolution is $\sim 110cm^{-1}$ we are not able to distinguish all the peaks reported in [65] and [68]: as we have already pointed out, the spectral resolution can be greatly improved by increasing the maximum delay scan achievable by the wedge translator. Anyway the spectral hypercube obtained from the measurements with the $532nm$ allows us to clearly distingush the two species in the FOV based on their spectra with a very rapid acquisition in comparison to the performances of other Raman imaging systems. This is a very promising result considering that the HSM is a very compact and stable system that could have all the characteristics to be used in routinely laboratory and industrial research.

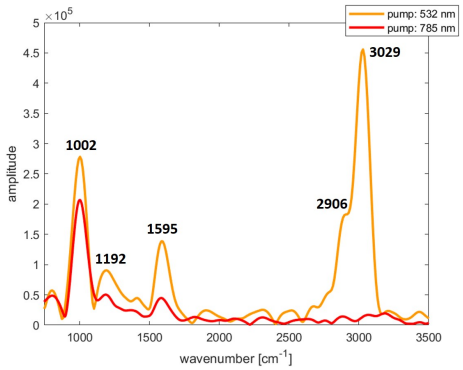

Figure 4.10: Comparison of the spectrum of a PS beads in the measurement with $532nm$ extitation laser (orange line) with respect to the measurement with $785nm$ extitation laser (red line).

4.2.4 Microplastics Raman measurement

In a collaboration project with Università Politecnica delle Marche and Università degli Studi di Padova we have planned measurements to test the HSM system in a possible application for the hyperspectral imaging identification of a series of microplastics (MPs). Nowadays MPs contamination constitutes a serious global environmental problem because MPs, particles smaller than 5mm in size, are easily ingested and have the potential to accumulate in

both biota and acquatic food web [73]. MPs are produced directly in pellets or abrasive agents industry but the large majority of environmental MPs are of secondary origin (e.g. degradation of plastic wastes or synthetic cloth washing).

In this subsection two examples of microplastics Raman measurements with the HSM are presented. These two measurements have been performed on a polyethylene (PE) and polystyrene (PS) powders mixture (PE grains $20 - 25\mu m$, PS grains $50 - 100\mu m$) and on a polyester (PEST) [13] and polyamide (PA) fibers mixture (PEST fibers $618 \pm 367\mu m$ length and $13 \pm 1\mu m$ diameter, PA fibers $566 \pm 500\mu m$ length and $11 \pm 1\mu m$ diameter) [14]. The samples have been prepared on an aluminum substrate and illuminated by the $532nm$ laser described in subsection 4.2.3 with the same illumination geometry in the HSM. The parameters have been identical for both these measurements and they are listed in Table 4.3.

laser	**power**	**obj.**	**fiber**	**scan**	**time**	**g.**	**bin.**
$532nm$	$450mW$	$20\times$	$400\mu m$	$+45 \rightarrow +1005(\times 10\mu m)$	$600ms$	1	2

Table 4.3: PE and PS mixture and PEST and PA mixture measurements paremeters. **laser**: laser pump wavelength. **power**: laser power on the sample. **obj.**: objective. **fiber**: fiber diameter. **scan**: wedge translator scan. **time**: CCD integration time. **g.**: CCD gain. **bin.**: CCD binning.

Figure 4.11 and Figure 4.13 show the reflectivity images obtained with the top illumination using a lamp (a) and the false RGB images retrieved from the Raman spectral hypercube (b) of the two measurements considering the range from $2590cm^{-1}$ to $3245cm^{-1}$ for the PE and PS mixture and the range from $2668cm^{-1}$ to $3412cm^{-1}$ for the PEST and PA mixture. Figure 4.12 and Figure 4.14 show the spectra of the two species for the respective measurement.

As in the measurement on the PMMA and PS beads described in subsection 4.2.3, on the basis of the spectra we are able to spatially distinguish the two species in the FOV. The spectrum of PS (Figure 4.12 (a)) is consistent with the one retrieved from the PS bead in the previous section. The spectrum of PE (Figure 4.12 (b)) is in agreement with the one described in [75]. We can see the band at $2832cm^{-1}$ that is consistent with the symmetric ($2848cm^{-1}$) and antisymmetric ($2883cm^{-1}$) carbon-hydrogen bond stretching in the CH_2 group: we are not able to distinguish these two peaks

[13] The generic description of "polyester" usually refers to fibers of the polymer poly(ethylene terephthalate) (PET) [74].

[14] All these samples have been arrived from the Ecotoxicology and Environmental Chemistry of Università Politecnica delle Marche.

because of the poor spectral resolution. The peak at $1432cm^{-1}$ can be related to the CH_2 bending (between $1416cm^{-1}$ and $1440cm^{-1}$ in [75]) and the peak at $1284cm^{-1}$ is explained with the CH_2 twisting ($1296cm^{-1}$ in [75]).

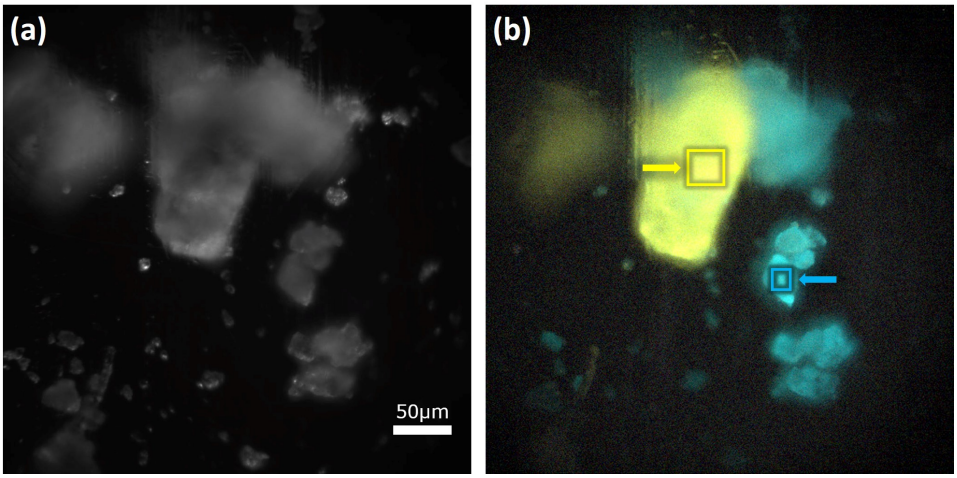

Figure 4.11: (a): reflectivity image of the PE and PS measurement (1004×1002 pixels) illuminating the sample by a lamp. (b): false RGB image (502×501 pixels) generated from the spectral Raman hypercube considering the wavenumber interval $2590cm^{-1} - 3245cm^{-1}$. In this spectral interval of the false RGB, the PE grains result in light blue and the PS grains result in yellow. The yellow arrow indicates a ROI in a PS grain and the light-blue arrow indicates a ROI in a PE grain. Laser pump: $532nm$. Power on the sample: $450mW$. Total temporal hypercube acquisition time: 14 minutes.

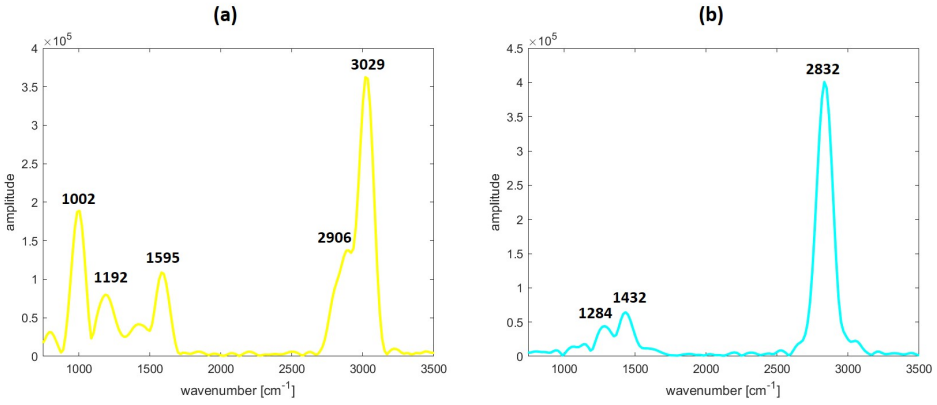

Figure 4.12: (a): Raman spectrum obtained as the mean of pixels in a ROI on a PS grain indicated by the yellow arrow in Figure 4.11. (b): Raman spectrum obtained as the mean of pixels in a ROI on a PE grain indicated by the light-blue arrow in Figure 4.11. The spectral resolution is $\sim 110cm^{-1}$.

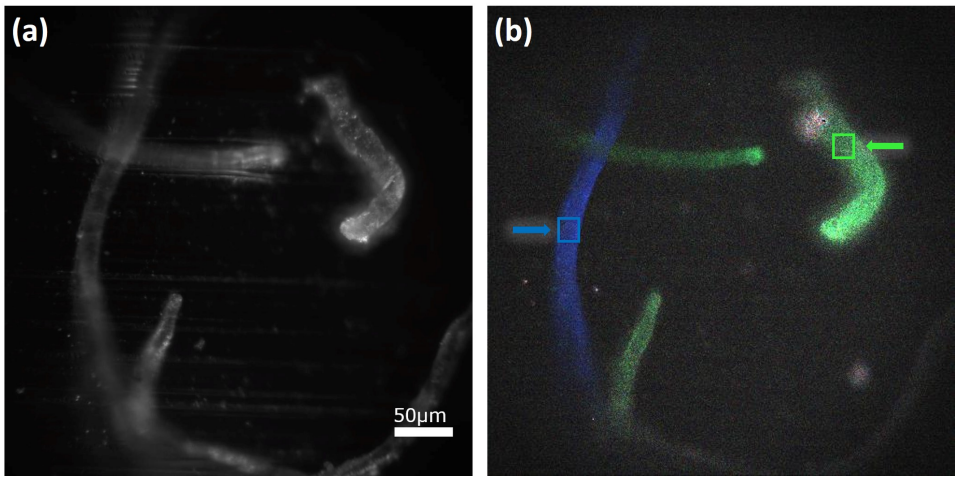

Figure 4.13: (a): reflectivity image of the PEST and PA measurement (1004 × 1002 pixels) illuminating the sample by a lamp. (b): false RGB image (502 × 501 pixels) generated from the spectral hypercube considering the wavenumber interval $2668cm^{-1} - 3412cm^{-1}$. In this spectral interval of the false RGB, the PEST fibers result in green and the PA fibers result in blue. The blue arrow indicates a ROI in a PA fiber and the green arrow indicates a ROI in a PEST fiber. Laser pump: $532nm$. Power on the sample: $450mW$. Total temporal hypercube acquisition time: 14 minutes.

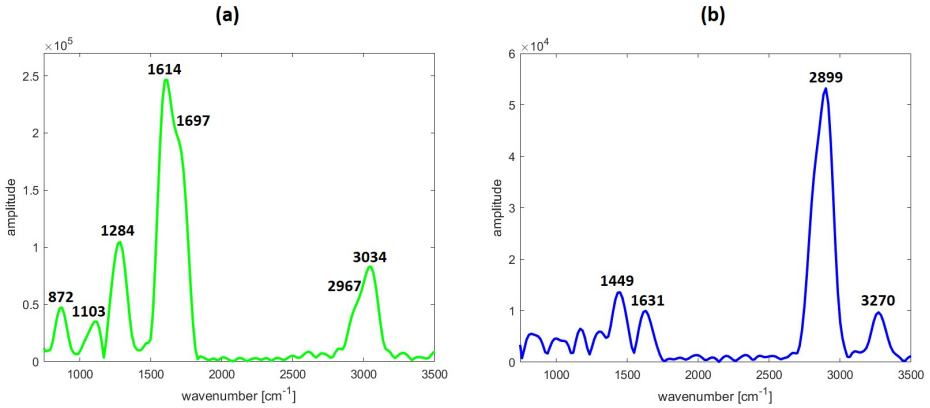

Figure 4.14: (a): Raman spectrum obtained as the mean of pixels in a ROI on a PEST fiber indicated by the green arrow in Figure 4.13. (b): Raman spectrum obtained as the mean of pixels in a ROI on a PA fiber indicated by the blue arrow in Figure 4.13. The spectral resolution is $\sim 110cm^{-1}$.

The PEST spectrum (Figure 4.14 (a)) is in agreement with the Raman spectra reported in [75, 76, 74, 77]. In [76] a Raman band is identified at $1615cm^{-1}$ ($1610cm^{-1}$ in [77]) and it is related to the $C-C$ bond in the benzene ring and in [74] the band near $1700cm^{-1}$ ($1725cm^{-1}$ in [77]) is related to the ester $C=O$ stretching: we can see these two peaks in our measurement with the HSM in the band at $1614cm^{-1}$ and as a shoulder at $\sim 1697cm^{-1}$. In [77] a clearly visible band at $1289cm^{-1}$ is reported and this is the one

we have at $1284cm^{-1}$. In the same article other peaks around $\sim 1100cm^{-1}$ and $\sim 850cm^{-1}$ are identified and these are in agreement with the ones we can see at $1103cm^{-1}$ and $872cm^{-1}$. The peaks at $\sim 2900cm^{-1}$ (that we see as a shoulder in Figure 4.14 (a)) can be explained as the frequencies of the CH_2 symmetric ($2908cm^{-1}$) and antisymmetric ($2970cm^{-1}$) stretching that are shifted of $\sim 50cm^{-1}$ with respect to the ones polyethylene because of the presence of the oxygen adjacent to the $C-H$ bond in PEST chemical structure [75]. The strong peak at $\sim 3000cm^{-1}$ is also present in the spectra shown in literature.

The spectrum that results from the PA fiber (Figure 4.14 (b)) can be explained on the basis of what is discussed in [78]. The high $2899cm^{-1}$ peak can be related to CH_2 antisymmetric ($2922cm^{-1}$) and symmetric ($2850cm^{-1}$ and $2907cm^{-1}$) stretching. The peak at $3270cm^{-1}$ is the nitrogen-hydrogen stretching in the amide group. The peak at $1631cm^{-1}$ can be related to the amide I Raman peak that is a typical one in both synthetic and natural polymers containing the secondary amide group $-CONHR$ [75]. The $1449cm^{-1}$ can be correlated to the evident CH_2 reported at $1440cm^{-1}$ in [78] and then all the other peaks are probably consistent with the CH_2 twisting and $C-C$ stretching listed in the same article.

4.2.5 Graphene monolayer Raman measurement

In this subsection a Raman measurement on a graphene sample is presented. First we provide a brief and general introduction on its structure and properties together with a brief explanation on the Raman process in such a material and the related peaks that have been studied in literature. A complete and deep study of the Raman spectrum of graphene is beyond the purpose of this subsection that has only the role to show a potential application of the HSM.

Graphene is a flat monolayer of carbon atoms organized in a 2D honeycomb lattice and it is the basic constituent of the 3D graphite, 1D nanotubes and 0D fullerenes [79]. Graphene has been firstly isolated and characterized by Andre Geim and Konstantin Novoselov in 2004 [80] and they were awarded the nobel prize in 2010 for this work. Nowadays there is an intense interest in graphene because of its exciting potential applications for example in electronics, photonics, sensors and energy generation and storage [81, 82]. Graphene is characterized by very high carrier mobility and for this reason it should enable transistors operating at very high frequencies ($\sim 100GHz$) [83]; electrons in graphene behave as massless two-dimensional particles which results in a wavelength independent absorption [81]; graphene is the strongest material ever measured [84]...

The Raman spectrum of graphene has been measured and characterized for the first time in 2006 [85]. As outlined in [86], Raman spectrum contains information about both atomic structure and electronic properties. For this

reason the Raman spectrum is a fundamental phenomenon that allows to distinuish pristine graphene from defected graphene and to study edges and doping which are at the origin of variation of the electronic properties. From the point of view of its electronic properties, graphene is a 2D zero-gap semiconductor [87]. The microscopically description of Raman scattering of light in a semiconductor involves three systems [38]:

- incident and scattered photons
- electrons in the semiconductor
- the phonon involved in the scattering

This description is more complex with respect to the one used to demonstrate the Raman activity in molecules which is related only to the normal modes of oscillation of the atoms nuclei [15]. One-phonon modes in defect-free samples can be Raman active only if their symmetry is correct and their wave vector is zero. As pointed out in [38], in a microscopic picture the Raman scattering in a semiconductor proceeds in three steps:

1. The incident photon excites the semiconductor into an intermediate state $|a\rangle$ by creating an electron-hole pair (or exciton)
2. The exciton is scattered into another state by emitting a phonon. We denote this intermediate state as $|b\rangle$
3. The exciton in $|b\rangle$ recombines radiatively with emission of scattered photon

In such a scattering process the wavevector must be conserved: this means that the wavevector in the final state $|b\rangle$ must be equal to the wavevector in $|a\rangle$. There can be two-phonon Raman scattering events that ivolve the emission of two phonons such that the wavevector conservation is satisfied: in the particular case in which the two phonons are identical (same wavevector) the related Raman peak is called *overtone*.

As it can be seen from this microscopic description, electrons play an important role in the Raman scattering of phonons although they remain

[15] Raman activity in molecules is present for a particular normal mode if the Raman tensor $[\alpha]$ belongs to the same symmetry species as that normal mode [75]. Given a polarizability tensor $[p]$ and a particular normal mode with coordinate U_m, the single element ij of the Raman tensor is defined as:

$$\alpha_{ij} = \frac{\partial p_{ij}}{\partial U_m}$$

where p_{ij} is the ij element of $[p]$. The polarizability tensor is such that

$$\vec{\mu} = [p]\,\vec{E}$$

where $\vec{E}$ is the electric field and $\vec{\mu}$ is the induced dipole moment.

unchanged after the process.

As shown in [86], graphene presents two main Raman peaks called the G peak and the 2D peak. The G peak ($\sim 1580 cm^{-1}$) is due to the degenerate in-plane optical mode, thus it is related to a one-phonon process. The 2D peak ($\sim 2700 cm^{-1}$) is due to a two-phonon scattering event called intervalley event: it is named 2D because it is the overtone of the D peak which is due to the breathing modes of the six-atoms rings of graphene. The D peak ($\sim 1350 cm^{-1}$) would be determined by a one-phonon scattering process but, as a result of wavevector conservation, it can happen only by means of the electron scattering on a defect: for this reason it is absent in pristine graphene. Another peak that is present in pristine graphene is the so called 2D' peak which is the overtone of the D' peak: the D' peak is related to an intravalley process and, as well as the intervalley process related to the D peak, it can happen only by means of a defect. 2D' peak ($\sim 3250 cm^{-1}$) is present in pristine graphene because, as well as the 2D peak process, it is due to a two-phonon scattering where the wavenumber is conserved. There's another scattering event that gives rise to another peak called D+D" that is a combination of the phonon related to the D peak and a phonon related to the D" peak. The D" peak has been seen in defected graphene measured with visible light and it is related to a phonon at $\sim 1100 cm^{-1}$ [88]. The D+D" peak ($\sim 2450 cm^{-1}$) is present in the spectrum of pristine graphene because, as the 2D peak, it is related to a two-phonons (phonon D + phonon D") intervalley scattering event. In defected graphene there's the D+D' peak ($\sim 2975 cm^{-1}$) which is due to a two-phonons (D phonon + D' phonon) scattering event with one intravelley phonon and one intervalley phonon: this process is not possible in pristine graphene because the overall wavevector conservation can be guarateed only by means of an electron scattering on a defect. Figure 4.15 shows the Raman processes related to the peaks we have considered in our discussion.

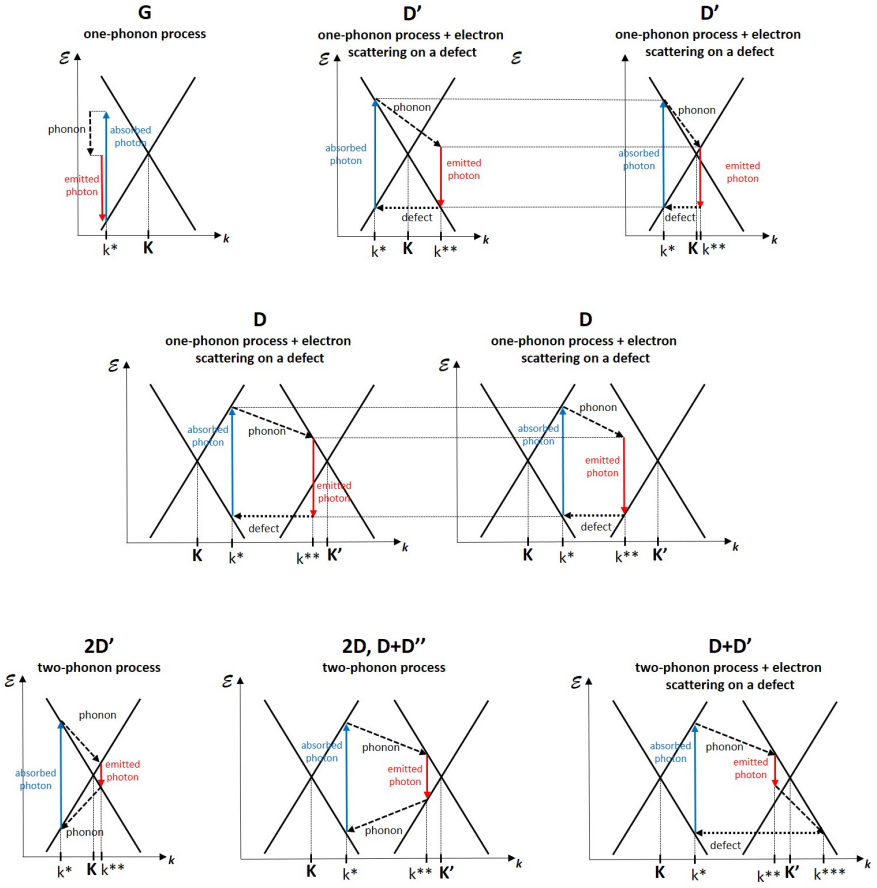

Figure 4.15: The most relevant scattering process related to the graphene Raman peaks. Each graph (energy $\mathcal{E}$ vs wavenumber k) presents the schematic of graphene electronic dispersion (Dirac cones).

With HSM we have measured an hexagonal-shaped monolayer graphene sample (heaxagon side $\sim 200\mu m$) grown on a SiO_2 substrate. The measurement paramenters are listed in Table 4.4.

Figure 4.16 shows a false RGB image obtained from the spectral hypercube considering an interval around the graphene 2D peak measured at $2645cm^{-1}$ (see the graphene measured spectrum in Figure 4.17). Thanks to this peak we are able to clearly distinguish the graphene from the SiO_2 substrate. As it can be seen from Figure 4.17, in this measurement we can see the G peak at $1567cm^{-1}$. The spectrum doesn't clearly show the D+D" peak expected at $\sim 2500cm^{-1}$ and the 2D' peak expected at $\sim 3250cm^{-1}$ because the S/N is too low: there's a very small peak near the 2D peak ($2645cm^{-1}$) at $\sim 2428cm^{-1}$ and another one at $\sim 3198cm^{-1}$ but we can't assure that they are real signal peaks. The G peak presents a small shoulder on its right: this is probably the D' peak that emerges in cases of defects but the spectral hypercube of this measurement is too much noisy to outline

a spatial map of the defects on the basis of this property and a much better spectral resolution would be needed to clearly distinguish the G peak from the D' peak. The absence of a clear D peak at $\sim 1350cm^{-1}$ suggests that the graphene sample is not too much defected.

laser	**power**	**obj.**	**fiber**	**scan**	**time**	**g.**	**bin.**
$532nm$	$789mW$	$20\times$	$400\mu m$	$+45 \rightarrow +1005(\times 10\mu m)$	$6s$	1	2

Table 4.4: Hexagonal monolayer graphene measurement paremeters. **laser**: laser pump wavelength. **power**: laser power on the sample. **obj.**: objective. **fiber**: fiber diameter. **scan**: wedge translator scan. **time**: CCD integration time. **g.**: CCD gain. **bin.**: CCD binning.

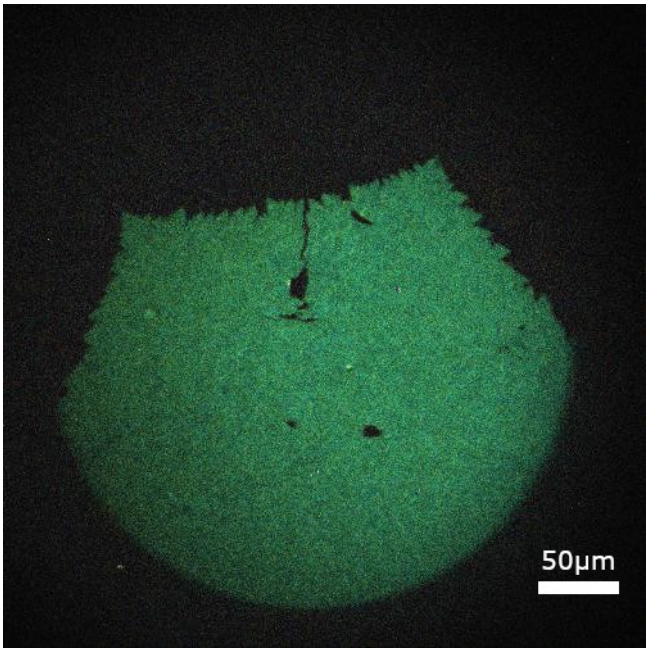

Figure 4.16: False RGB image (502×501 pixels) generated from the spectral hypercube considering the wavenumber interval $2537cm^{-1} - 2797cm^{-1}$. In this spectral interval of the false RGB, the graphene results in green and the SiO_2 background results in black as it has no signal in the considered spectral range. Laser pump: $532nm$. Power on the sample: $789mW$. Total temporal hypercube acquisition time: 1 hour 40 minutes

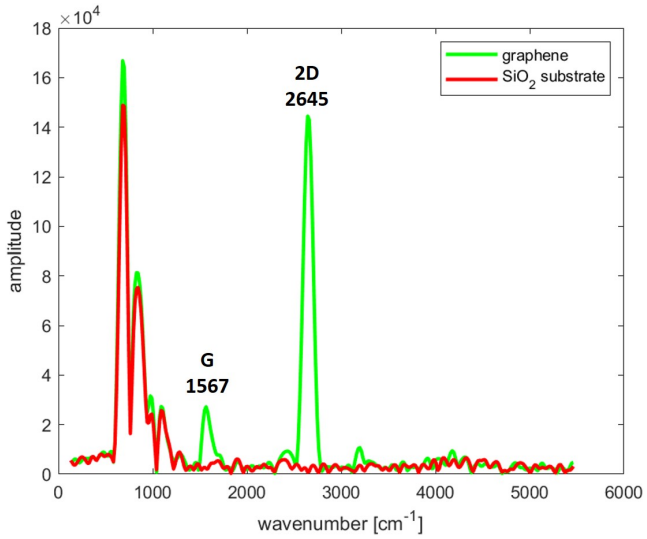

Figure 4.17: Spectra obtained as mean of a ROI on the graphene and a ROI on the SiO_2 background. The 2D and the G peak of graphene are clearly distingushable.

In [85] the change and the shift of the 2D peak as the numbers of graphene layers increases is discussed. The measurement we have taken with the HSM has a S/N that is not enough to obtain a reliable map of the 2D peak for the peak spectral position in each single pixel but, with an higher S/N, it would allow to study the presence of multiple graphene layers on the sample area. A possible way to increase the S/N would be using a band-pass filtering that removes all the light under $\sim 1000cm^{-1}$: in this way the half-dynamics of the interferograms determined by the fluorescence of the SiO_2 would be reduced and this would allow an higher binning or integration time. In this way we will loose the small wavenumber interval of the spectrum but, from Figure 4.17, it is clear that that region of the spectrum is anyway spoilt by the peaks of the SiO_2 substrate. In addition the relevant graphene peaks are between $1100cm^{-1}$ and $3500cm^{-1}$.

This preliminary result obtained with the HSM is very promising because it shows the capacity of the system to perform widefiled Raman imaging on a monolayer material in a reasonable measurement acquisition time and, after some setup improvements (such as the spectral resolution and the bandpass filtering), the possibility to study the electronic properties of graphene samples on their surface with a spatial resolution that is the one of an optical microscope.

Conclusions and future planning

This thesis work has validated the widefield high-throughput HSM as a reliable system to perform fluorescence-free Raman imaging measurements in small acquisition times ($\sim 9ms$ per image pixel) and with an high spatial resolution ($\sim 1\mu m$) and spectrum peak sensitivity ($\sim 0.5nm$). However the spectral resolution allowed by the present TWINS interferometer based on α-BBO crystal is $\sim 110cm^{-1}$ which is not enough for Raman adjacent peaks distinction. As it has been pointed out in this thesis, the spectral resolution can be improved with an higher wedge excursion in the measurement acquisition and with an higher birefringence of the crystals. For this reason the next step in the optimization of the HSM for Raman imaging application is to improve the spectral resolution up to $25cm^{-1}$ at least: we have extimated that such a resolution can be reached using YVO_4 crystal and an almost three-times longer wedge excursion with respect to the one allowed by the actual interferometer. The enhancement of the resolution will make the HSM a very impressive instrument in the Raman imaging community and a very powerful setup for several applications. Furthermore the acquisition approach outlined in subsection 4.2.2 can allow separation of the Raman signal from the fluorescence one. This property can be exploited for the acquisition of a pair of measurements for the same sample: one fluorescence acquisition and one Raman acquisition. Further work has to be done in this sense but, in principle, this system is ready for the measurement of a fluorescence hypercube and a Raman hypercube of the same sample FOV.

Bibliography

[1] Candeo, A., et al. "A hyperspectral microscope based on an ultrastable common-path interferometer." *APL Photonics* 4.12 (2019): 120802.

[2] W. Smith, D. Zhou, F. Harrison, H. Revercomb, A. Larar, A. Huang, and B. Huang, "Hyperspectral remote sensing of atmospheric profiles from satellites and aircraft." *Proc. SPIE 4151*, 94 – 102 (2001).

[3] C. Stellman, F. Olchowski, and J. Michalowicz, "WAR HORSE (wide-area reconnaissance: hyperspectral overhead real-time surveillance experiment)." *Proc. SPIE 4379*, 339–346 (2001).

[4] Lu, Guolan, and Baowei Fei. "Medical hyperspectral imaging: a review." *Journal of biomedical optics 19.1* (2014): 010901.

[5] Dale, Laura M., et al. "Hyperspectral imaging applications in agriculture and agro-food product quality and safety control: A review." *Applied Spectroscopy Reviews* 48.2 (2013): 142-159.

[6] Hege, E. Keith, et al. "Hyperspectral imaging for astronomy and space surveillance." *Imaging Spectrometry IX.* Vol. 5159. International Society for Optics and Photonics, 2004.

[7] Liang, Haida. "Advances in multispectral and hyperspectral imaging for archaeology and art conservation." *Applied Physics A 106.2* (2012): 309-323.

[8] Fischer, Christian, and Ioanna Kakoulli. "Multispectral and hyperspectral imaging technologies in conservation: current research and potential applications." *Studies in Conservation 51.sup1* (2006): 3-16.

[9] Wiener, N. "Generalized harmonic analysis." *Acta mathematica 55* (1930): 117-258.

[10] Born, Max, and Emil Wolf. "Principles of optics: electromagnetic theory of propagation, interference and diffraction of light." *Elsevier, pp. 9-24* (2013): 9-24.

[11] Gilardi, G. "Analisi tre." *Milano: McGraw-Hill, pp. 235* (2014): 235.

[12] Michelson, Albert A., and Edward W. Morley. "On the Relative Motion of the Earth and of the Luminiferous Ether." *Sidereal Messenger, vol. 6, pp. 306-310 6* (1887): 306-310.

[13] Weiner, Andrew M. "Ultrafast optics." *John Wiley & Sons, Inc., pp.89-91* (2009): 89-91

[14] Pedrotti, Frank L., Leno M. Pedrotti, and Leno S. Pedrotti. "Introduction to optics." *Cambridge University Press* (2017).

[15] Bell, R.J. "Introductory Fourier Transform Spectroscopy", *Academic Press, pp.19-25*, New York (1972): 19-25

[16] Herres, Werner, and Joern Gronholz. "Understanding FT-IR data processing. Part 1: Data Acquisition and Fourier Transformation." (1984).

[17] Perri, A., et al. "Hyperspectral imaging with a TWINS birefringent interferometer." *Optics express* 27.11 (2019): 15956-15967.

[18] Brida, Daniele, Cristian Manzoni, and Giulio Cerullo. "Phase-locked pulses for two-dimensional spectroscopy by a birefringent delay line." *Optics letters* 37.15 (2012): 3027-3029.

[19] Herres, Werner, and Joern Gronholz. "Understanding FT-IR data processing. Part 2: Details of the Spectrum Calculation." (1985).

[20] Mertz, Jerome. "Introduction to optical microscopy." *Cambridge University Press*, 2019.

[21] Harris, Fredric J. "On the use of windows for harmonic analysis with the discrete Fourier transform." *Proceedings of the IEEE* 66.1 (1978): 51-83.

[22] Nuttall, Albert. "Some windows with very good sidelobe behavior." *IEEE Transactions on Acoustics, Speech, and Signal Processing* 29.1 (1981): 84-91.

[23] Cooley, James W., and John W. Tukey. "An algorithm for the machine calculation of complex Fourier series." *Mathematics of computation 19.90* (1965): 297-301.

[24] Greengard, Leslie, and June-Yub Lee. "Accelerating the nonuniform fast Fourier transform." *SIAM review 46.3* (2004): 443-454.

[25] Mertz, Lawrence. "Auxiliary computation for Fourier spectrometry." *Infrared Physics 7.1* (1967): 17-23.

[26] Knoll, Glenn F. "Radiation detection and measurement." *John Wiley & Sons, pp.497-501* (2010): 497-501.

[27] Zhou, Zhimin, Bedabrata Pain, and Eric R. Fossum. "Frame-transfer CMOS active pixel sensor with pixel binning." *IEEE Transactions on electron devices 44.10* (1997): 1764-1768.

[28] Rais-Zadeh, Mina, et al. "Gallium nitride as an electromechanical material." *Journal of Microelectromechanical Systems 23.6* (2014): 1252-1271.

[29] Krishna, Shibin, et al. "Ultrafast photoresponse and enhanced photoresponsivity of Indium Nitride based broad band photodetector." *Solar Energy Materials and Solar Cells 172* (2017): 376-383.

[30] Shan, W., et al. "Optical properties of $In_xGa_{1-x}N$ alloys grown by metalorganic chemical vapor deposition." *Journal of Applied Physics 84.8* (1998): 4452-4458.

[31] Nisoli, Mauro. "Semiconductor photonics. Principles and Applications." *Società Editrice Esculapio*, *pp.100-103*, 2016: 100-103

[32] Turchinovich, Dmitry. "Study of ultrafast polarization and carrier dynamics in semiconductor nanostructures: a THz spectroscopy approach." *The University of Freiburg*, *pp.62* (2004): 62

[33] Oliver, Rachel A., et al. "InGaN quantum dots grown by metalorganic vapor phase epitaxy employing a post-growth nitrogen anneal." *Applied Physics Letters 83.4* (2003): 755-757.

[34] Takeuchi, Tetsuya, et al. "Quantum-confined Stark effect due to piezoelectric fields in GaInN strained quantum wells." *Japanese Journal of Applied Physics 36.4A* (1997): L382.

[35] Raman, Chandrasekhara V. "A change of wave-length in light scattering." *Nature 121.3051* (1928): 619-619.

[36] Amer, Maher, ed. "Raman spectroscopy for soft matter applications." *John Wiley & Sons*, *pp.15-19*, 2009.

[37] Simon, Steven H. "The Oxford solid state basics." *OUP Oxford*, 2013.

[38] Peter, Y. U., and Manuel Cardona. "Fundamentals of semiconductors: physics and materials properties." *Springer Science & Business Media*, *pp.375-426*, 2010: 375-426

[39] Carey, Paul R. "Raman spectroscopy, the sleeping giant in structural biology, awakes." *Journal of Biological Chemistry 274.38* (1999): 26625-26628.

[40] Rangan, Shreyas, et al. "Applications of Raman spectroscopy in the development of cell therapies: State of the art and future perspectives." *Analyst 145.6* (2020): 2070-2105.

[41] Matthäus, Christian, et al. "Infrared and Raman microscopy in cell biology." *Methods in cell biology 89* (2008): 275-308.

[42] Vašková, Hana. "A powerful tool for material identification: Raman spectroscopy." *Int. J. Math. Model. Methods Appl. Sci 5* (2011): 1205-1212.

[43] Paudel, Amrit, Dhara Raijada, and Jukka Rantanen. "Raman spectroscopy in pharmaceutical product design." *Advanced drug delivery reviews 89* (2015): 3-20.

[44] Ling, Jian, et al. "Direct Raman imaging techniques for study of the subcellular distribution of a drug." *Applied optics 41.28* (2002): 6006-6017.

[45] Haka, Abigail S., et al. "Diagnosing breast cancer by using Raman spectroscopy." *Proceedings of the National Academy of Sciences 102.35* (2005): 12371-12376.

[46] Huang, Zhiwei, et al. "Near-infrared Raman spectroscopy for optical diagnosis of lung cancer." *International journal of cancer 107.6* (2003): 1047-1052.

[47] Chen, Pu, et al. "Bio-Raman spectroscopy: a potential clinical analytical method assisting in disease diagnosis." *Analytical Methods 3.6* (2011): 1257-1269.

[48] Vanna, Renzo, et al. "Raman Spectroscopy Reveals That Biochemical Composition of Breast Microcalcifications Correlates with Histopathologic Features." *Cancer research 80.8* (2020): 1762-1772.

[49] Zhang, Yin, Hao Hong, and Weibo Cai. "Imaging with Raman spectroscopy." *Current pharmaceutical biotechnology 11.6* (2010): 654-661.

[50] Keren, S., et al. "Noninvasive molecular imaging of small living subjects using Raman spectroscopy." *Proceedings of the National Academy of Sciences 105.15* (2008): 5844-5849.

[51] Delhaye, Michel, and Paul Dhamelincourt. "Raman microprobe and microscope with laser excitation." *Journal of Raman Spectroscopy 3.1* (1975): 33-43.

[52] Qi, Ji, Jingting Li, and Wei-Chuan Shih. "High-speed hyperspectral Raman imaging for label-free compositional microanalysis." *Biomedical optics express 4.11* (2013): 2376-2382.

[53] Gierlinger, Notburga, Tobias Keplinger, and Michael Harrington. "Imaging of plant cell walls by confocal Raman microscopy." *Nature protocols 7.9* (2012): 1694-1708.

[54] Li, Haibo, et al. "A practical wide-field Raman imaging method with high spectral and spatial resolution." *Review of Scientific Instruments 89.8* (2018): 083103.

[55] Schlücker, Sebastian, et al. "Raman microspectroscopy: a comparison of point, line, and wide-field imaging methodologies." *Analytical Chemistry 75.16* (2003): 4312-4318.

[56] Chase, D. Bruce. "Fourier transform Raman spectroscopy." *Journal of the American Chemical Society 108.24* (1986): 7485-7488.

[57] Chase, Bruce. "Fourier transform Raman spectroscopy." *Analytical Chemistry 59.14* (1987): 881A-890A.

[58] Wadduwage, Dushan N., et al. "Near-common-path interferometer for imaging Fourier-transform spectroscopy in wide-field microscopy." *Optica 4.5* (2017): 546-556.

[59] Müller, Walter, et al. "Light sheet Raman micro-spectroscopy." *Optica 3.4* (2016): 452-457.

[60] Qin, Jianwei, et al. "Advances in Raman spectroscopy and imaging techniques for quality and safety inspection of horticultural products." *Postharvest Biology and Technology 149* (2019): 101-117.

[61] Smith, Gregory D., and Robin JH Clark. "Raman microscopy in archaeological science." *Journal of archaeological science 31.8* (2004): 1137-1160.

[62] Mosier-Boss, P. A., S. H. Lieberman, and R. Newbery. "Fluorescence rejection in Raman spectroscopy by shifted-spectra, edge detection, and FFT filtering techniques." *Applied Spectroscopy 49.5* (1995): 630-638.

[63] Cadusch, P. J., et al. "Improved methods for fluorescence background subtraction from Raman spectra." *Journal of Raman Spectroscopy 44.11* (2013): 1587-1595.

[64] Everall, Neil, et al. "Picosecond time-resolved Raman spectroscopy of solids: capabilities and limitations for fluorescence rejection and the influence of diffuse reflectance." *Applied spectroscopy 55.12* (2001): 1701-1708.

[65] Palm, Ann. "Raman Spectrum of Polystyrene." *The Journal of Physical Chemistry 55.8* (1951): 1320-1324.

[66] Serafim, Andrada, et al. "Osteoblast-like cell behavior on porous scaffolds based on poly (styrene) fibers." *BioMed research international 2014* (2014).

[67] Thomas, K. J., et al. "Raman spectra of polymethyl methacrylate optical fibres excited by a 532 nm diode pumped solid state laser." *Journal of optics a: pure and applied optics 10.5* (2008): 055303.

[68] Haris, M. R. H. M., S. Kathiresan, and S. Mohan. "FT-IR and FT-Raman spectra and normal coordinate analysis of poly methyl methacrylate." *Der Pharma Chemica 2.4* (2010): 316-323.

[69] Qi, Ji, and Wei-Chuan Shih. "Parallel Raman microspectroscopy using programmable multipoint illumination." *Optics letters 37.8* (2012): 1289-1291.

[70] Davis, Brandon M., et al. "Multivariate hyperspectral Raman imaging using compressive detection." *Analytical chemistry 83.13* (2011): 5086-5092.

[71] Timlin, Jerilyn A., et al. "Spatial distribution of phosphate species in mature and newly generated mammalian bone by hyperspectral Raman imaging." *Journal of Biomedical Optics 4.1* (1999): 28-34.

[72] Yvon, Horiba Jobin. "Raman spectroscopy for analysis and monitoring." nd). Retrieved from *http://www. horiba. com/fileadmin/uploads/Scientific/Documents/Raman/bands. pdf* (2017).

[73] Magni, Stefano, et al. "The fate of microplastics in an Italian Wastewater Treatment Plant." *Science of the Total Environment 652* (2019): 602-610.

[74] Keen, Imelda P., Graeme W. White, and Peter M. Fredericks. "Characterization of fibers by Raman microprobe spectroscopy." *Journal of Forensic Science 43.1* (1998): 82-89.

[75] Bower, David I., and W. F. Maddams. "The vibrational spectroscopy of polymers." *Cambridge University Press*, 1992.

[76] Lang, Patricia L., et al. "The identification of fibers by infrared and Raman microspectroscopy." *Microchemical journal 34.3* (1986): 319-331.

[77] Bulkin, Bernard J., Menachem Lewin, and Frank J. DeBlase. "Conformational change, chain orientation, and crystallinity in poly (ethylene terephthalate) yarns: Raman spectroscopic study." *Macromolecules 18.12* (1985): 2587-2594.

[78] Menchaca, C., et al. "Mechanisms for the modification of nylon 6, 12 by gamma irradiation." *International Journal of Materials and Product Technology 19.6* (2003): 521-529.

[79] Geim, Andre K., and Konstantin S. Novoselov. "The rise of graphene." *Nanoscience and technology: a collection of reviews from nature journals.* 2010. 11-19.

[80] Novoselov, Kostya S., et al. "Electric field effect in atomically thin carbon films." *science 306.5696* (2004): 666-669.

[81] Novoselov, Konstantin S., et al. "A roadmap for graphene." *nature 490.7419* (2012): 192-200.

[82] Zhu, Yanwu, et al. "Graphene and graphene oxide: synthesis, properties, and applications." *Advanced materials 22.35* (2010): 3906-3924.

[83] Lin, Y-M., et al. "100-GHz transistors from wafer-scale epitaxial graphene." *Science 327.5966* (2010): 662-662.

[84] Lee, Changgu, et al. "Measurement of the elastic properties and intrinsic strength of monolayer graphene." *science 321.5887* (2008): 385-388.

[85] Ferrari, Andrea C., et al. "Raman spectrum of graphene and graphene layers." *Physical review letters 97.18* (2006): 187401.

[86] Ferrari, Andrea C., and Denis M. Basko. "Raman spectroscopy as a versatile tool for studying the properties of graphene." *Nature nanotechnology 8.4* (2013): 235-246.

[87] Novoselov, K. S., et al. "Electronic properties of graphene." *physica status solidi (b) 244.11* (2007): 4106-4111.

[88] Tan, PingHeng, et al. "Probing the phonon dispersion relations of graphite from the double-resonance process of Stokes and anti-Stokes Raman scatterings in multiwalled carbon nanotubes." *Physical Review B 66.24* (2002): 245410.

Acknowledgements

Ringrazio **Cristian** per avermi guidato in questa esperienza di tesi che si è rivelata una magnifica avventura nel mondo dell'imaging iperspettrale e per avermi insegnato a lavorare in un contesto in cui i risultati si ottengono solo con la costanza, la dedizione e la passione. Ringrazio tutti i professori che mi hanno seguito o sostenuto in questo percorso: **Gianluca Valentini**, **Andrea Bassi**, **Giulio Cerullo**, **Daniela Comelli**, **Cosimo D'Andrea** e **Antonio Pifferi**. Ringrazio tutte le persone del personale del Dipartimento di Fisica e del CNR che mi hanno aiutato in questi mesi o che mi hanno accompagnato in una parte del lavoro sperimentale in laboratorio: **Renzo Vanna**, **Alessia Candeo**, **Andrea Farina**, **Alberto Ghezzi**, **Marta Ghirardello**, **Lorenzo Colombo**, **Simone Atzeni**, **Chiara Trovatello**, **Armando Genco**, **Michele Devetta**, **Antonio Di Natale**, **Carlo Brambilla**, **Giuseppe Romano**. Ringrazio tutte le persone che hanno dedicato il loro lavoro a progetti legati alla mia esperienza di tesi: il professore **Nicola Trivellin** dell'Università di Padova, la ricercatrice **Alessandra Biancolillo** dell'Università degli Studi dell'Aquila, **Giuseppe Vitucci** di Optec S.p.a., **Fabrizio Preda** della spin-off NIREOS, il professor **Marco Malagodi** dell'Università di Pavia, i professori **Andrea Frontini** e **Francesco Regoli** dell'Università Politecnica delle Marche, la professoressa **Lucia Gemma Delogu** dell'Università di Padova.

Ringrazio **papà** e **mamma** per avermi permesso di iscrivermi e seguire questo corso di studi al Politecnico di Milano e per avermi sempre incoraggiato nel mio percorso universitario in cui non sono mancate le fatiche e difficoltà. Ringrazio mia sorella **Maddalena** (Maddaaa!!!) per le lunghe chiaccherate fisico-matematiche (e di programmazione) e su svariati argomenti (tra cui musica, film e attori) e per la simpatia. Ringrazio mio fratello **Bernardo** per il confronto su argomenti di fisica e di informatica di un certo livello (tanto lui li macina anche meglio di me che ho 7 anni in più) e per il "movimento" che ha sempre portato in famiglia. Ringrazio mio fratello **Martino** per tutte le cose che mi racconta e mi fa imparare ogni volta che ci vediamo e per le discussioni su Star Wars, Minecraft e tante altre belle cose. Ringrazio tutta la mia famiglia allargata: le **nonne Ignaziella e Carmela** e **tutti gli zii e cugini** con cui sono cresciuto e con cui ho vissuto innumerevoli esperienze. Ringrazio tutti quelli che mi guardano da lassù: i nonni **Benedetto** e **Salvatore**, lo **zio Alberto** e lo **zio Giuseppe**.
Della mia famiglia allargata ci tengo in particolare a ringraziare mio cugino **Andrea** che è sempre stato un punto di riferimento nella mia vita e un amico fondamentale (forse la persona con cui più mi trovo in sintonia e d'accordo): fu lui che 7 anni fa (quando ancora non avevo molto chiaro cosa avrei fatto) mi fece scoprire e mi

consigliò di intreprendere il corso di studi di Ingegneria Fisica al Politecnico di Milano. Allo stesso modo ci tengo a ringraziare mio cugino e padrino di cresima **Luca** per le grandi passioni che mi ha trasmesso (Tolkien in particolare) che, partendo dalla nostra infanzia, non si sono mai esaurite e continuano a tenerci in contatto nonostante gli impegni e la distanza.
Ringrazio **Marco "Peo"** per l'amicizia che ci ha tenuti legati durante il Liceo e che continua nelle poche ma gioiose volte che ci vediamo ancora. Ringrazio tutta la mia classe delle superiori e tutti i miei amici di Vicenza.
Ringrazio i miei amici della Lega dello Zabaione che hanno sempre reso uniche le estati in Sicilia e che mi hanno sempre riempito di felicità: **Donato**, **Malcolm**, **Pippo**, **Giovanni il Miglio** per tutti i momenti fantastici passati insieme fin da quando eravamo piccoli (e abitavamo a pochi metri di distanza) e **Salvo**, il mio vecchio amico, per le lunghe chiaccherate su The Lord of the Rings e la Terra di Mezzo.

Ed ora passiamo a chi negli anni universitari mi ha dovuto sopportare.

Tanto tempo fa in un appa lontano, lontano ...
(Main Title Soundtrack)

UNA NUOVA IGNORANZA

É un periodo di passaggio. I precedenti componenti di Picard hanno lasciato il loro vecchio (e malridotto) appa; solo ***Tommi Piazza*** *è rimasto fedele alla casa e ha radunato nuovi inquilini provenienti da luoghi diversi e improbabili.*
Durante i primi mesi, grazie al superlativo lavoro di ***Peppo****, i nuovi compagni sono riusciti ad avere un appa più pulito e meglio organizzato.*

Ciascun membro ha grandi potenzialità: ***Sbrisolino*** *è sempre bellissimo,* ***Michelle*** *è un genio della musica e un cuoco eccezionale,* ***Pedo*** *porta sempre tanta allegria e* ***Gio Elisei*** *è un cantante e chitarrista di grande talento. I battibecchi non mancano. Le solite dispute Nord-Sud (in genere accese da chi è, o pensa di venire, da sopra il Po) scatenano un po' di scompiglio. Tuttavia c'è sempre un argomento condiviso da tutti e ricorrente nei discorsi durante le cene: il PIZZETTO DI 16, una barbetta che sporge dal mento della giovane e inesperta matricola.*

*Per volontà dell'appa nella sera della cena di Natale, la giovane matricola gareggia (con il pizzetto colorato di blu e con le treccine) nelle Olimpioladi (o Piolimpiadi o Piolimpioladi: non ho mai capito come si chiamino veramente), la prestigiosa (davvero?) gara di corsa delle matricole del piazzale Piola. Grazie alla buona sorte (in gergo "botta di c***") riesce a vincere: in questo modo Picard si riprende il primato che gli spetta.*
Ma il meglio deve ancora arrivare. Con il mercato di gennaio arriva un'altra sorpresa nell'appa: ***Kalach*** *...*

Ringrazio tutti le persone che mi hanno sopportato nel mio primo anno da matricola e tutte quelle che lo hanno fatto negli anni successivi: **Ross (17)**, **Titti**, **Spugna**, **Gaolo Poldoni**, **Samsung**, **Mitch**, **Bubba**, **Ciotto (18)**, **Schiellmann**, **Attila**, **Giorgio Poje**, **Zorro**, **Ciro**, **Pippo**, **Matri**, **Totò**, **Pietro Pe-**

terburg e **Valentina**, **Nico**, **Ago**, Bold (che metto sottolineato perchè lui è già "bold"), **Marco**.
Ringrazio tutti i "numeri" che mi hanno succeduto **17**, **18**, **19 (Ciano)** e **20** (se ce ne fossero altri ringrazio anche loro) e, ci tengo a sottolinearlo, sicuramente sono maggiori del sottoscritto.
Ringrazio **Gio Elisei** per l'amicizia che è nata negli anni di Picard, per le "cerche" e "missioni" che abbiamo vissuto insieme, per l'amore per il maiale e la "ciccia" e, ovviamente, lo ringrazio per il progetto Perugia... ah sì, ovviamente lo ringrazio anche per tutte le cene a base di specialità umbre. Ringrazio **Peppo** per avermi insegnato che le lezioni sono sopravvalutate e per avermi fatto sentire "giovane e inesperto" (ora mi sento un po' meno giovane ma comunque sempre inesperto). Ringrazio **Pedo** per il mio soprannome (mi risulta l'abbia inventato lui), per avermi colorato il pizzetto di blu, per avermi scritto 16 sulla schiena (e disegnato altre cose nel petto e nelle braccia) e per le lunghe chiaccherate in appa che abbiamo fatto nel mio primo anno. Ringrazio **Kalach** semplicemente perchè è **Kalach** e mi ha voluto tanto bene. Ringrazio **Tommi Piazza** per avermi insegnato (o meglio, provato ad insegnare) ad aprire le bottiglie di birra con le posate e per avermi fatto caricare per le Piolimpiadi. Ringrazio **Sbrie** per avermi insegnato che devo pulire meglio le padelle e per aver tirato insieme a me un sospiro di sollievo dopo che la Juve ha perso la finale di Champions con il Real. Ringrazio **Michelle** per i tanti consigli che mi ha dato strada facendo sul mio percorso di studi che è stato anche il suo prima di me. Ringrazio **Ssette (17)** per le chiamate a tavola: "Sssseeeeediciiiiii, è prontooooo!!!!" Ringrazio **Titti** per aver portato in appa i pugnali di Legolas e la magnifica lavagnetta (e per **Titti** intendo **Titti**, non tutti). Ringrazio **Spugna** per tutte le cose divertenti, interessanti e "pazze" che mi ha insegnato. Ringrazio **Samsung** per tutte le lunghe chiaccherate sulla Marvel. Ringrazio **Gaolo Poldoni** per avermi consigliato Thomas Bergersen e per avere condiviso con me la passione per il Metallo. Ringrazio **Mitch** per non avermi mai pestato nonostante le molte minacce. Ringrazio **Bubba** per aver tollerato (forse) la mia avversione alla Juve. Ringrazio **Ciotto** per la grinta e l'ottima prestazione alle Olimpioladi del dicembre 2017 e per il periodo in cui abbiamo sognato insieme "a Maggica" sul tetto d'Europa. Ringrazio **Shellman** (il nome può subire variazioni nello spelling) per tutte le favolose pietanze che ha preparato in questi anni. Ringrazio **Pippo** per avermi iniziato al bazzinianismo. Ringrazio **Giorgio**, **Attila**, **Nico** e **Ciccio** per il continuo confronto sulle nostre esperienze universitarie negli anni della magistrale e per la stima reciproca. Ringrazio **Zorro** perchè è l'unica persona che ho conosciuto in questi anni di Ringhiera che mi risulta abbia letto il Silmarillion. Ringrazio **Ciro** per averci sempre ricordato di fare le pulizie. Ringrazio **Matri** per avermi ricordato la mia lontana giovinezza quando giocavo con le miniature di The Lord of The Rings della Games Workshop. Ringrazio **Totò**, il campione in carica delle Olimpioladi prima del mio anno, per avermi aiutato a "spiegare i calendari" nella mia prima cena di Natale. Ringrazio **Peterburg** per avermi invogliato a conoscere Python e per i saluti "Ciao bellezz!". Ringrazio **Ago** per tutte le volte che si incazza quando il Milan subisce un'ingiustizia. Ringrazio Bold per la torta al testo e per essere un

tifoso juventino molto sportivo (anche se, a volte, gode un po' troppo quando il Milan va male). Ringrazio **Marco**, uno dei superstiti del Liceo Quadri di Vicenza (come il sottoscritto), per la musica che ascolta e mi ha consigliato (non è facile al giorno d'oggi trovare persone che ascoltano musica decente: ovvero classica, metal e rock) e tutti i consigli di carattere informatico che mi ha dato.
Ringrazio i miei compagni di corso con cui ho affrontato le fatiche del Poli (e mille briscole epiche): **Amede'**, **Ricca'**, **Agosti'**, **Luha**, **Pena**, **Filippo (Flpflp)** e **Gauge**.
Ringrazio **Alessandro**, **Marco** e **Salvo** per la bellissima esperienza di laboratorio progettuale nella tesina triennale.
Ringrazio tutte le persone che in qualche modo mi hanno arricchito e accompagnato nella mia crescita e nella mia vita fino a questo momento.
Infine, per ultimo in questa lista di ringraziamenti ma non certo l'ultimo nella mia vita, ci tengo a ringraziare **Giovanni**, detto **il Tambu**: lui per me è un Fratello fin da quando siamo stati battezzati insieme e la cui amicizia è quella che maggiormente mi regala momenti, nell'inesorabile fatica della vita, in cui intravedo una verità più profonda oltre le mura del mondo.

- 16